DEVELOPMENT OF ACOUSTIC MICROFLUIDIC PLATFORMS FOR SEPARATION AND ANALYSIS OF PARTICLES AND CELLS

A Dissertation

by

HAN WANG

Submitted to the Office of Graduate and Professional Studies of
Texas A&M University
in partial fulfillment of the requirements for the degree of

DOCTOR OF PHILOSOPHY

Chair of Committee,	Arum Han
Committee Members,	Arul Jayaraman
	Byung-Jun Yoon
	Jun Kameoka
	Yong-Joe Kim
Head of Department,	Miroslav M. Begovic

August 2015

Major Subject: Electrical Engineering

ABSTRACT

Acoustofluidics has been an emerging technology that combines fluidic control of microfluidics technology and particle handling of acoustics technology. This integrative approach provides non-contact and efficient particle and cell manipulation inside microfluidic channels. In this work, two acoustofluidic platforms have been developed, one for environmental monitoring application and one for medical application.

The first platform was developed that enabled trapping and quantification of crude oil droplets for environmental monitoring application. Crude oil spills have serious ecological and economic impacts. Detecting low concentrations of oil after dispersion into small oil droplets is challenging and has immense importance in marine environment monitoring, such as in the case of large-scale oil spill as well as chronic oil discharge. Current fluorescence-based oil detectors have trade-offs between detection sensitivity and portability. In this research an acoustic radiation force based microfluidic device was developed to trap and concentrate oil droplets in water, which facilitated highly sensitive fluorescence detection of concentrated oil droplets as well as sampling for further off-chip analysis. The developed system successfully trapped low concentration crude oil droplets utilizing a circular acoustic resonance cavity, detected the accumulated oil droplets with a compact fluorescence detector, and separated the concentrated oil droplets to a downstream collection outlet for further off-chip analysis.

The second platform was developed to analyze the biophysical properties of cells such as their density and compressibility for differentiating cancer cells of different stages. It has been reported that biophysical properties of cells are related to cancer progression, where benign cells are less deformable and malignant cells are more deformable. This change has been generally interpreted as metastatic cancer cells being more capable to translocate through the narrow gaps of adjacent tissue and the epithelial cell layers of blood vessels. Therefore measuring biophysical properties of cells such as compressibility is of great importance to differentiate cancer cells having different metastatic potential. However current methods are low throughput, costly, and usually require expertise for operation. In this work, an acoustic radiation force based system was developed that allowed non-contact measurement of cell biophysical properties. The developed system utilized multi-frequency acoustic resonance simultaneously to allow highly accurate measurement of cell density and compressibility of cancer cells at high throughput using simple instrumentation.

In summary, advancements in acoustofluidic technology enabled solving real world challenges in a wide range of applications, including environmental monitoring, cell biophysics, and cancer metastasis.

DEDICATION

To my dear parents and family for your unconditional love and support.

ACKNOWLEDGEMENTS

I would like to thank my advisor and committee chair, Dr. Arum Han, at the first place for his unwavering guidance and support all the way. Dr. Han has been an exceptional mentor, and given me invaluable encouragement and suggestions throughout my research. I would like to thank my committee members, Dr. Arul Jayaraman, Dr. Byung-Jun Yoon, Dr. Jun Kameoka, and Dr. Yong-Joe Kim for their advice and support. Especially I would like to thank Dr. Kim for his guidance and value input to the project. Also I would like to take a special thanks to Dr. Jayaraman for kindly allowing me to work in their lab.

I would like to take the chance to thank my collaborator, Zhongzheng Liu, for his excellent work and valuable discussion. I also want to thank my group members, Dr. Jaewon Park, Dr. Chiwan Koo, Dr. Sungman Kim, Hyunsoo Kim, Celal Erbay, Adrian Guzman, Nebras Sobahi, Sehoon Jeong, Sergio Castro, Yusuf Dogan, Keith Krenek, and alumni Dr. Mi-Jin Choi, Dr. Changwoo Ban, Dr. Huijie Hou, Dr. Bo Ma, Woosik Kim, Whitney Parker, Osman Safa Cifci, and Jianzhang Wu for their enormous help in the lab and in life. The NanoBio Systems Lab is a wonderful place for research, and a warm family for life. It is my great honor to be part of it.

Thanks also go to my friends and colleagues and the department faculty and staff for making my time at Texas A&M University a great experience. I also want to extend my gratitude to the U.S. Army Corp of Engineer (Engineering Research and

Development Centre (ERDC)) and the National Science Foundation (NSF), which provided the funding for my research.

Last but not least, I would like to thank my parents and my sister for their love and support.

NOMENCLATURE

AFM	Atomic force microscopy
BAEC	Bovine aortic endothelial cell
CsCl	Cesium chloride
DRIE	Deep reactive-ion etching
FDM	Finite difference method
FFA	Free flow acoustophoresis
HNC	Head and neck cancer
IDT	Interdigital transducer
LED	Light emitting diode
$LiNbO_3$	Lithium Niobate
OMA	Oil-mineral aggregate
1-D	One-dimensional
ppb	Parts-per-billion
ppm	Parts-per-million
PDMS	Polydimethylsiloxane
PMT	Photomultiplier tube
PMMA	Polymethyl methacrylate
PRF	Primary radiation force
PCB	Printed circuit board
RBC	Red blood cell

SPLITT	Split flow thin fractionation
SSAW	Standing surface acoustic wave
SAW	Surface acoustic wave
TSAW	Travelling surface acoustic wave
UV	Ultraviolet

TABLE OF CONTENTS

Page

LIST OF FIGURES

Page

LIST OF TABLES

Page

CHAPTER I

INTRODUCTION

1.1. Fundamentals of acoustofluidics

Microfluidic technologies have been utilized in a variety of applications including cell biology, toxicology, energy, and environmental monitoring. Since the dimension of these microfluidic devices are of the same order as cells, it provides a unique opportunity to study the cellular behavior and microscale physical and chemical phenomena. By integrating the function components such as valves, pumps, mixers, and gradient generators, microfluidic devices provide all-in-one platforms to carry out sophisticated experiments, so-called as "lab-on-a-chip".[1-4]

In recent years, acoustophoresis has gained increasing attention in manipulation of cells and particles due to its non-contact nature and efficiency. Also acoustophoresis technology is a label-free method for separation and localization of cells and particles which are affected only by the vibro-acoustic properties of the targets and the medium. These inherent advantages once combined with microfluidic technology, so-called as "acoustofluidics", have proved to be a viable approach in microscale cell and particle handling.[5, 6]

Conventional layered acoustic resonators (or called as planar resonators) are typically configured as a resonance compartment with geometrically designed layers, such as coupling layer, matching (or transmission) layer, fluid layer, and reflector layer

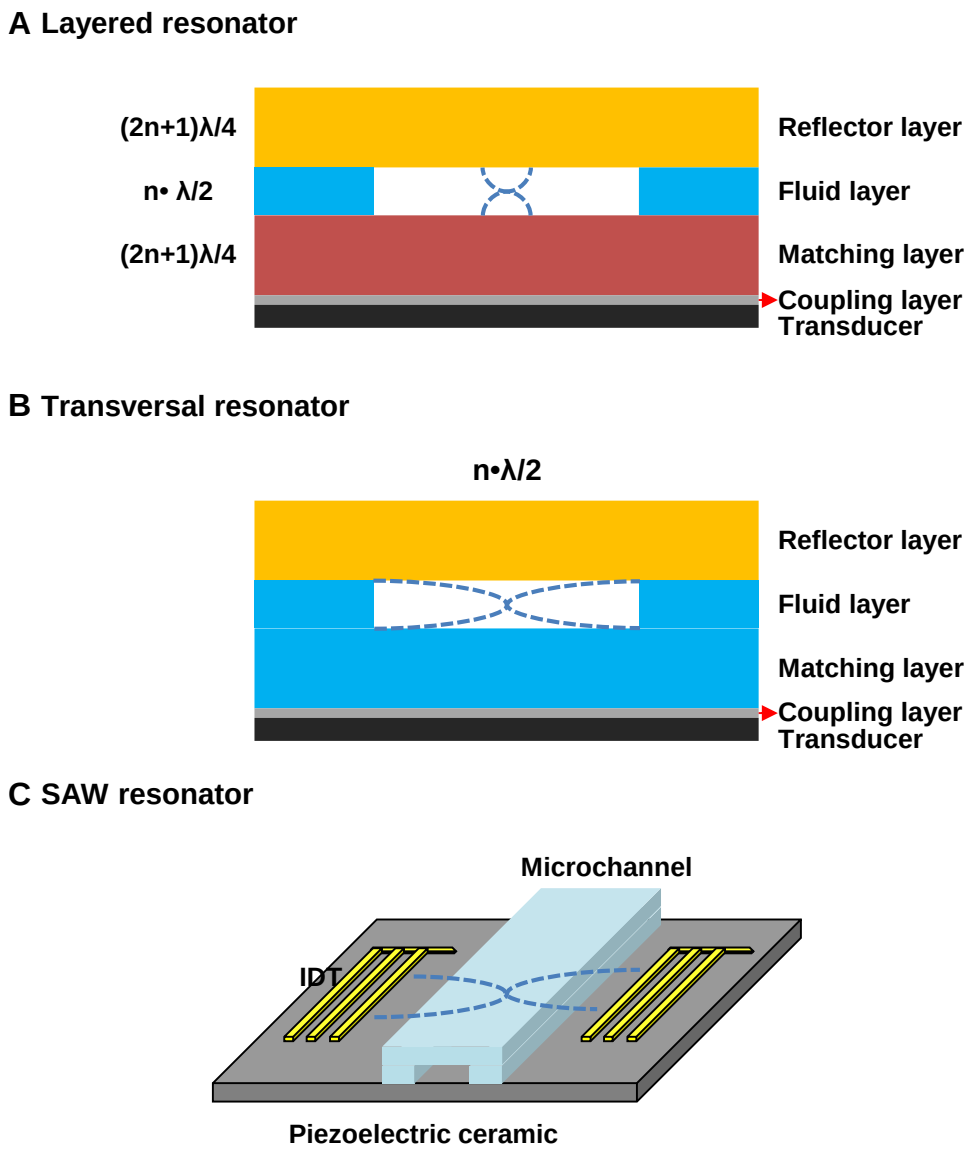

Fig. 1.1 Illustrations of the different configurations of acoustic resonators: (A) Layered resonator, (B): Transversal resonator, (C): Surface acoustic wave (SAW) resonators. (Redrawn from Ref. 6)

(Fig. 1.1A). The thickness of each layer is precisely designed to achieve its specific role. The transducer generates the acoustic wave, which is thereby transmitted to the system through the coupling layer. The matching layer forms the bottom of the resonator chamber, and also serves as the reflector of the acoustic wave. The fluid layer carries the liquid and suspended cells or particles. The reflector layer forms the top of the resonator chamber and reflects the acoustic wave. Another transducer can also be used as the reflector layer, which generates the same frequency of acoustic wave and forms resonance in the chamber. In this configuration, by tuning the phase of the two transducers, the position in relative to the chamber can be changed. Hawkes *et al.* showed in simulation that to maximum the Q-value of the resonator and to compensate for the phase shift during reflection into fluid, the matching layer and reflector should both have quarter wavelength thickness, while the fluid layer should have half wavelength thickness. And the whole system should operate near the piezoceramic's fundamental resonance frequency.[7] In this configuration, the acoustic standing wave is formed by reflections between the matching layer and the reflector layer, thus the material that can be used for the fluid layer is flexible, such as using polymers that have large acoustic attenuation. On the other hand, the matching layer and the reflector layer are usually made of materials that have small acoustic attenuation, such as metals and glass. The system Q-value is mainly determined by the layer thickness.

Another configuration of acoustic resonator is called transversal resonator, in which the acoustic standing wave is formed in the directions perpendicular to the piezoceramic's excitation direction (Fig. 1.1B). In this configuration, the acoustic wave

is reflected between the sidewalls of the fluid channel, which in practice is usually achieved by resonating the whole system as one body. Therefore in the transversal resonator the materials that can be used are limited to those that have small acoustic attenuation, such as silicon, glass, and metals. On the other hand, the thickness for each layer is not important.

The quality of a material as used in acoustic resonators is determined by a term called characteristic acoustic impedance Z, which is the multiple of material density ρ and speed of sound in that material c (eqn (1.1)).

$$Z = \rho c \tag{1.1}$$

A list of characteristic acoustic impedance for different materials is given in Table. 1.1. Thus the layered resonator has the flexibility to use low acoustic impedance materials such as polydimethylsiloxane (PDMS), while the transversal resonator needs to use high acoustic impedance materials such as silicon and glass. The transmission and reflection coefficients can be also calculated using the characteristic acoustic impedance.[8] In the case of normal incidence where the propagation direction of the incident acoustic wave is perpendicular to the interface plane, the reflection coefficient can be calculated as in eqn (1.2).

$$R = \frac{Z_2 - Z_1}{Z_2 + Z_1} \tag{1.2}$$

where Z_1 is the characteristic acoustic impedance of medium 1 and Z_2 of medium 2. the transmission coefficient can be thereby calculated as in eqn (1.3).

$$T = 1 - R = \frac{2Z_1}{Z_2 + Z_1} \tag{1.3}$$

Table 1.1 Density, speed of sound, and characteristic acoustic impedance for commonly used materials. (Rewritten from Ref. 6)

Materials	*Density/kg•m^{-3}*	*Speed of sound/m•s^{-1}*	*Characteristic acoustic impedance/10^{6} kg•m^{-2}•s*
Silicon	2331	8490	19.79
Pyrex	2230	5647	12.59
Steel-stainless 347	7890	5790	45.68
Polymethyl methacrylate (PMMA)	1150	2590	2.98
Polydimethylsiloxane (PDMS)	965	1076 (10:1)*	1.04
H_2O (25 ℃)	997	1497	1.49
PZT	7700	4000	30.8
Air	1	343	0.00034

*: The mixing ratio between base and curing agent is 10:1 for PDMS pre-polymers.

From eqn (1.2) and eqn (1.3), we can have the following conclusions:

1. As the acoustic impedance of two materials get closer, the reflection coefficient decreases, and the transmission coefficient increases. This suggests that materials that have similar acoustic impedance can be treated as the same in acoustic field, such as PDMS and water.

2. For surfaces that need to reflect acoustic waves (matching and reflector layers), the larger the difference of acoustic impedance the better the reflection. This means the reflectors should use high acoustic impedance materials such as silicon or glass or PZT since the fluid layer is typically filled with aqueous solutions.

3. For the reflector layer (or the matching layer as in transversal resonator), air backing provides best reflection efficiency since air has the smallest acoustic impedance.

4. To reduce acoustic loss due to reflection, the adjacent layers need to have matched impedance so that the acoustic energy in the fluid layer is maximized. For example, the matching layer should have lower acoustic impedance than the transducer but higher impedance than the fluid layer.

There is another type of acoustic resonator which is called surface acoustic wave (SAW) resonator (Fig. 1.1C). In SAW devices, the patterned electrodes on the PZT substrate generate acoustic waves propagating into a fluidic compartment. In this configuration, the fluid channels should be comprised of materials that have similar acoustic impedance to water so that the acoustic wave is not interfered with the channel structures.[9-11] Most commonly used substrate is Lithium Niobate ($LiNbO_3$), while the channel is typically constructed of PDMS.

Among these different configurations, transversal resonators has proved to be a powerful and versatile tool in manipulating cells and particles in microfluidic channels due to the simple configuration and easy setup. Layered resonators are mostly in bulk flow or chambers mainly because of the requirement of layer thickness control, and that the vertical actuation is inconvenient to observe. SAW devices have also been reported as a versatile tool and can control the positions of particles within the channels, but are limited to the materials that can be used, the use of high frequency signals, and the temperature control. Therefore the following sections would focus on the transversal resonators while keeping the others in touch.

1.2. Principles of acoustofluidics

The theory of the acoustic standing wave force has been extensively studied by King,[12] Yosioka and Kawasima,[13] Gorkov,[14] and Nyborg[15] among others. King *et al*. presented the acoustic force on a rigid sphere in any field represented (in first-order approximation) by a velocity potential, Yosioka and Kawasima extended the theory to compressible spheres. Gorkov presented a different approach to express the acoustic radiation forces acting on a particle in an arbitrary acoustic field, and Nyborg derived a simple expression for the acoustic radiation force on a small rigid sphere using the method first developed by King.

In an acoustic field, the forces induced on particles include both the primary and secondary radiation forces. The primary radiation force (PRF) in general represent the strongest acoustic forces exerted on suspended particles in an acoustic standing wave.

The secondary radiation force which is induced by the scattering of acoustic waves on particles, on the other hand, is typically orders of magnitude smaller than PRF. Also the secondary radiation force is strongly dependent on the distance between particles, i.e. in cases where the particles density is very high the secondary radiation force should not be neglected.[16]

The primary radiation force can be divided into the axial component and the transverse component (Fig. 1.2). The axial PRF translates the particles into the pressure nodes or anti-nodes depending on the particles vibro-acoustic properties in respect to the medium. The transverse PRF keeps the particles closer and also maintains their positions. Usually the axial PRF is much stronger than the transverse PRF. The axial PRF on a suspended compressible sphere in an arbitrary acoustic field can be expressed using eqn (1.4).

$$F_a = -V_0[\frac{1}{2} f_1 \beta_s \nabla < p_1^2 > - \frac{3}{4} f_2 \rho_s \nabla < v_1^2 >] \tag{1.4}$$

where V_0 is the volume of the particle, p_1 is the acoustic pressure amplitude, v_1 is the acoustic velocity amplitude, β_s and ρ_s are the compressibility and density of the solution, f_1 and f_2 are the pre-factors that are determined as follows.

$$f_1 = 1 - \frac{\beta_s}{\beta_0} \tag{1.5}$$

$$f_2 = 2\frac{\rho_0 - \rho_s}{2\rho_0 + \rho_s} \tag{1.6}$$

where β_0 and ρ_0 are the compressibility and density of the particle. The acoustic contrast factor is given by eqn (1.7).

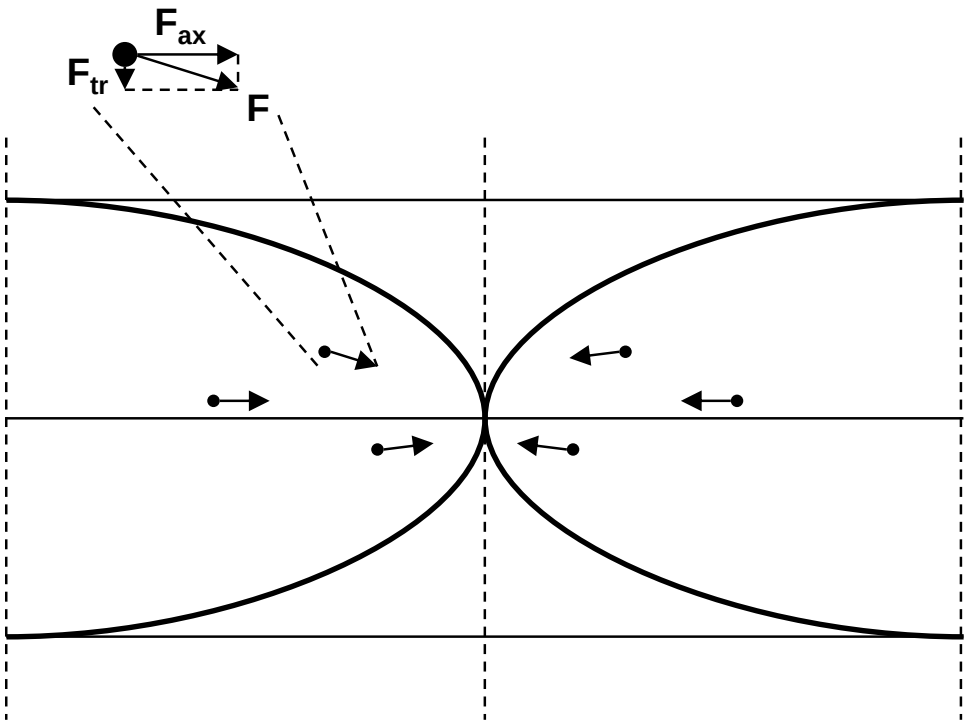

Fig. 1.2 Illustration of the primary radiation force on suspended particles in an acoustic standing wave field.

$$\Phi = \frac{f_1}{3} + \frac{f_2}{2} \tag{1.7}$$

For particles that have positive acoustic contrast factors, the direction of the axial PRF is towards the pressure node. While for particles that have negative acoustic contrast factors, the direction of the axial PRF is towards the pressure anti-node. From the above equations it can be seen that the PRF is determined solely by the acoustic field and the particles' and medium' vibro-acoustic properties such as density and compressibility, and is irrelevant of factors such as pH, ionic concentration, enabling the acoustic manipulation of particles to be used in a broad area of applications. Also the PRF is proportional to the particles' volume, which makes it ideal for separating particles of different sizes.

In the case of a one-dimensional (1-D) acoustic standing wave, the axial PRF can be simplified into the following expression (eqn (1.8)).

$$F_a = -\left(\frac{\pi p^2 V_0 \beta_s}{2\lambda}\right) \Phi(\beta, \rho) \sin(2kx) \tag{1.8}$$

where p is the acoustic pressure amplitude, V_0 is the volume of the particle, β_s is the compressibility of the solution, λ is the wavelength of the acoustic field, k is the wavenumber defined as $2\pi/\lambda$, and $\Phi(\beta, \rho)$ is the 1-D acoustic contrast factor defined by:

$$\Phi(\beta, \rho) = \frac{5\rho_0 - 2\rho_s}{2\rho_0 + \rho_s} - \frac{\beta_0}{\beta_s} \tag{1.9}$$

where ρ_0 and ρ_s are the densities of the particle and solution, respectively, and β_0 and β_s are the compressibilities of the particle and the solution, respectively.

During the movement of the particle to the acoustic pressure nodes or anti-nodes, there is a relative velocity difference between the particle and the solution, inducing a viscous drag force in the opposite direction to the particle motion. In a flow condition with a low Reynolds number (less than 1), the drag force can be expressed by eqn (1.10).[17]

$$F_v = -6\pi\eta a v_r \tag{1.10}$$

where η is the dynamic viscosity of the solution, a is the radius of the particle, and v_r is the relative velocity between the particle and the solution. Here, acoustic streaming velocity induced by the resonant excitation is assumed to be included in the solution flow velocity. Then, the particle motion can be determined by using both the acoustic radiation force and the viscous drag force when the gravitation and buoyancy forces are applied perpendicular to the direction of the acoustic radiation force.

1.3. Previous applications of acoustofluidics

Conventional acoustic resonators have been mostly layered resonators which usually operate in the centimeter to meter dimension and are bulky.[18, 19] Since the introduction of half wavelength resonators as described by Mandralis *et al.*,[20] acoustic resonators started to be utilized in the dimension range of hundreds of micrometers and were ready to be used in microfluidic applications. As discussed in the introduction session, the acoustic resonators include mainly three different configurations, namely layered resonators, transversal resonators, and SAW resonators. In this session the applications of each

configuration will be covered, while most applications will be derived from the transversal resonators.

1.3.1. Layered (planar) resonators

As shown in Fig. 1.1A, layered resonators have been seldom used in microfluidic devices due to the material choice and requirement of thickness control, also the inconvenient visualization of particles manipulation in the vertical direction makes this configuration unfavorable. However, efforts in utilizing this configuration have been spent for efficient particle filtration, trapping, separation and sensing.[21]

Hawkes *et al*. utilized an etched transducer as a continuous flow microparticle filter by combing laminar flow scheme.[22] Harris *et al*. extended the efforts by exploiting microfabricated silicon and Pyrex based device using anisotropic etching as an acoustic filtration device.[23] This type of microfabricated device, though give good performance due to the material property, however is very costly and labor-intensive to fabricate. It was later found that disposable components such as capillaries can be incorporated into acoustofluidic devices for modular fabrication and readily sterilization. Hammarstrom *et al*. demonstrated a contact-less disposable capillary based acoustic cell trapping system in which tedious microfabrication is not necessary.[24] By coupling the disposable capillaries with accurate frequency prediction, the developed system permits disposable usage in biological applications.

Johnson *et al*. developed a size based acoustic particles separation device in which the particles in feed stream were initially introduced near channel sidewalls by

another carrier stream, when the first-order acoustic standing wave was generated the larger particles moved faster to the pressure node in the channel center and were separated by the splitter with the smaller particles which moved slower and exited through the outlet near the initial feed stream (Fig. 1.3).[25] This type of acoustic separation method was later called as split flow thin (SPLITT) fractionation.

Gupta *et al*. showed that by tuning the medium property (e.g. use aqueous glycerol solution) the polarity of acoustic contrast factor for suspended particles can be changed and therefore the particles with different vibro-acoustic properties such as compressibility and density can be separated.[26]

Another method that achieve acoustophoretic particle separation utilized frequency switching, such that the actuation frequency changes in a simultaneous or serial manner to generate different orders of acoustic resonance inside the microchannels. Since the pressure node distribution at different orders of resonance is different, particles of different sizes or other mechanical properties can be separated. Initially developed in layered resonators, Ratier *et al*. showed separation of different size particles using simultaneous application of first and second order resonance frequencies at different locations.[27] Mandralis *et al*. demonstrated separation of particles in a bi-directional flow by switching the frequency between first and second order resonance.[28] Siversson *et al*. showed particle fractionation by switching between first and second order resonance in a continuous flow.[29] Harris *et al*. demonstrated an improved method where particles were first pre-concentrated at channel center using the first order

resonance, and then fractionation of particle sizes was achieved by switching between second and third order resonance.[30]

Hawkes *et al*. showed the use of the reflector layer that was of half wavelength of acoustic wave to translate bacterial spores to the antibody coated glass surface for improved detection efficiency of as high as 200-fold.[31] Townsend *et al*. further explored the technique and demonstrated the capability of a quarter wavelength resonator where the acoustic pressure node is located close to channel surface in concentrating particles to the surface and be used for concentration and sensing.[32]

Kapishnikov *et al*. demonstrated that by placing two transducers on both sides of microchannels with matched distances, acoustic manipulation of particles can be also achieved in polymer based microfluidic devices such as PDMS.[33] This enables the incorporation of acoustophoresis in polymer microdevices.

Other applications include measurement or monitoring of chemical reactions,[34, 35] forming 2-D cell aggregates,[36, 37] and sonoporation.[38-41]

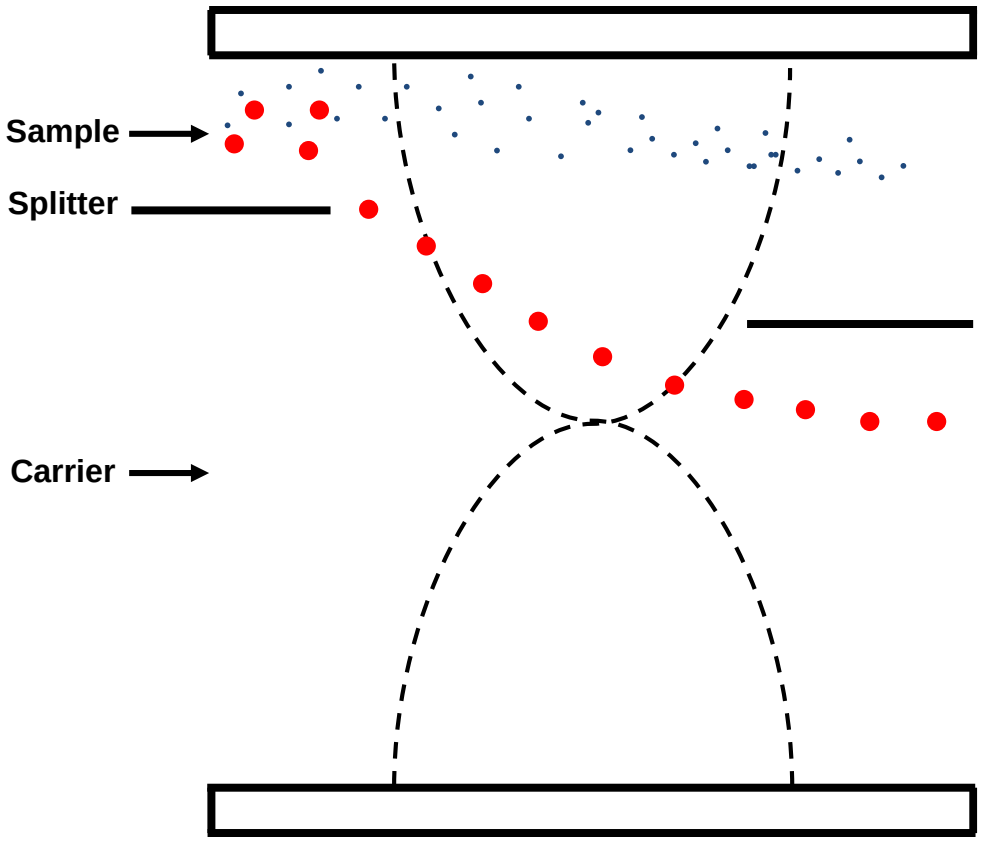

Fig. 1.3 Illustration of the separation scheme for particles of different sizes (red: large, blue: small) with half wavelength resonator in a continuous flow.

1.3.2. Transversal resonators

In transversal resonators (Fig. 1.1B) the acoustic wave reflects between sidewalls of the microchannels, therefore this configuration provides easy visualization of particle manipulation due to acoustic radiation force from the top view. Also, in this configuration the layer thickness doesn't need to be carefully designed and matched; only the channel width determines the resonance frequency. This provides great convenience in designing and assembling acoustofluidic devices, and is an important reason that this configuration got increased attention and popularity. However there is a limitation in the selection of construction materials that only those have high characteristic acoustic impedance can be used, such as silicon and glass. Polymers that are widely used in microfluidic systems such as PDMS are not good resonators. Transversal resonators have been widely used in acoustic particle filtration, separation, trapping, fluidic switching, and measurement of cell mechanical properties.

1.3.2.1. Acoustic filtration

Similar to those described in the layered resonator session, transversal resonators have also been used in particles or cell filtration applications in a continuous flow scheme. However, since in many transversal resonators the fundamental resonance frequency is used the acoustic pressure node is located in the channel center, thus the center stream is removed to obtain purified solutions.

Previously we have used this method for the removal of blood cells from the whole blood to obtain the purified plasma (Fig. 1.4).

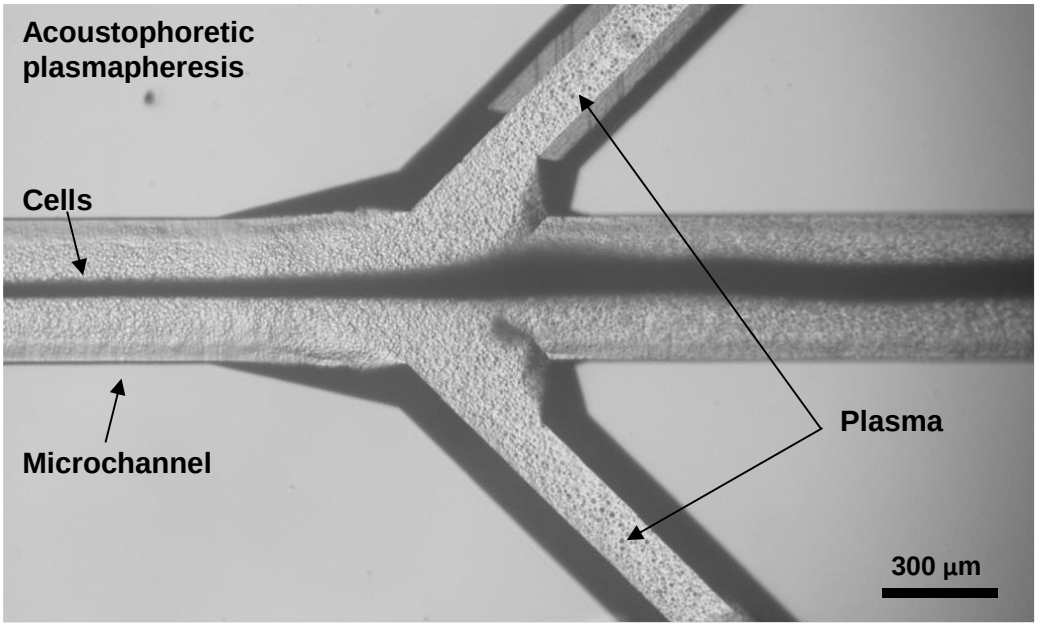

Fig. 1.4 Micrograph of the acoustofluidic device for plasmapheresis. Blood cells were separated into the center stream, while the purified plasma was collected from the side outlets. The device was etched by KOH with the center channel width about 375 μm. Scale bar = 300 μm.

As can be seen in Fig. 1.4, at high concentrations the cells or particles focused at the channel center could be overloaded and exit through the side outlets. Lenshof *et al*. demonstrated an improved strategy where a series of outlet holes were made along the microchannel, so that focused blood cells can be removed gradually through the series of outlet holes, facilitating ultra-pure plasma separation.[42]

1.3.2.2. Acoustic separation

From the equations of acoustic axial PRF, it can be seen that PRF is proportional to particle volume, and is also proportional to the contrast factor which is determined by densities and compressibilities of the particle and medium. Therefore utilizing the different polarity (where the polarity of acoustic contrast factor is changed) and magnitude (mostly with various size, but can be also related to contrast factor) of PRF, particles or cells can be separated.

Petersson *et al*. demonstrated size based particle separation into multiple bands in continuous flow using the free flow acoustophoresis (FFA) method.[43] By tuning the medium property using added cesium chloride (CsCl), separation of leukocytes, erythrocytes, and platelets was also achieved. In the FFA scheme, particle or cell mixtures are introduced from the side inlets while buffer is introduced from the center inlet. By actuating the particles or cells using acoustophoretic force in a region of the straight channel, particles or cells of different vibro-acoustic properties (such as size, density, compressibility) can be separated into different outlets (Fig. 1.5).

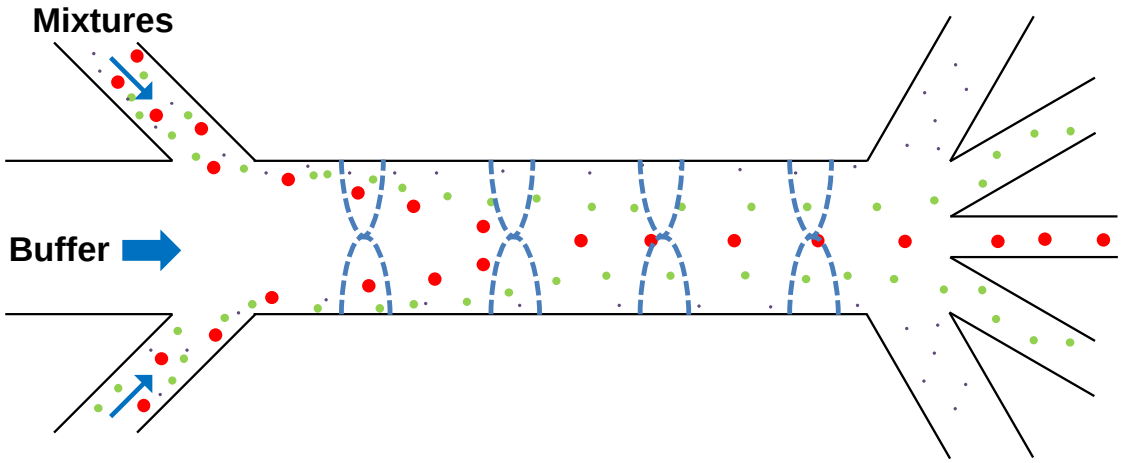

Fig. 1.5 Illustrations of the free flow acoustophoresis (FFA) method. Red: large size particles, green: medium size particles, black: small size particles.

Thevoz *et al*. reported that using the FFA method breast cancer cells (MDA-MB231) of different phases in the life cycle can be separated.[44] Augustsson *et al*. utilized the FFA method to separate circulating tumor cells from white blood cells using a dual outlet device.[45] To achieve separation of particles or cells of multiple sizes, a serial connection of FFA components was reported as multi-band FFA system by Adams *et al*.[46] Here the system operates as a band-pass particles size filter where particles of multiple sizes can be separated independently.

Particle separation by frequency switching has also been performed in transversal resonators. Liu *et al*. demonstrated that in a continuous flow, switching between the second and third order resonance frequency can achieve improved particle fractionation since the two modes share one pressure node at the channel center.[47] Thus by carefully tuning the duty cycle and period for the frequency switching, particles of different sizes can be separated at high efficiency and stability.

1.3.2.3. Acoustic trapping

In acoustophoresis, it is desired that the acoustic potential is along the entire length of the microchannel where the acoustic standing wave is formed. This helps to move particles or cells to the pressure node or anti-node along the flow. However in an acoustic trapping system, it is desired to have localized high acoustic pressure gradient. It was found that the main force involved in acoustic trapping is the transverse PRF, which is typically orders of magnitude weaker than the axial PRF. Also when particles are close during trapping, the secondary radiation force start to play and need to be

considered. The transverse PRF induced by acoustic standing wave on a particle with radius a is given by eqn (1.11).[48]

$$F_{tr} = \pi \rho_s \omega^2 a^2 u_0 u_m \tag{1.11}$$

where ρ_s is the density of the medium, ω is the angular frequency of the acoustic wave, u_0 is the displacement amplitude at the center of the particle, and u_m is the difference of displacement at the edge of the particle compared to at the center. In order to generate high gradient in the lateral direction, either highly localized acoustic field or localized acoustic resonance is utilized in acoustic trapping systems.

A straightforward method to generate localized acoustic field is to use two opposing transducers to focus acoustic waves to a node, which was realized by Wu[49] and Hertz[50], respectively. Using layered resonators as described previously, localized acoustic field can be generated using small transducers coupled to microfluidic channels. Evander *et al*.[51] and Hammarstrom *et al*.[24] developed acoustic particle and cell trapping sites in a fluidic channel by using miniature transducers mounted on a printed circuit board (PCB) to create localized acoustic fields. However these systems require labor intensive manual assembly and are inconvenient for routine use.

Using transversal resonators localized resonance can be generated using fluidic cavities incorporated with acoustic standing wave.[52] A transitional version of this method was developed by Manneberg *et al*.[53] and Svennebring *et al*.[54] using standalone wedge transducers. Wang *et al*. further explored this method and utilized the resonance cavity in trapping and accumulation of crude oil droplets in continuous flow, as shown in this work.[55]

1.3.2.4. Acoustic switching

As acoustic radiation force can be used to manipulate particles in a continuous flow, it is intuitive to implement acoustic standing wave in a multiplex system where the acoustic radiation force acts as the valve to move particles to corresponding outlets. Laurell *et al*. demonstrated switching of particles to four different outlets by using on/off combinations of two piezoelectric transducers.[5] Manneberg *et al*. investigated the cross-talk issue in this kind of systems and found that it is desired to use different channel width at different branches so that the transducers would operate at different frequencies, minimizing the cross-talk issue.[56]

This method can be further explored for cell selection in a continuous flow. When rare target cells are introduced from the side stream in a mixture with other cells, the target can be detected (optically, or electrically.) and then the acoustic standing wave is applied, driving the target cell to the center collection outlet. The throughput would be determined by the acoustic pressure field, cells' mechanical properties, and the flow.

1.3.2.5. Measurement of cell properties

Since the acoustic radiation force is related to the mechanical properties of particles or cells such as density and compressibility, it can be used to study the mechanical properties by evaluating the cell motion in an acoustic standing wave field.

Augustsson *et al*. demonstrated the capability of acoustofluidic systems in measuring the acoustic contrast factors of particles and cells using the 1-D analytical method (eqn (1.8)).[57] Barnkob *et al*. further measured the densities and compressibilities

of particles and cells using the acoustic radiation force in an arbitrary field model (eqn (1.4)).[58] Hartono *et al*. used a similar method to Augustsson's to extract cell compressibilities from the motion of cells in an assumingly 1-D acoustic standing wave field.[59] In all cases the motion of particles and cells were extracted and analyzed using Newton's second law of motion, and the calculated acoustic radiation force was substituted into either eqn (1.4) or (1.8) to calculate particles' and cells' mechanical properties. A difference can be noted that using eqn (1.8) only one unknown factor can be calculated, as in Hartono's work the densities were imported from other works, while using eqn (1.4) the acoustic radiation force is applicable to general acoustic fields and also both density and compressibility can be extracted. Wang *et al*. used the approach similar to Barnkob's with improved 1-D numerical model and demonstrated that cancer cells of different metastatic potential hold different profiles of density and compressibility, where the compressibility plays a more important role, as shown in this work.[60]

1.3.3. SAW resonators

SAW resonators (Fig. 1.1C) utilize a very unique approach where the acoustic wave is generated from patterned electrodes on piezoelectric substrates (such as $LiNbO_3$), while the microchannels are patterned by polymer (such as PDMS) which are bonded to the substrates in respect to the electrodes. SAW resonators offer flexible manipulation of particles since the pressure node positions can be readily tuned by both the frequency and phase of the SAW. There are two main types of SAW devices, namely the travelling

SAW (TSAW) devices and standing SAW (SSAW) devices. TSAW devices rely on the SAW-induced streaming of the surrounding medium to manipulate particle, while SSAW rely on the PRF from the standing wave that is directly exerted on particles.[10]

TSAW has been used for fluid mixing inside a droplet,[61] moving, splitting, merging and mixing of unconstrained droplets,[62] concentrate and separate particles of different sizes inside a droplet,[63] and sorting of droplets or microparticles in a continuous flow.[64, 65] Similar functions have also been achieved using the SSAW technique, such as droplet sorting into multiple outlets in a continuous flow,[66] as well as sorting of microparticles based on either size[67] or density[68]. Ding *et al*. demonstrated manipulation of single particles and cells and *C. elegans* in a stagnant SSAW field using two pairs of chirped interdigital transducers (IDTs).[69] The single particles were trapped using the PRF induced by the SSAW field, once trapped the particles can be moved by changing the frequencies and phases of the constituent SAWs.

This work focused on the utilization of the transversal resonators due to its convenience in assembly and simple setup, also this configuration suits our target of applications in oil droplet trapping and detection and cell mechanical property measurement well. Chapter II will discuss about the development of a continuous flow low concentration oil droplet trapping and detection system, and Chapter III will discuss about the study on measuring cell mechanical properties using acoustofluidic systems.

CHAPTER II

MICROFLUIDIC ACOUSTOPHORETIC FORCE BASED LOW-CONCENTRATION OIL SEPARATION AND DETECTION FROM ENVIRONMENT[*]

2.1. Introduction

Crude oil spills pose severe environmental and economic threats.[70, 71] Thick oil slicks are typically treated with chemical dispersants to be broken down into small oil droplets in the sub-100 μm ranges for rapid dispersion into the ocean.[72] Oil leaked from spills and other chronic discharges also experience a series of naturally-occurring physical and biochemical processes, such as spreading, biodegradation, and oil-mineral aggregate (OMA) formation, which are referred to as "weathering".[73, 74] The weathered oil eventually breaks down into small droplets in the aqua environment. Therefore, in regions away from an initial spill site and also in weathered spill sites, the concentration of oil droplets is lower than 1 parts-per-million (ppm).[75, 76] Large oil spills are usually monitored by microwave or optical sensors carried on satellites, aircrafts, or ships that track thick oil slicks on the surfaces of water.[77, 78] However, detecting and quantifying dispersed oil contents are difficult due to their extremely low concentration, especially in coastal areas where environmental impacts are the greatest.[79] As reported by surveys conducted spanning from May to June of 2010 in the Deepwater Horizon spill in the Gulf of Mexico, after the application of a dispersant, COREXIT 9500 (Nalco Energy

[*] Reprinted with permission from "Microfluidic acoustophoretic force based low-concentration oil separation and detection from the environment" by Han Wang etc., 2014, *Lab Chip*, **14**, 947-956, Copyright [2014] by The Royal Society of Chemistry (http://dx.doi.org/10.1039/c3lc51032h).

Services, TX), the dispersed oil concentration was in the range of 8.1 – 14.5 mgL^{-1} (ppm) at the wellhead measured by fluorescence spectrophotometers, and quickly dropped to less than 1% to the range of parts-per-billion (ppb) at locations 1 km away from the plum.[80-82] Most commercial portable ultraviolet (UV) fluorometers for oil detection utilize the natural fluorescence fingerprints of crude oil excited by UV light, but have limited sensitivities (typically at 0.05 – 1 ppm) and detection volumes (typically at 0.3 – 1 ml).[83-85] To detect oil droplets below the ppm range, complex flow chambers combined with expensive optical instruments are required, and thus not suitable for field deployments.[86] Therefore a low-cost, portable, and highly sensitive system that can be used to quantify low concentrations of oil droplets in marine environment on site as well as sample them for further analyses in laboratory settings with mass spectrometers could have broad implications.

It is proposed that use of acoustophoretic force to first concentrate oil droplets to improve the detection sensitivity and then to separate them from water for further downstream analyses. Particles suspended in a liquid solution experience the acoustophoretic force when exposed to a resonant acoustic standing wave (given that the particles are much smaller than the excitation wavelength), where such force depends on the vibro-acoustic properties of the particles and the surrounding solution.[12-14] The acoustic standing wave forms acoustic pressure nodes (i.e. minimum acoustic pressure points) and anti-nodes (i.e. maximum acoustic pressure points). The particles can then move either to the acoustic pressure nodes or anti-nodes by the acoustophoretic force. The direction of this movement depends on the vibro-acoustic properties of the particles

and the surrounding solution, and can be represented as a constant referred to as the acoustic contrast factor. This force has been utilized in manipulating and separating particles and biological samples such as cells.[5, 43, 87-90] Conventional layered ultrasound resonators are bulky and require a tedious acoustic impedance matching process to achieve accurate matching of the layer thicknesses to form an acoustic standing wave.[91, 92] The recent development of transversal type resonators integrated with microfluidic systems enabled simple implementation of acoustophoretic force based particle manipulation systems.[5] Reported first by Nilsson *et al*., this transversal resonator utilized a piezoelectric transducer attached to the bottom of a silicon/glass microchip to generate planar acoustic standing waves inside the microchannel, and allowed continuous particle separation.[88]

The system presented here utilizes the fact that oil droplets have negative acoustic contrast factors, and thus will move towards the acoustic pressure anti-nodes under acoustic excitations. Petersson *et al*. developed an acoustophoretic force based system for continuous lipid separation from erythrocytes in blood.[90] Due to their positive acoustic contrast factor, erythrocytes in blood moved towards the acoustic pressure nodes in an acoustic standing wave field, while the lipid particles moved towards the pressure anti-nodes due to their negative contrast factor, and thus could be separated from the erythrocytes.

To concentrate oil droplets from continuously flowing water samples as needed in our application, an acoustophoretic trapping structure was designed to have acoustic pressure anti-nodes away from the main flow so that oil droplets could be moved and

trapped at the pressure anti-nodes. This concept is similar in principle to a few acoustophoretic particle trapping schemes that utilized localized acoustic resonance in trapping regions.[24, 51, 53, 54] Manneberg *et al*.[53] and Svennebring *et al*.[54] demonstrated that the retention and trapping of particles and cells could be achieved in a circular-shaped resonance cavity. However, the acoustic standing wave was created by using stand-alone wedge transducers, which are bulky and cannot be easily integrated into compact and portable acoustic actuation systems.[93] Evander *et al*.[51] and Hammarstrom *et al*.[24] developed acoustic particle and cell trapping sites in a fluidic channel by using miniature transducers mounted on a printed circuit board (PCB) to create localized acoustic fields. However, this method could not be easily integrated with other microfluidic operations and required labor-intensive manual assembly for the miniature transducers. Most importantly, none of these acoustophoretic trapping schemes has been applied to selectively trap particles having negative acoustic contrast factors such as crude oil droplets as presented in this paper.

Manipulation of droplets using acoustophoretic force can be also achieved by using both Rayleigh surface acoustic wave (SAW) and standing surface acoustic wave (SSAW).[10, 64, 66] Franke *et al*. demonstrated droplet and particle sorting using SAW generated by interdigital transducer (IDT).[64] In this work, acoustic streaming in the bulk fluid surrounding the droplet or particle generated by applied high frequency acoustic wave deflected the droplet or particle trajectory to achieve successful separation. Li *et al*. utilized chirped IDT to generate SSAW with excellent tunability and controllability for droplet sorting.[66] The acoustic radiation force directly applied to droplets allowed fast

sorting in a wide range with multiple outlets. Even though SAW-based droplet manipulation provides more flexibility in droplet manipulation, such systems require specialized substrates that are typically much more costly than utilizing a piezoelectric transducer and bulk acoustic wave. Thus in cases where only simple separation or trapping of droplets are required, bulk acoustic wave based systems can provide more advantages.

Here a round-shape acoustic resonance cavity in a microfluidic channel operating in the transversal mode was developed for oil droplet trapping. The presented microfluidic system is the first low-concentration oil droplet accumulation, detection, and separation system based on the acoustophoretic force. Oil droplets in water samples could be trapped and concentrated, and detected with a custom-built compact fluorescent detector. The trapped oil droplets could thereby be sampled for further off-chip analyses such as conducting fluorescence spectrum analyses or gas chromatography to identify the collected crude oil compositions and their origins that are important in oil spill detections.

2.2. Principles of acoustophoretic manipulation of oil droplets

A particle suspended in a liquid solution where an acoustic standing wave is formed experiences an acoustic radiation force, which is also referred to as the acoustophoretic force given in eqn (2.1) in the case of an one-dimensional (1-D) acoustic standing wave.[12-14] The equations have been discussed in Chapter I, and here the 1-D case is used

for oil droplet manipulation. The acoustophoretic force acts along the y-axis perpendicular to the flow direction (x-axis): i.e.,

$$F_a = -\left(\frac{\pi p^2 V_0 \beta_s}{2\lambda}\right)\Phi(\beta,\rho)\sin(2ky) \tag{2.1}$$

where p is the acoustic pressure amplitude, V_0 is the volume of the particle, β_s is the compressibility of the solution, λ is the wavelength of the acoustic field, k is the wavenumber defined as $2\pi/\lambda$, and $\Phi(\beta,\rho)$ is the acoustic contrast factor defined by:

$$\Phi(\beta,\rho) = \frac{5\rho_0 - 2\rho_s}{2\rho_0 + \rho_s} - \frac{\beta_0}{\beta_s} \tag{2.2}$$

where ρ_0 and ρ_s are the densities of the particle and solution, respectively, and β_0 and β_s are the compressibilities of the particle and the solution, respectively. Thus, depending on the properties of the particle and the surrounding solution, the acoustic contrast factor can have either a positive or negative value. The polarity of this acoustic contrast factor determines whether the particle moves to acoustic pressure nodes (for a positive contrast factor) or anti-nodes (for a negative contrast factor). Since oil droplets in water have negative contrast factors, they move towards the pressure anti-nodes of an acoustic standing wave (Fig. 2.1A).

The viscous drag force in a flow condition with a low Reynolds number (less than 1), can be expressed by eqn (2.3), which is proportional to the particle's radius and the relative velocity.[17]

$$F_v = -6\pi\eta a v_r \tag{2.3}$$

where η is the dynamic viscosity of the solution, a is the radius of the particle, and v_r is the relative velocity between the particle and the solution.

In order to generate the high-level resonant acoustic fields in the transversal mode, a piezoelectric transducer is usually attached to the bottom of a microchip containing a microfluidic channel, and excited at the first resonance frequency of the microchannel. In a straight microchannel, one or two of the parallel sidewalls of the microchannel can be excited at the first resonance frequency whose one half-wavelength is equal to the channel width to generate a 1-D acoustic field as in eqn (2.1). As for a circular chamber, it is similar to the 1-D straight channel case except that the circumferential sidewalls of the chamber serve as the excitation surfaces. Although the excitation surface is not a plane surface, it can generate acoustic fields resembling the "1-D" acoustic fields due to the rigid boundary conditions on the sidewalls. In this case, the acoustic pressure anti-nodes are formed at the sidewalls while the node is at the center of the chamber. The oil droplets having negative acoustic contrast factor and flowing into this circular chamber thus move towards the circumferential sidewalls of the circular chamber (i.e. acoustic pressure anti-nodes) and be trapped there due to the acoustophoretic force (Fig. 2.1B). An additional benefit of this configuration is that the oil droplets trapped near the sidewalls can avoid the high flow rate region of the chamber center, and thus effective trapping can be achieved by reducing the fluidic drag force.

2.3. Design and fabrication

2.3.1. Design

As shown in Fig. 2.1C, the developed acoustic oil droplet quantification system consists of a circular chamber for oil droplet trapping and detection, microfluidic inlet and outlet

channels for the circular chamber, and a downstream microchannel coupled with a trifurcation outlet for separating the concentrated oil droplets into the collection outlet upon release from the trapping chamber. Two piezoelectric transducers are attached underneath the trapping chamber and the separation channel areas, respectively, to generate the acoustic standing waves in the corresponding areas of the microchip at two different frequencies.

The circular chamber is designed to be 750 μm in diameter and the corresponding first resonance frequency was tuned to 1.00 MHz. The microfluidic channels connecting the circular chamber are designed to be 125 μm in width, and the downstream separation channel is designed to be 350 μm wide for separating the concentrated oil droplets at the first half-wavelength frequency of 2.14 MHz. The downstream channel width was selected to avoid crosstalk with the circular acoustic trapping chamber by deviating sufficiently away from a channel width that corresponds to higher order harmonic resonance frequencies of the circular trapping chamber.

The circular trapping region also serves as the optical oil droplet detection zone. A custom-made compact fluorescent detector is aligned to the circular trapping chamber and focused on the fluidic channel plane for the detection and quantification of the accumulated oil droplets.

2.3.2. Microchip fabrication

The microchannel was fabricated in silicon by using reactive-ion etching (Oxford Plasmalab 100 ICP RIE) to a depth of 100 μm, and covered with a borofloat coverglass

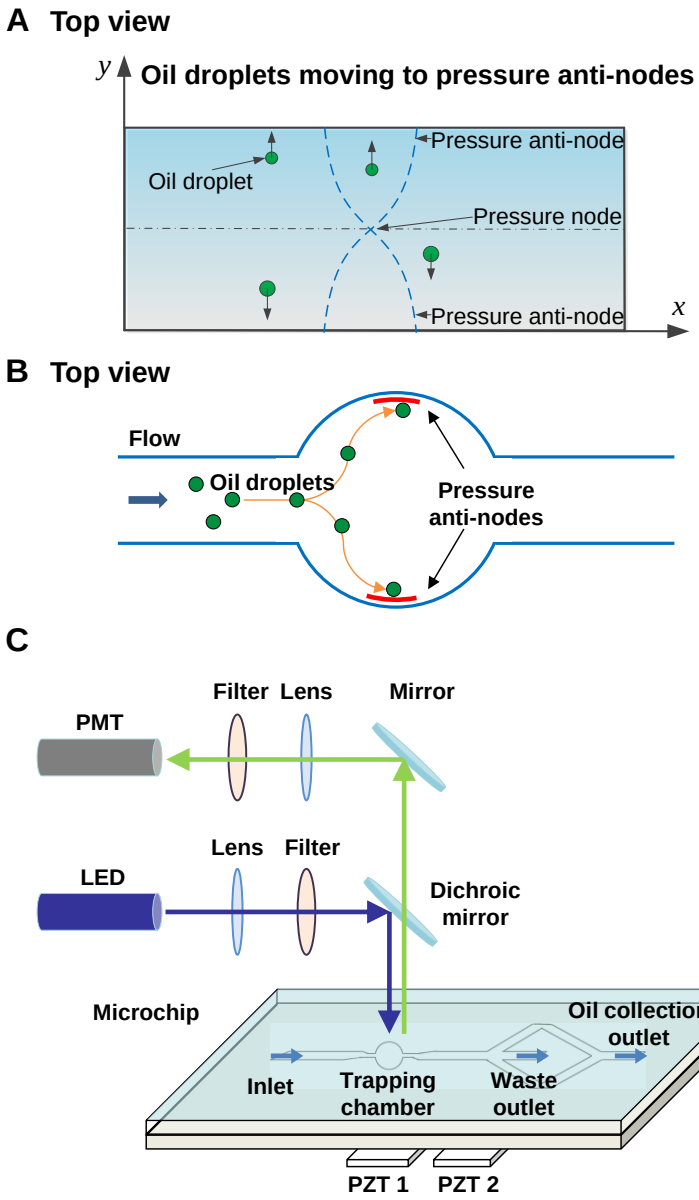

Fig. 2.1 Illustration of the acoustophoretic oil droplet trapping, detection, and separation scheme. (A) Due to their negative acoustic contrast factor, oil droplets experience the acoustophoretic force towards the acoustic pressure anti-nodes that are formed near sidewalls of the straight, half-wavelength resonator at the first acoustic resonant frequency. (B) In the circular chamber, the acoustic pressure anti-nodes form at the sidewalls, where the oil droplets are trapped. (C) Schematic of the microfluidic oil droplet trapping/separation chip aligned to the compact fluorescent detection module. The oil droplets trapped in the circular chamber were excited by a light emitting diode (LED) and the emitted fluorescence light was collected by a photomultiplier tube (PMT) and recorded by an in-house LabVIEW™ program. The concentrated oil droplets could be then released from the trapping chamber and separated into the collection outlet by using another piezoelectric transducer for further off-chip analyses.[55]

by using anodic bonding. The fabricated trapping chamber had a diameter of 745 μm and the separation microfluidic channel in the downstream of the trapping chamber was 345 μm wide. Fluidic access holes were drilled in the coverglass using a bench drill press (DP101, Ryobi Ltd, SC), and connected via flat-bottom ferrules (P-200N, Upchurch Scientific, WA) to Tygon® tubing (Saint-Gobain Performance Plastics, OH). The two piezoelectric transducers (PZ26, Ferroperm Piezoceramics A/S, Denmark) were attached to the bottom of the microchip at desired positions by using wax (Crystalbond™ 509, SPI Supplies/Structure Probe Inc., PA) instead of permanent glue so that the microchip could be recycled.

The T-junction droplet generators to produce oil-in-water emulsions as a pseudo sample of oil spills were fabricated in polydimethylsiloxane (PDMS, Sylgard® 184, Dow Corning Corp., MI) using soft lithography. The master molds were fabricated in negative photoresist (SU-8, MicroChem Corp., MA) on a silicon substrate using standard photolithography. PDMS was then poured onto the master molds and cured at 80 ℃ for 2 hours. The cured PDMS replicas were then released from the master molds and access holes were punched before bonding to a glass substrate using oxygen plasma. The fabricated PDMS droplet generators were rinsed with DI water and coated with surfactant (Pluronic F-108, 2% w/v in DI water, Sigma-Aldrich Inc., MO) in a 37 ℃ incubator for 1 hour prior to test.

2.4. Oil droplet generation

Crude oil sample from Midland, Texas was used to generate the oil-in-water droplets using the microfabricated T-junction droplet generators. The oil droplets with diameters of 14, 32, and 62 μm were generated and used as pseudo reference samples. Samples taken from a weathered oil spill site typically contains oil droplets and oil-mineral aggregates mainly in the range of 10 – 50 μm in diameter, which fits well within the range of the pseudo samples used here.

A series of the T-junction droplet generators (Fig. 2.2) with different channel widths and heights were fabricated to generate the oil droplets of different sizes. The flow rates of crude oil and buffer solution (DI water with 2% v/v Tween® 20 surfactant) (Sigma-Aldrich Inc., MO) were adjusted to obtain the desired droplet generation frequencies and droplet sizes. The oil droplets of 14 μm in diameter were generated by flowing buffer solution at 100 μl/hr and crude oil at 1 μl/hr in a T-junction device with both channel width and height of 15 μm. The oil droplets of 32 μm in diameter were generated by flowing buffer solution at 200 μl/hr and crude oil at 3 μl/hr in a T-junction device with both channel width and height of 30 μm. The oil droplets of 62 μm in diameter were generated by flowing buffer solution at 300 μl/hr and crude oil at 5 μl/hr using a T-junction device with both channel width and height of 60 μm.

The droplet generator chip and the acoustic oil detection chip were connected with a 0.25 mm inner diameter tubing to directly inject the generated oil droplets into the detection chip. To characterize the relationship of required power for acoustic trapping and flow rate, a syringe pump (Pico Plus, Harvard Apparatus, MA) was used to inject

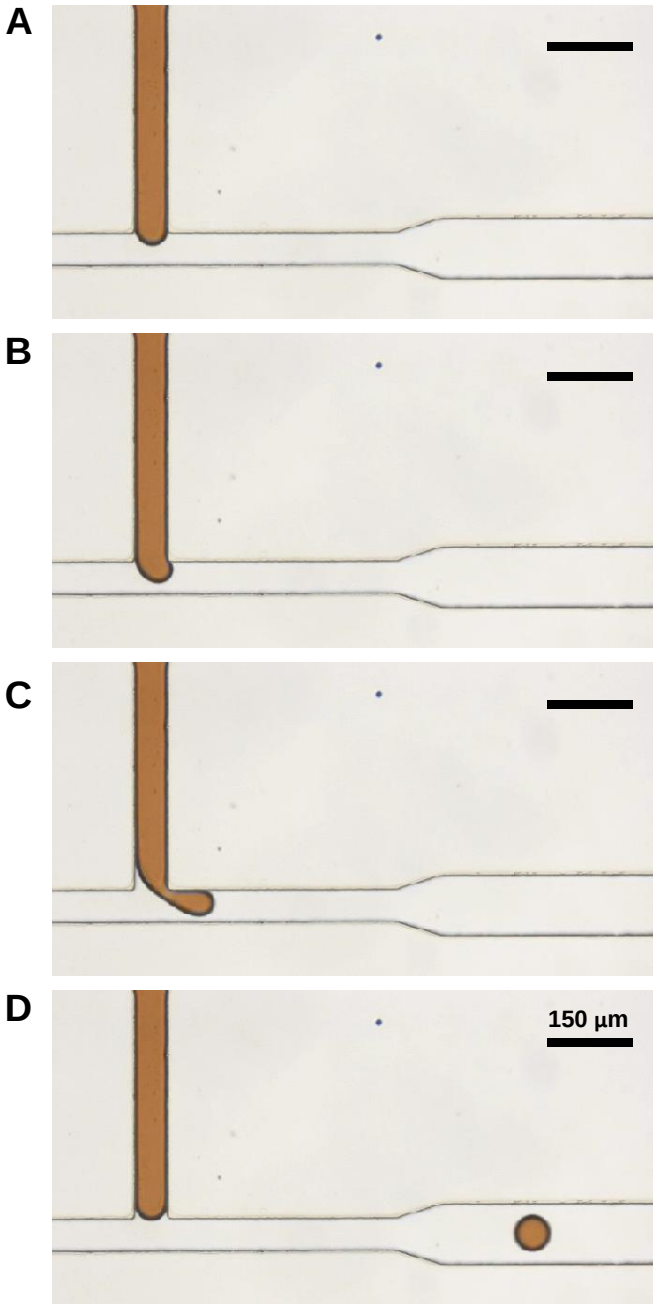

Fig. 2.2 T-junction droplet generator for crude oil droplet generation. (A-D) Time-lapse microscopic images showing the process an oil droplet breaks from the oil sample in buffer. The channel width in the above images is 60 µm. Scale bar = 150 µm.

the generated oil droplets at various flow rates. Two different droplet generation frequencies were utilized. For the single oil droplet trapping and detection experiments, approximately 1 droplet/sec, which represents 1 droplet passing through the trapping region of the acoustophoretic chip a second, was generated. For the oil droplet accumulation experiments, approximately 5 – 10 droplets/sec were generated.

To better resemble real oil spill samples, oil droplet mixtures having various sizes of oil droplets were generated by stirring crude oil in water using a magnetic bar. Crude oil of 500 µl was mixed with 25 ml DI water (pre-mixed with 2% v/v Tween® 20 surfactant), and stirred for 15 min at 300 rpm. The generated oil droplet mixtures were injected into the acoustic oil detection chip by a syringe at a flow rate of 300 µl/hr.

2.5. Acoustophoretic oil droplet trapping

2.5.1. Experimental method

Sinusoidal waves from a function generator (DG4102, Rigol Technologies Inc., OH) was supplied to the piezoelectric transducers via a 40 dB power amplifier (406L, Electronic Navigation Industries Inc., NY) to generate the acoustic standing wave inside the microfluidic device. For oil droplet trapping, sinusoidal waves with amplitude of approximately 100 – 400 mV was applied from the function generator, while for oil droplet separation, about 20 – 50 mV was applied. For the fabricated circular trapping chamber with a diameter of 745 µm, a 1.01 MHz sinusoidal wave was applied to obtain the first resonant acoustic standing wave.

Once all the oil droplets were collected in the trapping chamber and optically quantified, the piezoelectric transducer under the trapping chamber was turned off and the oil droplets were released and carried downstream with the buffer solution. The second transducer in the downstream channel was then turned on and the concentrated oil droplets were separated into the collection outlet at the trifurcation outlet. The separation fluidic channel width was 345 μm, resulting in the first resonance frequency of 2.18 MHz. This was distinctive from the first and higher order resonance frequencies of the trapping chamber to avoid any potential cross-talk.

2.5.2. Trapping of single crude oil droplets

To characterize crude oil droplet movement and trapping, the 62 μm diameter oil droplets were flown through the circular trapping chamber at a flow rate of 200 μl/hr (i.e., the inlet velocity of 4.44 mm/sec) and at a frequency of approximately 1 droplet/sec. This relatively slow flow speed was used to observe single oil droplet movement in the trapping chamber with the piezoelectric transducer turned on and off. The top row images in Fig. 2.4 show a single oil droplet travelling through the trapping chamber when the piezoelectric transducer was off. The bottom row images show a

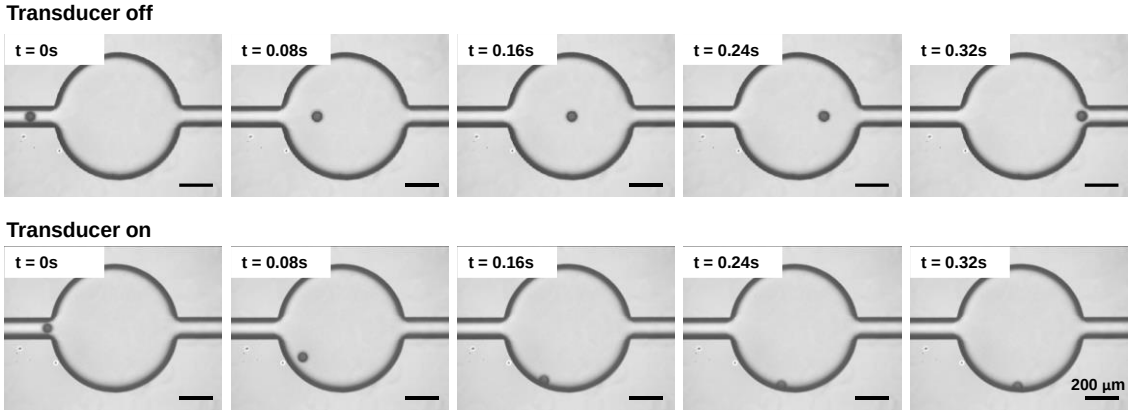

Fig. 2.3 Demonstration of acoustophoretic oil droplet trapping inside the circular trapping chamber. Time-lapse images show a single oil droplet (diameter: 62 µm) passing through the circular chamber when the acoustic transducer was turned off (top row), and being trapped in the circular chamber when the acoustic transducer was turned on (bottom row). Scale bar = 200 µm.[55]

single oil droplet being successfully trapped on the sidewall of the chamber with the transducer on.

2.6. Optical detection of accumulated oil droplets

2.6.1. Experimental setup for optical detection

The compact fluorescent detection module (Fig. 2.1C) was aligned to the trapping chamber for recording the fluorescence intensity increase as the oil droplets were trapped inside the chamber. This allowed quantification of the oil droplet concentrations in the sample. The fluorescent detection module was composed of a blue LED (excitation peak at 470 nm, NSPB310B, Nichia, Japan) for excitation, an excitation filter (ET470/40x, Chroma Technologies, VT) to pass only blue spectrum to excite the oil droplets, a dichroic mirror (495DCLP, Chroma Technologies, VT) to direct the excitation light on the trapping chamber, an emission filter (ET535/50m, Chroma Technologies, VT) to transmit only the emitted light from the oil droplets, and a compact photomultiplier tube (PMT, H10721, Hamamatsu, Japan) for fluorescence emission collection. An NI data acquisition module (NI9219 DAQ, National Instruments Inc., TX) was used for recording the fluorescent intensity from the PMT, and export the data to a custom LabVIEW™ (National Instruments Inc., TX) program. The entire detection module was securely enclosed in a plastic housing fabricated by a 3-D material printer (ULTRA®, Envisiontec Inc., MI, USA). To monitor the oil droplet trapping and separation characteristics, an upright fluorescent microscope (LV100, Nikon Instruments Inc., NY) with a digital camera was used.

2.6.2. Oil droplet accumulation and detection

Small oil droplets of 14 μm in diameter were used to characterize the accumulation and quantification of oil content in water samples since they represent the typical size of oil droplets or oil- mineral aggregates in natural spill samples. Larger oil droplets will require less power to be trapped since the acoustophoretic force is proportional to the volume of the droplets at the same input power as shown in eqn (2.1). Brightfield and fluorescent time-lapse microscopic images show oil droplets being accumulated inside the circular trapping chamber when excited at the first resonance frequency (Fig. 2.5A,). Consistent with the simulated trajectories (Fig. 2.3B), the oil droplets were successfully trapped and accumulated at the top and bottom poles of the circular trapping chamber where the pressure anti-nodes were formed and gradually expanded into a semi-circular pattern.

Then, the fluorescent intensity from the trapped oil droplets was measured by placing the microfluidic chip on the custom-built compact fluorescent detector module. When the system was operating in the trapping mode, the gradually accumulated crude oil droplets (Fig. 2.5A) contributed to the gradual increase in the measured fluorescent intensity. Once the system was turned off, the oil droplets were released as represented by the sharp decrease in the measured fluorescent intensity (Fig. 2.5B).

The current setup based on the highly sensitive PMT has the capability to detect even a single 14 μm diameter crude oil droplet without trapping it. However, the acoustic trapping scheme was still of central importance in the developed oil droplet

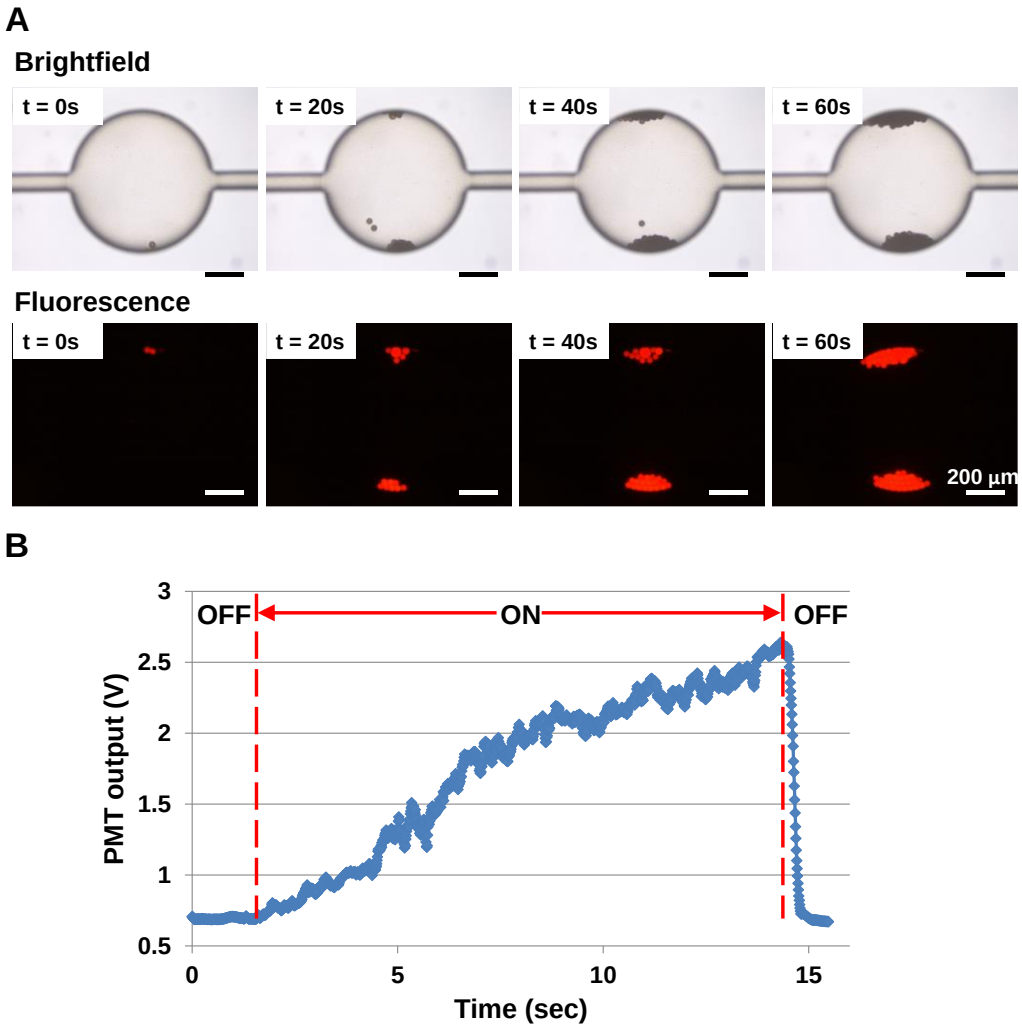

Fig. 2.4 Optical detection of oil droplets based on their natural fluorescence. (A) Time-lapse brightfield and fluorescent images showing oil droplets (diameter: 14 µm) being trapped and accumulated over time in the circular trapping chamber. (B) Fluorescent intensity increased over time as oil droplets accumulated inside the circular trapping chamber, and decreased when the trapped oil droplets were released from the trapping chamber.[55]

detection system. First, for portable oil spill detection systems, the capability of collecting samples for off-chip analyses is crucial. Second, the ultimate goal is to develop a low-cost system where the use of a low-cost photodiode is desirable instead of a PMT. Thus, trapping oil droplets to a detectable level is necessary. Third, at the higher flow rate that is required to achieve higher sample processing throughput, the data acquisition module may not properly resolve a single droplet for quantification. Thus the oil droplet trapping approach was implemented in our design.

2.6.3. Oil droplet trapping threshold and detection sensitivity

Based on eqn (1), the acoustophoretic force is proportional to the acoustic pressure amplitude and the particle's volume, density, and compressibility. Therefore, oil droplets of different sizes experience different acoustophoretic force amplitudes in a resonant acoustic standing wave, requiring different levels of acoustic excitation for successful trapping. The input power requirement was characterized with the oil droplets of three different sizes (14, 32, and 62 μm in diameter) at varying flow rates (0.25 to 2 ml/hr) (Fig. 2.6). The threshold voltage was defined as the input voltage into the RF power amplifier that provided 100% oil droplet trapping efficiency for a given condition. As expected, smaller oil droplets required larger threshold voltages at the same flow rates. As the flow rate increased, the required threshold voltage also increased in a quasi-linear fashion, revealing the need for a larger acoustophoretic force as the fluidic drag force increased.

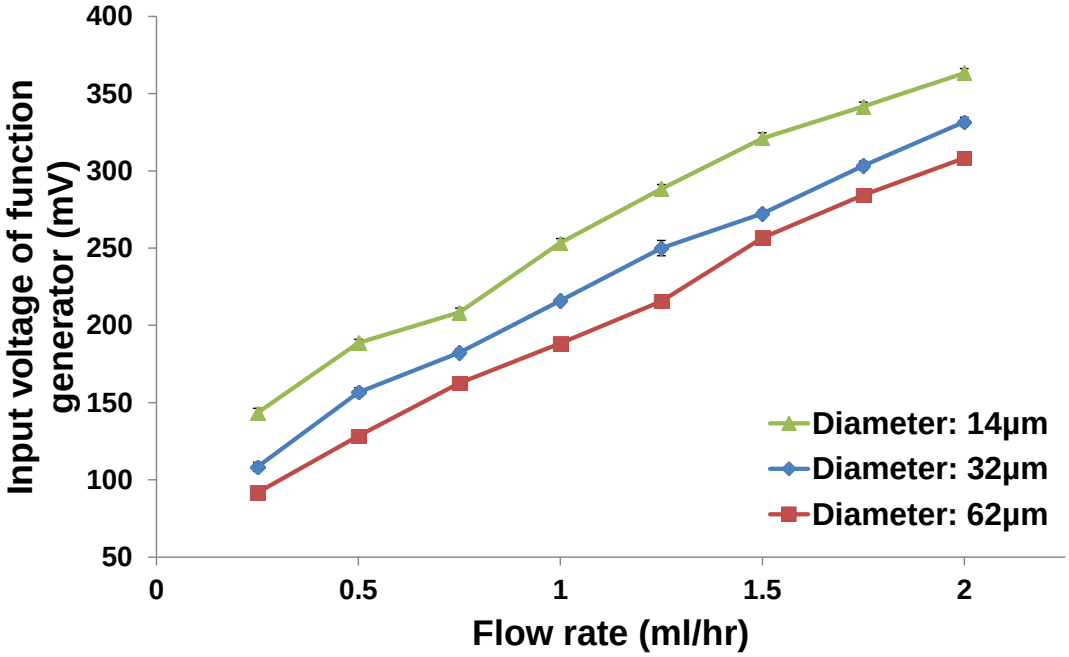

Fig. 2.5 Threshold input voltage to PZT for complete trapping. This experiment measured the minimum power needed to trap oil droplets of various sizes in the circular trapping chamber with 100% efficiency. For oil droplets with the diameters of 14 µm, 32 µm, and 62 µm, the threshold input voltage required to drive the piezoelectric transducer via the 40 dB power amplifier was characterized as a function of the flow rate in the range of 0.25 – 2 ml/hr. Data represents average ± STD (*n* = *3*). Error bars are not visible in this graph since they are smaller than the marker size.[55]

This continuous-flow oil droplet detection scheme with integrated trapping pattern facilitated highly sensitivity detection of oil droplets. The current maximum flow rate of 4 ml/hr and the capability of resolving a single 14 μm diameter oil droplet represent a detection sensitivity of 0.36 ppb oil content in water samples when running the system for 1 minute. This detection sensitivity can be further improved by utilizing for example multiple chambers in parallel to process more sample volumes for a given time.

2.6.4. Trapping and detection of poly-dispersed oil droplets

Pseudo oil spill sample of poly-dispersed oil droplet mixtures were successfully trapped and detected by the acoustic oil detection chip (Fig. 2.7). Oil droplets with significantly different sizes, ranging from 5 to 70 μm in diameter, were generated (Fig. 2.7A left). When the acoustophoretic force was applied, oil droplets of different sizes were all trapped and accumulated in the circular chamber (Fig. 2.7A right). This was further validated by fluorescence detection using the compact fluorescent detector. When the transducer was turned on, oil droplets started to accumulate and thus resulted in rapid increase in fluorescent intensity (Fig. 2.7B). When the piezoelectric transducer was turned off, the intensity dropped instantly as the trapped oil droplets were released.

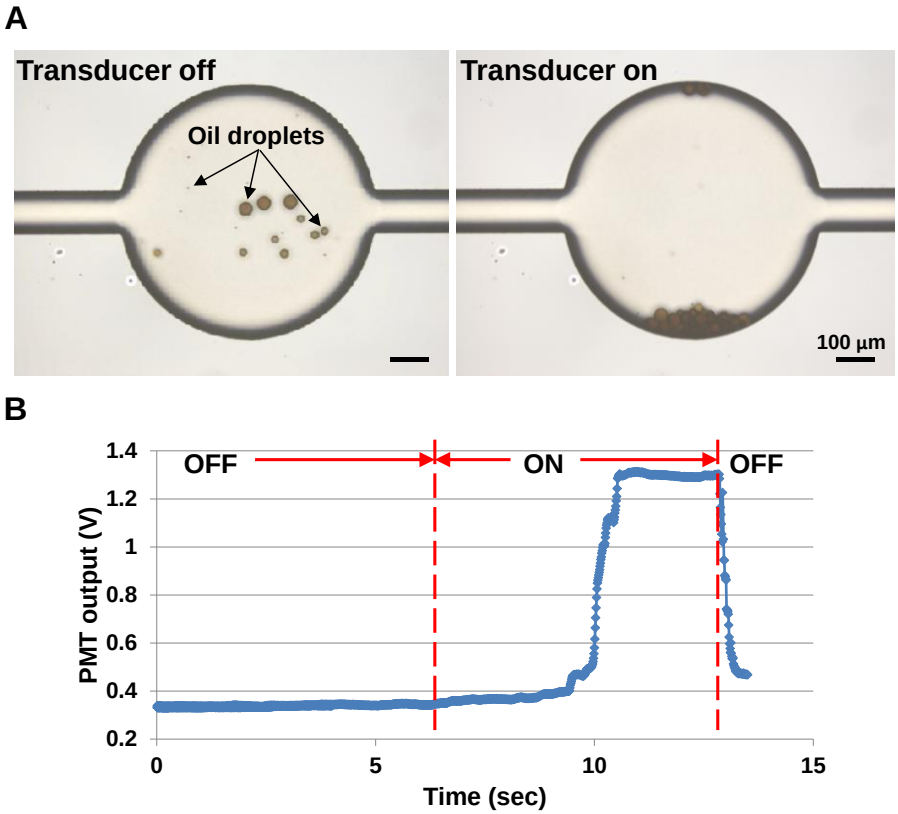

Fig. 2.6 Trapping and optical detection of pseudo oil spill sample containing mixtures of oil droplets having different sizes. (A) Brightfield images showing oil droplets of varying sizes passing through when the transducer was turned off (left) and then being trapped by the acoustophoretic force when the transducer was turned on (right). (B) Detected fluorescent intensity increased as oil droplets were trapped and accumulated, and decreased as oil droplets were released by turning off the transducer and flushed away with flow.[55]

2.7. Acoustic oil droplet separation

Once the oil droplets from the water samples were trapped and quantified, they were released by turning off the first piezoelectric transducer in the circular trapping region and separated in the downstream separation channel by turning on the second piezoelectric transducer (driven at 2.18 MHz) to collect the accumulated oil droplets. The released oil droplets moved towards the acoustic pressure anti-nodes near the sidewalls of the separation channel and flowed into the collection outlet. Collecting concentrated oil droplets from water samples can make the downstream off-chip physicochemical analyses easier since no extra pre-concentration step is needed. For example, the chemical compositions and spectra of the detected oil droplets can be analyzed using gas chromatography and spectrometry.[82]

2.8. Discussions

The developed acoustophoretic oil droplet detection system demonstrated the successful trapping, detection, and separation of crude oil droplets generated by a T-junction droplet generator. The oil-in-water droplets closely resemble the natural spill samples in terms of their sizes and concentrations, which are the key factors affecting the oil trapping and detection from water samples. Depending on the origins of oil spills and weathering processes, oil droplets possess different chemical compositions and show different fluorescence spectrums.[74, 94] Therefore, even for the same amount, oil droplets from different types of crude oil would exhibit different levels of fluorescent intensity. Thus without advance knowledge of the fluorescence properties of oil droplets, a

calibration process to determine the relationship between the oil concentration and fluorescence intensity is typically needed prior to field test. The microfluidic system presented here provides the capability for accumulating and concentrating sufficient amount of oil samples for off-chip analyses that can be used for such crude oil identification based on their fluorescent signatures. The system also provides the potential for on-chip optical spectroscopy since the accumulated oil droplets will provide sufficient sensitivity for even low-cost spectroscopy instrument.

Real seawater may contain many debris and particles. Larger particles can be easily pre-filtered using simple filtration systems (e.g., mesh filter), however smaller sub-100 μm dust particles can come into the acoustic device. Dust particles in seawater are expected to mostly possess positive contrast factor, and thus would be trapped in the chamber center. However even if particles are accumulated in center part of the chamber, because of their relative small size compared to the overall chamber size, we do not expect to see any significant interference to the flow or generated acoustic standing wave. Moreover, the detection of oil content depends on the autofluorescnece of crude oil at a particular wavelength range, which in most cases does not exist in other particles. Overall, the trapping and detection of oil droplet is most likely not affected by other particles that may exist in the seawater.

The developed acoustic oil droplet separation and detection system demonstrated the potential for a new type of low-cost portable oil content detector. In the current form, a bench-top power amplifier was used, but in the future can be replaced by a compact amplifier circuit on a printed circuit board (PCB). This PCB-based power amplifier

currently under development in our lab would enable fabricating a completely portable acoustic oil detection system for field deployment. By using the acoustic trapping strategy, a low-cost photodiode can replace the currently used PMT that is both significantly pricier and heavier than a photodiode. Changing the excitation LED and the corresponding filter sets to have a peak excitation at approximately 300 nm can give even stronger fluorescence emission from the trapped crude oils, thus increasing the detection sensitivity.[85]

Overall, the developed microfluidic device is a broadly applicable platform for trapping, concentrating, detecting, and separating not only crude oils but also other samples of interest that have negative acoustic contrast factors.

CHAPTER III

MEASUREMENT OF CELL BIOPHYSICAL PROPERTIES USING ACOUSTOPHORETIC FORCE

3.1. Introduction

Measurements of biophysical properties of cells such as their Young's modulus or compressibility (bulk modulus) are of great importance in understanding mechanobiology as well as of interest as a potential diagnostic biomarker. Biophysical properties of cells have been found to be associated with cell differentiation and disease progression. For example, using atomic force microscopy (AFM), Cross *et al*. demonstrated that metastatic tumor cells are more than 80% softer than benign mammalian cells.[95] Studies in this field suggest that the biophysical properties of cells can be used as an important intrinsic biomarker to distinguish healthy cells and diseased cells and diagnose disease progression. Malignant cancer cells possess a variety of genetic mutations and it can be inferred that their cytoskeletal structures are also altered. Metastatic cancer cells need to go through a series of processes including intravasation, circulating in the blood stream, extravasation and spreading to neighboring tissues to form secondary tumor.[96] Thus metastatic cancer cells are believed to have altered their biophysical properties to facilitate invasion to distant locations in the body.[97]

Conventional methods for cell biophysical property measurement use mechanical (AFM and micropipette aspiration), optical (optical tweezer), or magnetic (magnetic

twisting cytometry) forces to cause deformation to cells, where such deformations are measured to characterize the biophysical properties of cells.[98-100]

In AFM, the sharp tip at the free end of a cantilever is brought into physical contact with a cell surface and the local deformation is recorded. The applied force is then estimated by calibrating the deflection of the cantilever tip, which is detected by a photodiode using projected laser beam. Using this method, Lekka *et al*. showed cancerous cells (such as T24 and BC3726) had much smaller (as much as 10-folds) Young's modulus than normal cells (such as HU609 and HCV209) using the Sneddon model (cone-shape tip), which suggests cancerous cells were much more deformable than normal cells.[101] Li *et al*. measured the Young's modulus of breast cancer cells versus normal cells using the Hertz model (spherical tip), and found that cancerous MCF-7 showed about 2-fold higher Young's modulus than benign MCF-10A.[102] Also Leporatti *et al*. found that Young's modulus of living HeLa cells and MCF-7 cells were about a half of those when they were fixed using the Sneddon model.[103] These results indicate that the biophysical properties of cells change significantly according to their physiological state, for example malignant cells are more deformable than benign cells.

Micropipette aspiration uses a micropipette (about 1-10 μm in diameter) to provide suction pressure to partially or wholly suck a single cell inside, the shape deformation process is recorded with a video camera for analysis.[104] Byfield *et al*. measured the Young's modulus of bovine aortic endothelial cells (BAECs) using fluorescent images of sucked cells.[105] Zhou *et al*. compared the deformability of individual red blood cells (RBCs) at the different stages of malaria infection and found

that the deformability of RBCs decrease progressively with maturation of the parasite.[106] Kim *et al*. improved the method and used vacuum expanded microfluidic channels as micropipettes and measured the Young's modulus of HeLa cells.[107]

The optical tweezer technique involves projecting a laser beam at a high refractive index dielectric bead attached to the cell. The resulting attractive force between the bead and the laser beam pulls the bead towards the focal point of the laser beam. There are two variations of this technique. One of them involves projecting two laser beams to two beads attached at symmetrical positions across the cell, where the two beads can both be used for stretching the cell. The other variation uses only one laser beam to move one bead, while the other bead is fixed to the plate.[98, 100] Ashkin *et al*. pioneered the use of optical traps to manipulate individual viruses as well as *E. Coli*.[108, 109] Remmerbach *et al*. used two lasers to stretch the cells and measured the deformability of oral epithelial cancer cells compared to oral epithelial cells.[110] Guck *et al*. demonstrated that using the optical tweezer cancerous MCF-7 cells deformed more than noncancerous MCF-10 cells. Deformability of metastatic modMCF-7 cells was significantly higher than that of MCF-7.[111]

Magnetic twisting cytometry that uses beads that are attached to the cells for stretching utilizes similar scheme with the optical tweezer but uses magnetic force on magnetic beads.[112, 113]

In recent years, novel methods that utilize microfluidic technologies have emerged to study cell biophysical properties. Using constriction microchannel smaller than the diameter of cells, Adamo *et al.* and Tsai *et al.* demonstrated that the transit time

of cells passing through the constriction channel can be employed as a measure of cell elasticity.[114, 115] The microfluidic margination approach developed by Hou *et al.* utilized the phenomena that cells flowing in a microchannel tend to have different positions according to their elasticity.[116] This elasticity based separation can also be achieved by separating cancer cells from normal blood cells through inertial flow as demonstrated by Hur *et al.*.[117] Tse *et al.* demonstrated that single cell elasticity can be measured at the throughput close to flow cytometry by quantifying cell deformation optically at conjunction of colloidal flow.[118] Though these microfluidic systems showed improvement over conventional methods in throughput and ease of implementation, they either require expensive optical setup or are incapable to directly quantify the compressibility/elasticity of cells. Furthermore, with fixed constricting channel dimension, it's difficult to isolate the effect of cell size to compared cell elasticity.

Microfluidic acoustophoresis techniques have been widely utilized in applications involving contactless cell and particle manipulation, separation, and concentration.[5, 119] An approach to measure cell compressibility by tracking cell movement in acoustic field has been developed and reported recently,[57, 59] where acoustophoretic force can be calculated from cell trajectories in an acoustic standing wave field and cell compressibility can thereby be determined with given cell size and density. However in this method the cell density has to been estimated to be able to extract the compressibility, which may cause large variations since the density parameter was not from the measured samples. Barnkob *et al*. used the acoustic radiation force model in an arbitrary field (eqn (1.4)) and measured the densities and compressibilities

of particles and cells.[58] Here a similar approach with Barnkob's was adopted to use the acoustic radiation force model in an arbitrary field. The 1-D numerical analysis of the acoustic radiation force was utilized where acoustic pressure amplitude, cell density and compressibility can all be extracted at once from the cell trajectory data.

In previous studies, since cells were evenly distributed in the 3-D space when introduced into the microfluidic systems, there was a lack of control of their vertical position and thus it was difficult to find a focal plane that all cells or particles were in sharp focus. On the other hand, evenly distributed cells also suggests variations in the distance cells travel in acoustic standing wave field, which may bring errors in extracting mechanical properties due to lack of data especially for those with short travelling distance. Also it was found that as cells approached the channel bottom, there was edge effect that was associated with cells' motion, causing errors in measured density and compressibility. In this work a multi-frequency approach combining acoustic levitation was utilized to provide more accurate and robust control of cell position in acoustic trajectory monitoring for mechanical property extraction. Also cells were initially aligned to the second order resonance pressure nodes in the y-direction for added robustness. This method was applied to measure densities and compressibilities of cancer cells with different metastatic potentials.

3.2. Principles for measuring cell biophysical properties using acoustophoretic force

3.2.1. Fundamental laws

In this study the PRF is modeled in an arbitrary acoustic field, which is given by eqn (1.4) and is reprinted as eqn (3.1) for convenience.

$$F_a = -V_0[\frac{1}{2} f_1 \beta_s \nabla < p_1^2 > - \frac{3}{4} f_2 \rho_s \nabla < v_1^2 >] \tag{3.1}$$

where V_0 is the volume of the particle, p_1 is the acoustic pressure amplitude, v_1 is the acoustic velocity amplitude, β_s and ρ_s are the compressibility and density of the solution, f_1 and f_2 are the pre-factors that are determined as follows.

$$f_1 = 1 - \frac{\beta_s}{\beta_0} \tag{3.2}$$

$$f_2 = 2\frac{\rho_0 - \rho_s}{2\rho_0 + \rho_s} \tag{3.3}$$

where β_0 and ρ_0 are the compressibility and density of the particle. The viscous drag force induced by relative motion of the particle to the medium is reprinted as eqn (3.4).

$$F_v = -6\pi\eta a v_r \tag{3.4}$$

where η is the dynamic viscosity of the medium, a is the radius of the particle, and v_r is the relative velocity between the particle and the solution.

Thus the combined axial force exerted on the particle is given by eqn (3.5).

$$F_{tot} = F_a - F_v \tag{3.5}$$

And the Newton's second law of motion is shown in eqn (3.6).

$$F_{tot} = \frac{dp}{dt} = \frac{d(mv_r)}{dt} \tag{3.6}$$

where p is the momentum of the particle, and m is the mass of the particle which is given in eqn (3.7).

$$m = \rho_0 V_0 = \rho_0 (\frac{4\pi a^3}{3}) \tag{3.7}$$

And the velocity v_r can be extracted from the captured video frames. Also the acoustic velocity amplitude v_1 can be deduced from the acoustic pressure field amplitude p_1.[120]

Since the density and compressibility of the medium ρ_s and β_s, cell radius a, medium viscosity η, and cell trajectory are known from the experiment, the three unknown factors are the acoustic pressure p_1, cell density ρ_0, and cell compressibility β_0 that need to be extracted from the model.

3.2.2. Parameter extraction using acoustofluidic modeling

The modeling of acoustic field and extraction of cell biophysical property was performed by our collaborator Zhongzheng Liu in Dr. Yong-Joe Kim's lab. To extract the three unknown parameters, the cost function is defined as the square summation of difference between the simulated trajectories and the experimental trajectories. However, it was found that there exist many local optimization results that give the local minimum points. Thus, the global optimization was obtained by distributing the initial points for the optimization through a certain range of the parameters p_1, ρ_0, and β_0. The custom-built optimization code could then search the defined data range and find the global optimization result. The advantages of this method in extracting cell properties are that

there is no need for estimating the density of cells, and the acoustic pressure can be calibrated with particles of known mechanical properties such as polystyrene beads during the experiment, allowing accurate analysis of the compressibility of cells (Fig. 3.1).[60]

3.3. Lateral pre-alignment in static flow measurement

3.3.1. Conventional static flow measurement

In the conventional method, cells were introduced into the microchannel and acoustic standing wave was applied while the flow was in the static condition, trajectories of cells were recorded and used to calculate the acoustic radiation force exerted on cells, which was therefore used to extract cell contrast factor and even compressibility and density. Typically microparticles were used to calibrate the acoustic pressure field. Therefore the goal of experimental approach for measuring cells' mechanical properties in acoustic standing wave field was to generate a uniform 1-D acoustic field to simplify the analysis of cells' motion. Thus a straight channel with channel width at 375 μm was used to coupe with fundamental resonance frequency of the piezoelectric transducer (PZ26, Ferroperm Piezoceramics A/S, Denmark) at about 2 MHz. Trajectories of cell movement by acoustophoretic force in suspension of a straight microchannel was recorded by a high speed camera (ORCA-Flash4.0 V2, Hamamatsu, Japan), and extracted and analyzed subsequently to calculate cell density and compressibility simultaneously.

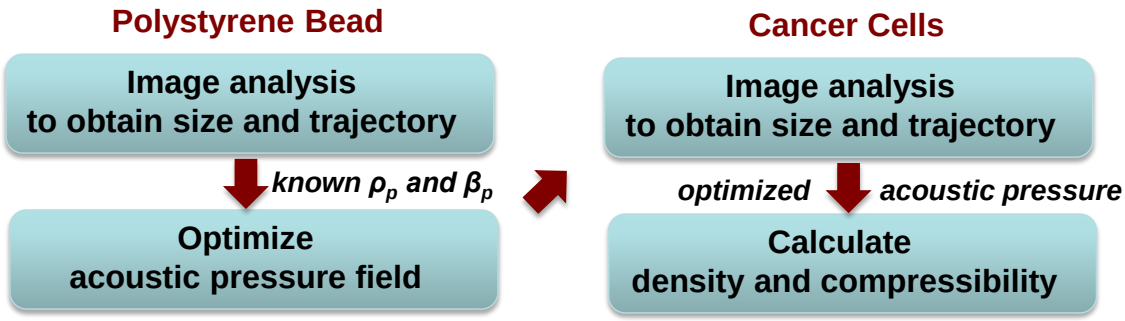

Fig. 3.1 Procedure for parameter extraction using the developed acoustofluidic model.

However as seen in Fig. 3.2, there was inherent shortcoming of the conventional measurement approach. The particles (polystyrene beads, Diameter: 11 μm, used for illustration) were distributed in the 3-D space in the fluid, making it difficult to focus on all particles at a time. Also these particles would gradually settle to the channel bottom due to gravity. On the other hand, since particles were also scattered in Y-direction, there was large difference in the initial positions while providing acoustic standing wave. This would cause variations in data extraction from cell trajectories and hence extracted properties.

Another issue with this method is that for particles that are close to channel bottoms, there's increased friction from the device, making inaccurate analysis of particle trajectory. Also, it was found that another influence from the device is that as particles get closer to channel walls there's a "wall factor" added to the viscous drag force, further increasing the inaccuracy of this method.[121-123]

Since all these factors were not taken into consideration of the conventional static flow measurement method, it raises the need for a method with well controlled particle position and trajectory.

3.3.2. Methods

Using a single band acoustic standing wave to drive particles or cells for trajectory monitoring had the shortcoming of initial position control, thus a method utilizing multi-frequency acoustic radiation force was developed. As shown in Fig. 3.3A, particles or cells were initially randomly distributed in the lateral direction, by driving at second

order resonance frequency in Y-direction particles were pre-aligned to the pressure nodes of second order resonance frequency. Thereby uniform trajectories can be achieved while particles were driven to the pressure node in channel center at the first order resonance frequency in the y-direction for recording. In this case, all particles or cells initially had the same fixed position, and all had the same travelling distance to reach to the channel center, greatly improving measurement accuracy and robustness.

3.3.3. Microchip fabrication

To fabricate the microchip, bare silicon wafer was deposited with aluminum at a thickness of about 500 nm. The microchannel was patterned with positive photoresist S1818 (Shipley). The photoresist was spin coated at 4000 rpm for 30 sec, pre-baked at 110 ℃ for 5 min, exposed at 100 mJ/cm^2 dosage, developed with MF-319 developer, and hard baked at 120 ℃ for 10 min. The aluminum was then etched using photoresist as etching mask, then the photoresist was removed by acetone. The microchannel was then etched in silicon by using reactive-ion etching (Oxford Plasmalab 100 ICP RIE) to a depth of 100 μm. A borofloat coverglass that had fluidic access holes drilled using a bench drill press (DP101, Ryobi Ltd, SC), was then bonded to silicon wafer using anodic bonding. The RIE process was tested and optimized to achieve straight side channel without forming silicon grass at the channel bottom. The optimized condition is listed in Table B.1. The fabricated microchannel had a width of 375 μm to generate 1st order resonance frequency close to the fundamental frequency of 2 MHz of the piezoelectric ceramic (PZ26, Ferroperm Piezoceramics A/S, Denmark). Fluidic connection was

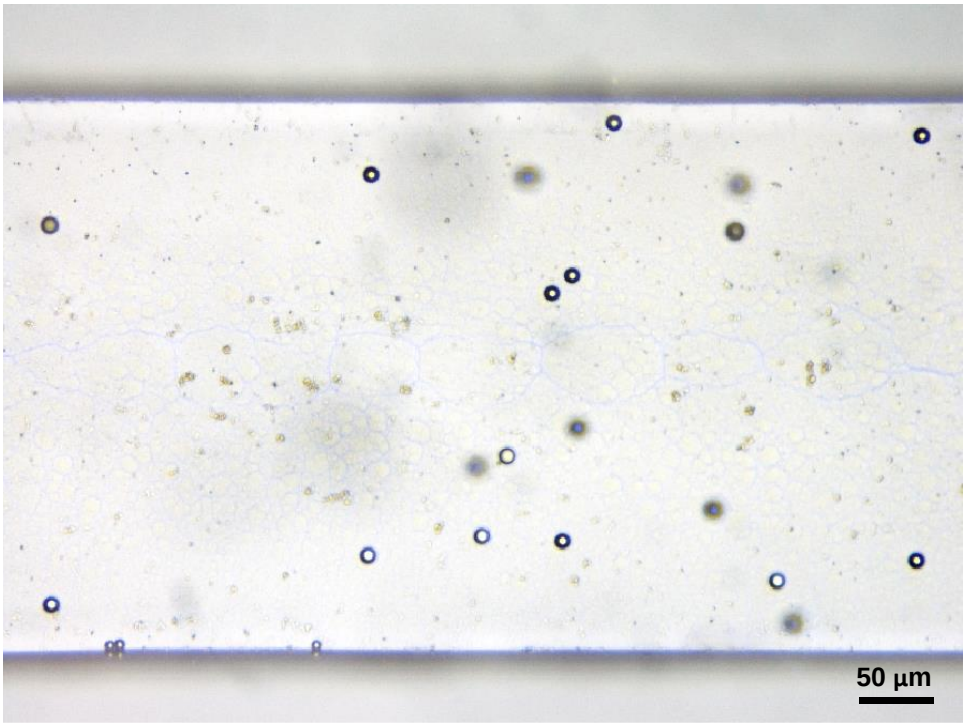

Fig. 3.2 Microscopic image showing the microchannel with polystyrene beads. The beads (Diameter: 10 µm) were distributed randomly prior to applying 1-D acoustic standing wave. Scale bar = 50 µm.

provided by flat-bottom ferrules (P-200N, Upchurch Scientific, WA) with Tygon® tubing (Saint-Gobain Performance Plastics, OH). Piezoelectric transducers (PZ26, Ferroperm Piezoceramics A/S, Denmark) were attached to the bottom of the microchip at desired positions by using wax (Crystalbond^{TM} 509, SPI Supplies/Structure Probe Inc., PA).

3.3.4. Results

Fig. 3.3B shows time-lapse images of particle movement with and without pre-alignment to the pressure nodes of second order resonance frequency, while Fig. 3.3C showed the recorded trajectories of particles moving to the pressure node of first order resonance frequency in the channel center in both cases. It can be clearly seen that the trajectories of particles with pre-alignment are much more uniform and have smaller variation than the trajectories of particles without.

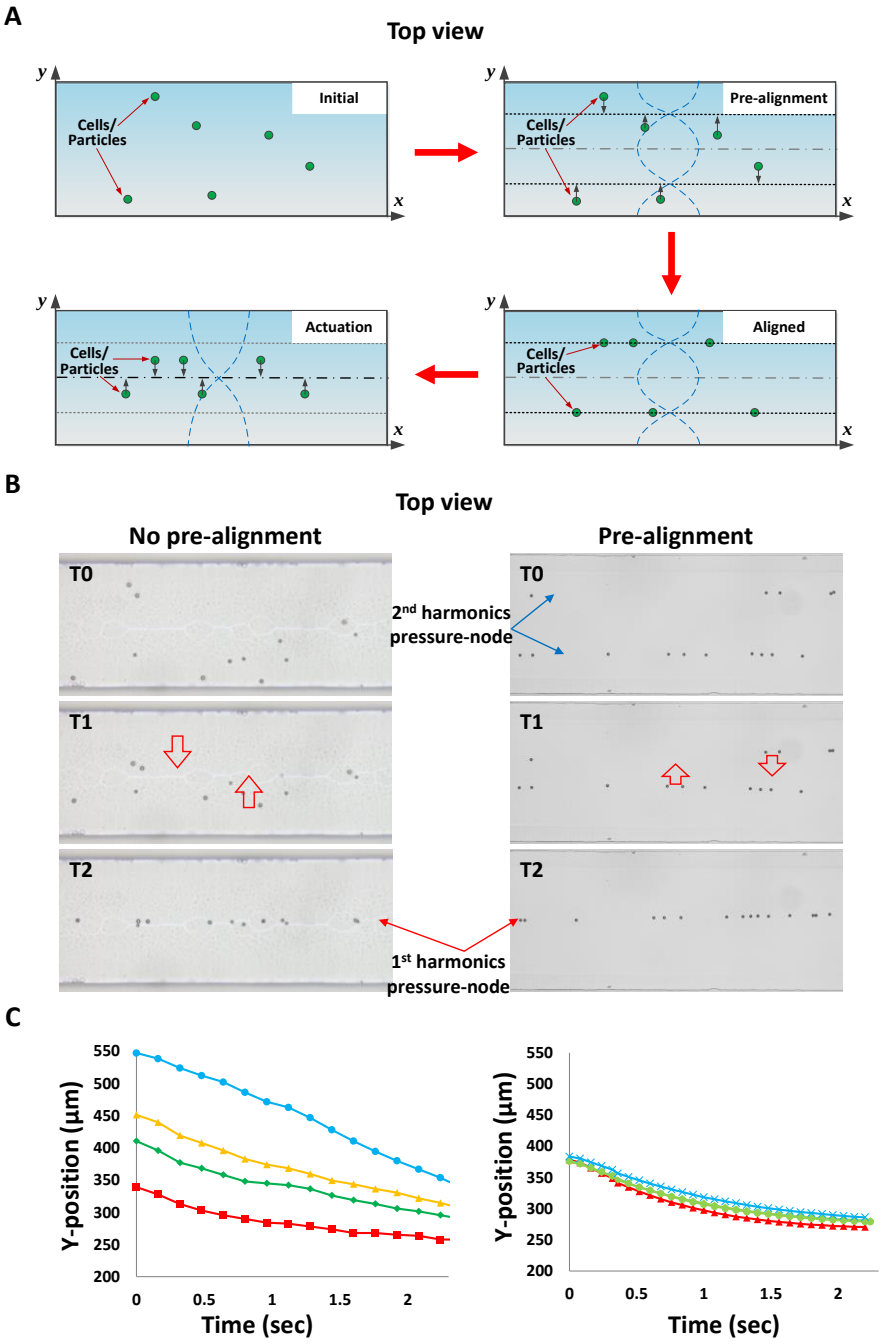

Fig. 3.3 Effect of particle pre-alignment to the second harmonic pressure nodes on particle trajectory analysis. (A) Top-view illustration of cell/particle movement in the lateral direction using a pre-alignment step to the 2nd harmonic pressure nodes before focusing the cells/particles to the 1st harmonic pressure node for acoustophoretic trajectory analysis. The piezoelectric transducer is attached at the bottom of the device. (B) Comparison of polystyrene bead movement with and without a pre-alignment step. (C) Comparison of polystyrene bead trajectories from (B).

3.4. Acoustic levitation in static flow measurement

3.4.1. Methods

Even with pre-alignment at the second order resonance frequency in the y-direction, the vertical positions of particles or cells were still dispersed, making it difficult to track due to lack of focus. Also to avoid the wall effect and friction from channel bottom, particles were levitated using acoustophoretic force in the microfluidic channel in Z-direction. Acoustic levitation was achieved in the microfluidic channel using a thick APC841 transducer (Diameter: 19 mm, Thickness: 12 mm, APC841, APC International, Ltd.) since the acoustic energy that it could generate is proportional to the volume of the transducer.[120] Due to the relatively large size of the transducer, within the field of view for particle and cell trajectory tracking the acoustic field could be regarded as uniform.

The principle of this levitation method is shown in Fig. 3.4A. The piezoelectric transducer was actuated at the first order resonance frequency in Z-direction, and particles were lifted to the pressure node which was at the channel center in Z-direction. To evaluate the capability of acoustic levitation we used fluorescent polystyrene beads to measure the height that these beads were lifted using the applied acoustic signal. The result is shown in Fig. 3.4B (top view), where once the first order resonance frequency was applied in Y-direction the beads were aligned in the channel center in Y-direction, and once the first order resonance frequency was applied in Z-direction the beads were lifted up by 47 μm measured by the Zeiss microscope (Observer Z1, Carl Zeiss), which was close to the channel center in Z-direction.

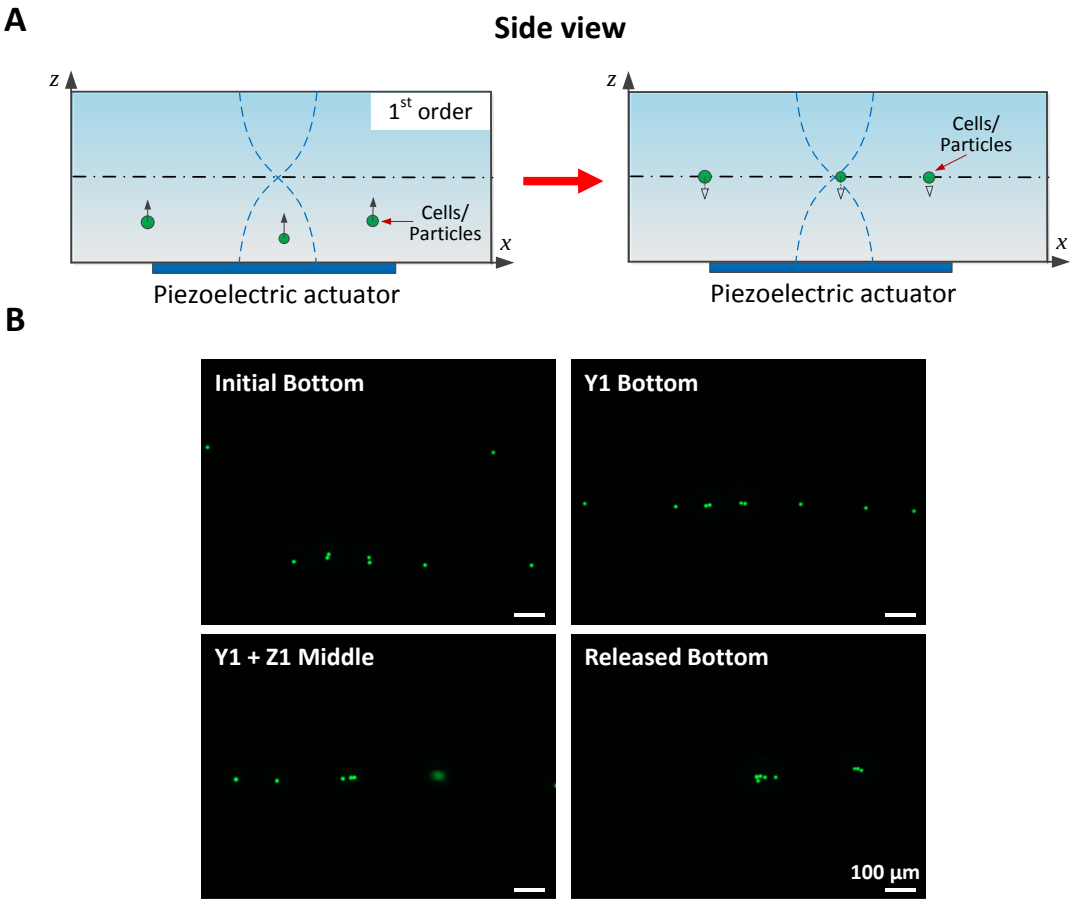

Fig. 3.4 Acoustic levitation. (A) Schematic showing the principle of acoustic levitation. Acoustic standing wave at the fundamental resonance frequency in Z-direction was applied, and particles or cells were lifted to the channel center in Z-direction. (B) Microscopic images showing fluorescent polystyrene beads (Diameter: 10 µm) positioning using acoustic levitation. Scale bar = 100 µm.

Also it was found that with the signal used in this experiment, it took less than 1 sec for polystyrene beads to be lifted up to final position, while it took about 1-2 sec for mammalian cells to be lifted up to final position. Thus as the cells or particles introduced into the channel entered the field of view which was located in the center of the transducer, they already reached the final positions under the flow conditions used.

3.4.2. Results

Fig. 3.5A shows the images of particles with and without being levitated to the channel center in Z-direction by acoustophoretic force. It can be seen that without levitation some particles are suspended in buffer, while some particles are close to channel bottom. This difference in initial Z-position caused large variation in particle trajectories moving to channel center in Y-direction at first order resonance frequency for recording. From Fig. 3.5B it can be clearly seen that there's a significant improvement in particle trajectory uniformity by levitating particles using acoustophoretic force.

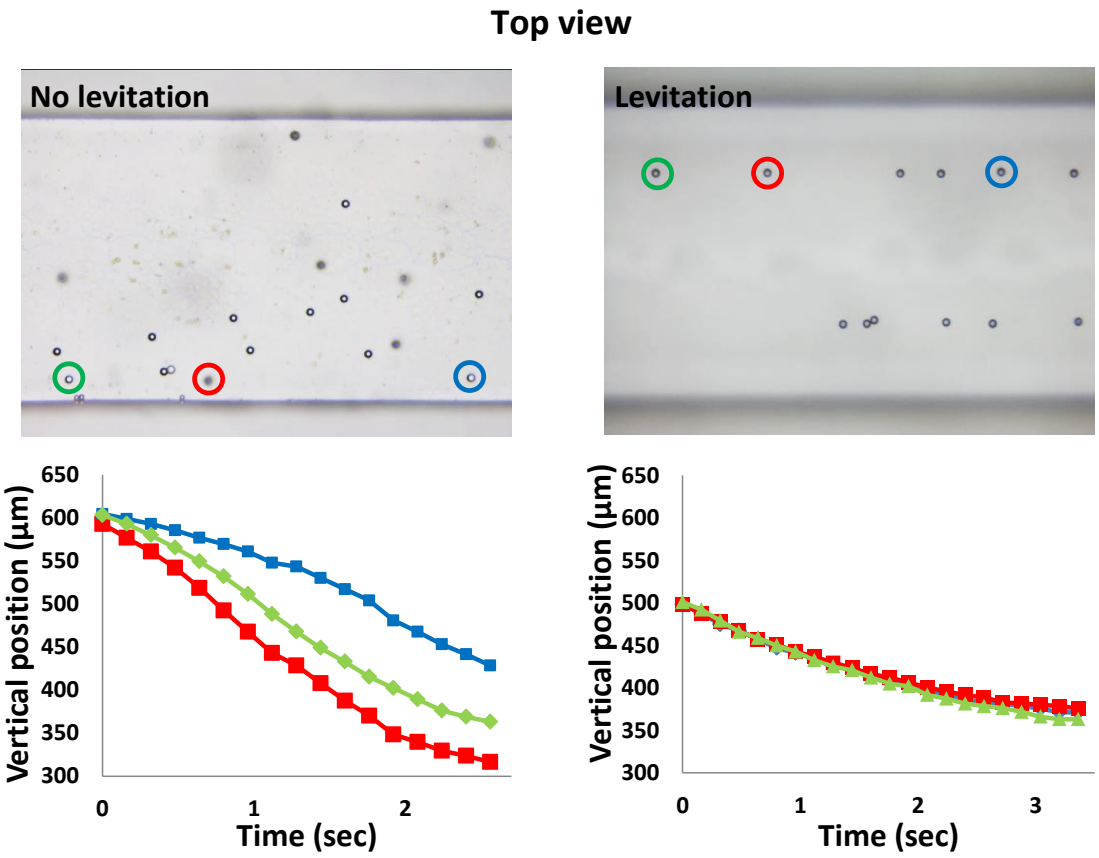

Fig. 3.5 Z-direction acoustic levitation effect on particle trajectory monitoring in Y-direction. (A) Comparison of the initial polystyrene bead distribution viewed from top. Without levitation, some particles are in focus and some particles are out of focus (left). With levitation, all particles are lifted to the same height and are in focus (right). (C) Comparison of polystyrene bead trajectories from similar Y-coordinates. It can be clearly seen that with acoustic levitation particle trajectories are more uniform.

3.5. Cell property measurement using static multi-frequency acoustics

3.5.1. Methods

From previous study it can be clearly seen that there's significant improve in particle trajectory uniformity by performing pre-alignment in Y-direction and levitation in Z-direction. Therefore it is desirable to combine the pre-alignment in planar directions with the acoustic levitation in the vertical direction to enable precise and robust control of particle or cell position in 3-D space for mechanical property measurement using acoustic standing wave. To generate the required signals, a custom-built signal adder PCB board using an Op Amp (AD811, Analog Devices) to combine multiple frequencies and apply them simultaneously to the transducer was used. The schematic diagram of the circuit is shown in Fig. 3.6A. Since a current-feedback Op Amp (AD811) was used and thus a resistor was attached to the output to generate voltage signals. Also the capacitors added to the output as well as the power supplies were capable to filter out high frequency noise.

The performance of the signal adder was first evaluated using continuous flow particles manipulation with simultaneous actuation of first and second order resonance frequencies in Y-direction (Fig. 3.6B). It can be seen that by tuning the amplitude of the two different resonance frequencies, the particles' (polystyrene beads, Diameter: 10 μm) position moved continuously.

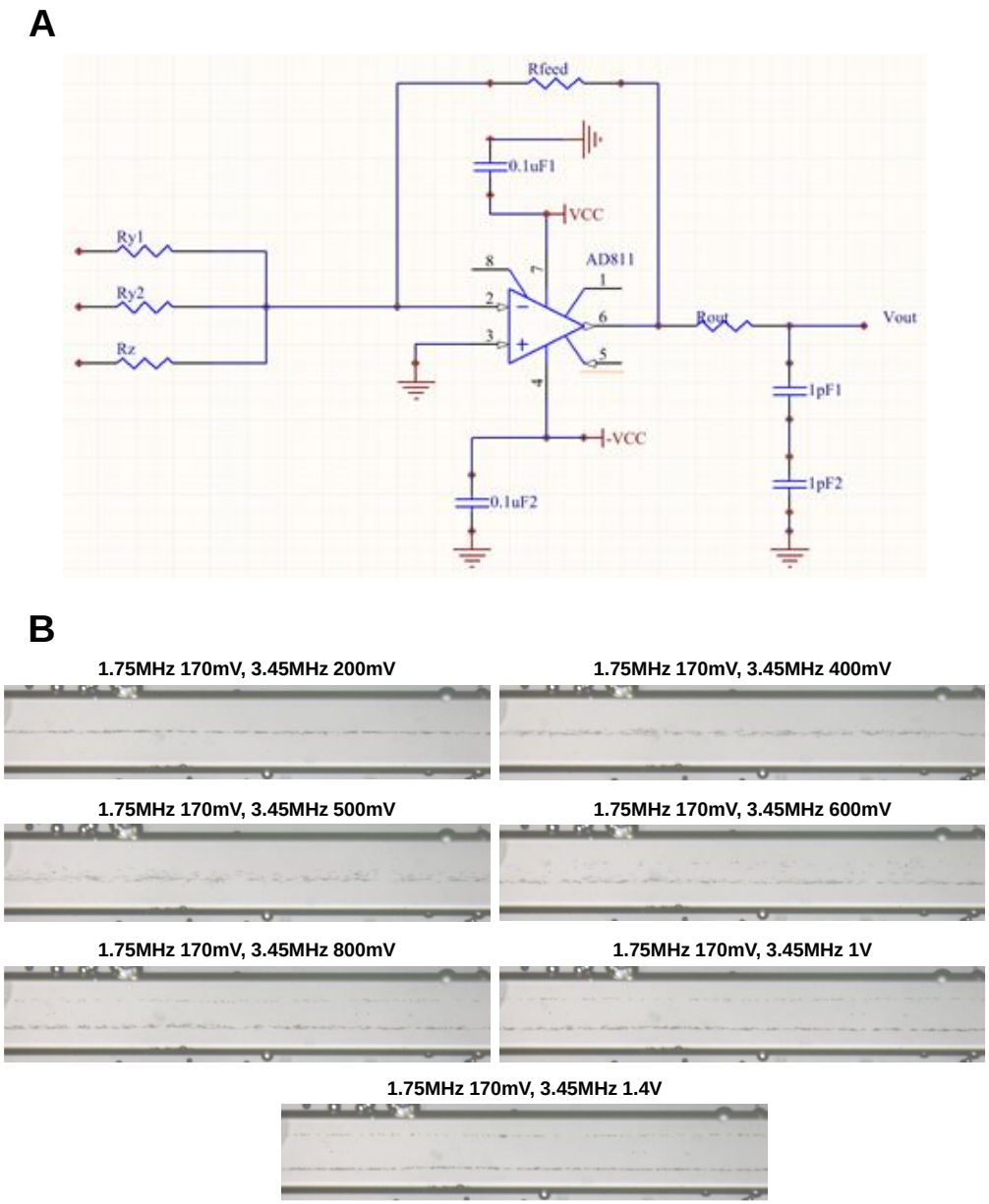

Fig. 3.6 Signal adder for multi-frequency acoustofluidics. (A) Schematic of the signal adder circuit. (B) Images showing positions of focused polystyrene bead bands in continuous flow by tuning the amplitudes of the first and second order resonance frequencies.

3.5.2. Experimental

Cell mechanical property measurement was performed using the multi-frequency technique that combined acoustic levitation in the static scheme, so that to provide more accurate and robust control of cell position, and to ensure cells were suspended in the medium to avoid any variations for edge effects near the channel bottom.

The experimental setup was similar to that used in oil droplet experiment, with modifications that multiple function generators were used to apply sinusoidal signals to the signal adder PCB board, and the combined signal was applied to the APC841 transducer via a 50 dB power amplifier (2100L, Electronics & Innovation, Ltd.).

The microchips were fabricated using DRIE etching on silicon wafers with aluminum etching mask as described earlier. Using the silicon microchannel (Length: 25 mm, Width: 370 μm, Height: 100 μm), it was found that the first and second order resonance frequencies in Y-direction were 1.92 MHz and 3.66 MHz, respectively, while the first order resonance frequency in Z-direction was 4.75 MHz.

The experiment used polystyrene beads (Diameter: 10 μm, Polybead® Microspheres, Polysciences) to calibrate the acoustic pressure field since the mechanical properties (density and compressibility) for polystyrene is known, and then cells were introduced for trajectory monitoring. In the second step the acoustic pressure field measured with polystyrene beads was used so that only cell density and compressibility were unknown factors and can be extracted. The detailed experiment procedure goes as follows.

1. Quickly flush with particles without any acoustic signal;

2. Introduce particles at 100-200 μl/hr using a syringe pump, in this step second order resonance frequency in the y-direction as well as the first order resonance frequency in the z-direction was applied;

3. Stop the pump, clamp both inlets and outlets, start video recording, turn off z-direction signal, and switch to first order resonance frequency in the y-direction;

4. Stop video recording, stop acoustic signal.

An automatic control program in LabVIEW^{TM} (National Instruments) with the same logic was developed to control the function generators and syringe pump that was used to introduce samples. Also a set of solenoid valves were used to open/close the fluidic inlet/outlet valves.

3.5.3. Results and discussion

Fig. 3.7 shows the trajectories of different head and neck cancer cells (Tu686, 686LN, M4e, 37B) and polystyrene beads. All cells and beads were imposed to acoustic levitation and pre-alignment prior to driven to the channel center in Y-direction. It can be seen that by simply comparing the trajectories it's difficult to differentiate different cells.

Fig. 3.8 shows the extracted densities and compressibilities of Tu686, 686LN, M4e, 37B, respectively. The results conform with previous head and neck cancer cell invasion capability study.[97]

With improved control of cell position in the cell trajectory extraction, the advantage of the developed method over conventional method lies in two aspects: first

there are more usable trajectories in each recorded video since all cells are focused, second in each trajectory the data interpolation is easier and more repeatable since the travelling distance is almost the same. Also since the cells are levitated they remain suspended during trajectory recording, while in the conventional method the cells might be close to channel bottom due to gravity which might bring more variations.

3.6. Continuous flow acoustic cell property measurement

3.6.1. Methods

The multi-frequency static flow cell trajectory analysis method provides improved accuracy and repeatability in measuring cell density and compressibility, however still has low throughput which greatly hinders its usage. Also in the static flow case, cells/particles travel a short distance, which poses limitation in the resolution. Therefore continuous flow trajectory monitoring was performed to achieve improved throughput and resolution. Cells or particles were introduced from the side channel with flow focusing while the center inlet was used for buffer medium. Thus as acoustic standing wave was generated, cells or particles would be moved towards the center of the microchannel. Depending on the mechanical properties of cells and particles the amplitude of acoustic radiation force they experienced would be different, and therefore cells or particles can be separated with flow. Here a single first order resonance frequency in Y-direction was used and cells or particles were introduced and deflected continuous. The trajectories of cells or particles can be recorded and analyzed for comparison or used to extract their density and compressibility.

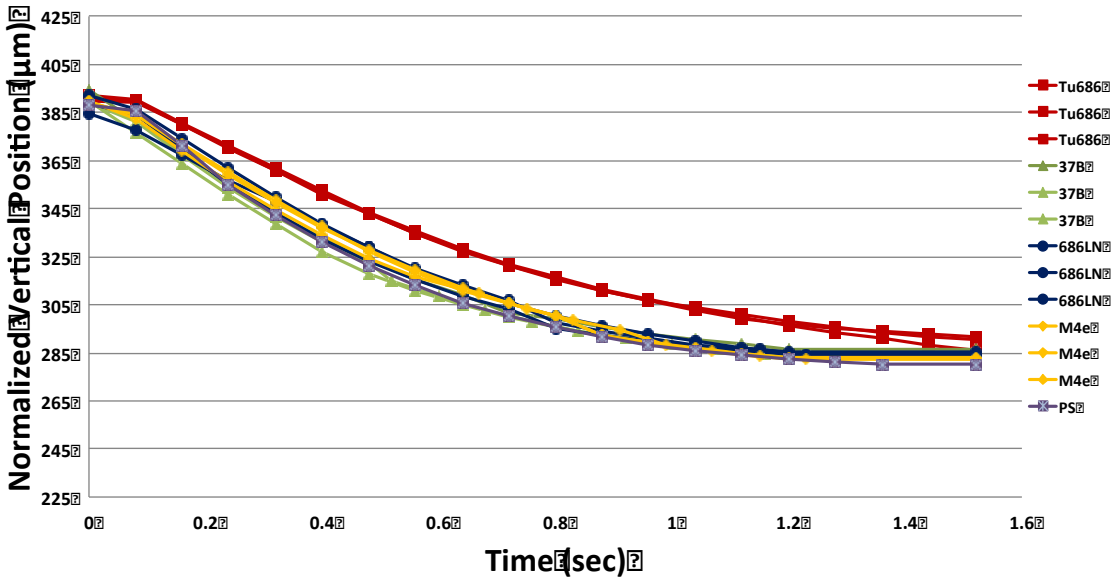

Fig. 3.7 Trajectories of four types of head and neck cancer cells using acoustophoretic force with three dimensional pre-alignment. However, from the trajectory itself cancer cells phenotyping cannot be done. This may partly due to the lack of cell size information, and requires numerical modeling to extract cell density and compressibility from trajectories.

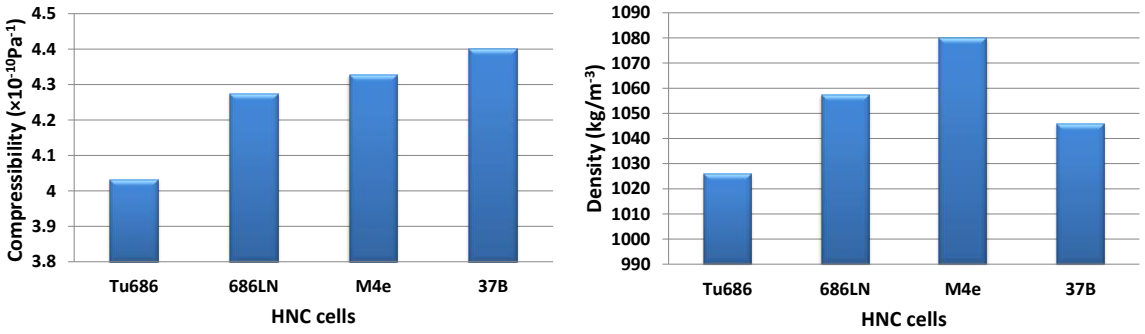

Fig. 3.8 Extracted density and compressibility for head and neck cancer cells. The compressibility data conforms well with their metastatic potential as reported previously by other researchers.

Since the acoustophoretic force is proportional to cell size and contrast factor, it is necessary to differentiate the size parameter from recorded trajectories. Therefore a scatter plot with cell size as X-axis and exit position as Y-axis was deployed for clear comparison of cell density and compressibility (as shown in the contrast factor) difference.

3.6.2. Design and fabrication

The continuous flow acoustic cell property measurement device features a straight main channel, with flow focused side channels as cell inlet. The main channel was designed to be 375 μm in width, while the side channel was 30 μm in width (Fig. 3.10).

Continuous flow microchips were fabricated in silicon, following the steps as previously described. A transducer (PZ26, Length: 25 mm, Width: 15 mm, Thickness: 1 mm, Ferroperm) was attached to the bottom of silicon chip to generate planar acoustic standing wave. The flow rates in each stream was set as center main inlet 150 μl/min, center side inlet 12.5 μl/min, and carrier side inlet 25 μl/min.

3.6.3. Results

Fig. 3.11 shows the trajectories of polystyrene beads (Diameter: 11 μm) while they enter the acoustic standing wave field with and without flow focusing in the side channel. It can be clearly seen that flow focusing helped to maintain the position and entry point of polystyrene beads into acoustic field.

Fig. 3.12A shows a series of time-lapse images of particle movement with and without acoustic deflection. Fig. 3.12B shows an example of analyzed trajectories using polystyrene beads with different diameters (6 and 11 μm). Thus with different parameters (size, density, compressibility) the difference of amplitude of PRF can be reflected on the trajectories in this continuous flow scheme, which can be therefore used as the marker of cells' mechanical properties.

Since the deflection distance in Y-direction is proportional to the total driving force (acoustophoretic force deduce viscous drag force), and the acoustophoretic force is proportional to cell size and contrast factor, plotting cell size *vs*. deflection distance (exit position) can give the information about cell contrast factor difference. Fig. 3.13 shows the scatter plot of breast cancer cells and breast cell MCF-10A as well as polystyrene beads (Diameter: 10 μm) in continuous flow acoustic standing wave. It can be seen that except MCF-7 having a large variation, other cells and polystyrene beads could be well distinguished from the plot. This confirms the analysis method as well as the continuous flow measurement can be a viable way to evaluate cell mechanical property.

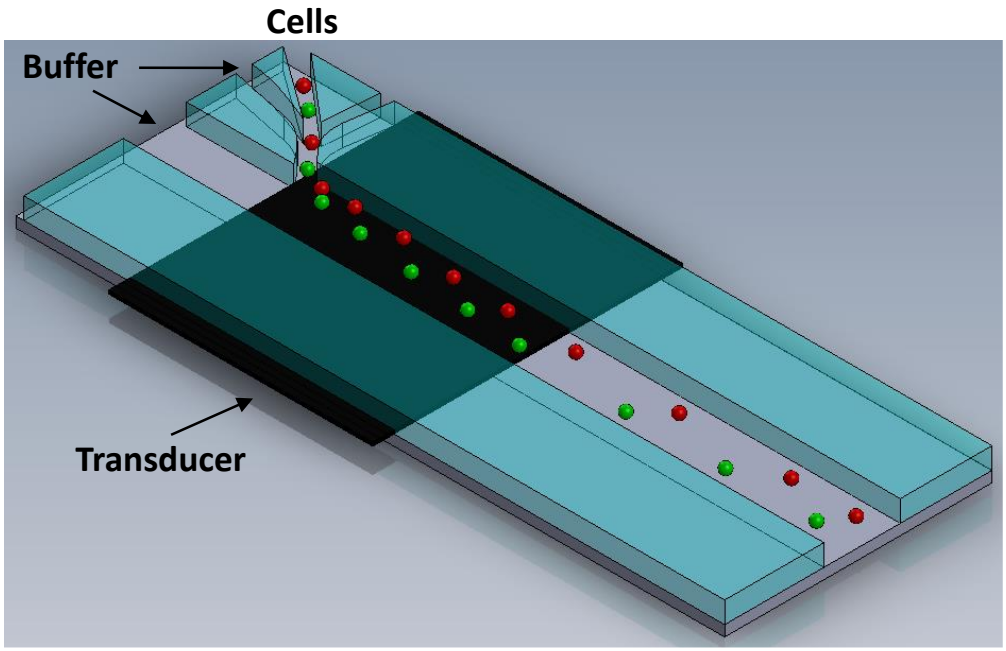

Fig. 3.9 Design of continuous flow cell biophysical property measurement device.

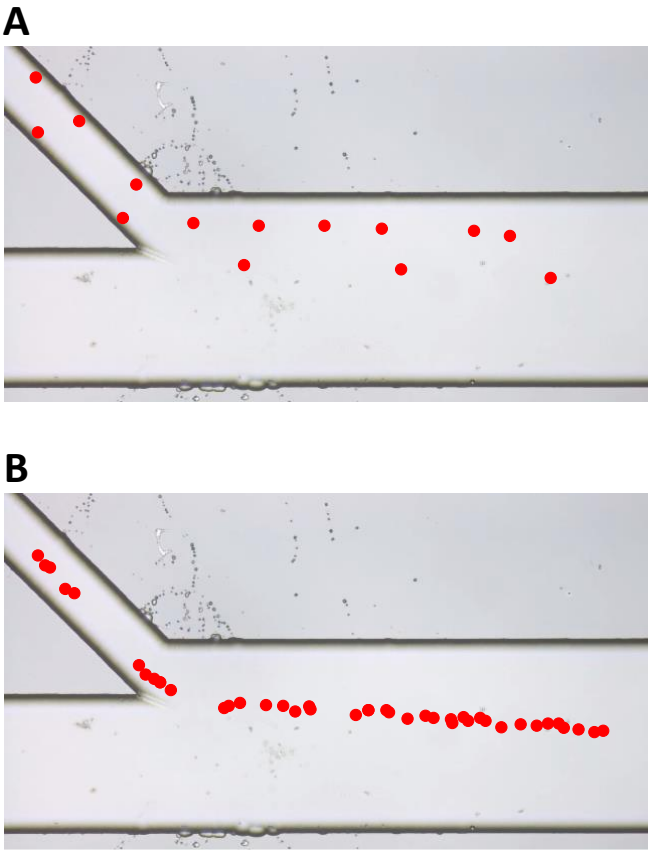

Fig. 3.10 Trajectories of polystyrene beads moving through acoustic standing wave field without (A) and with (B) flow focusing.

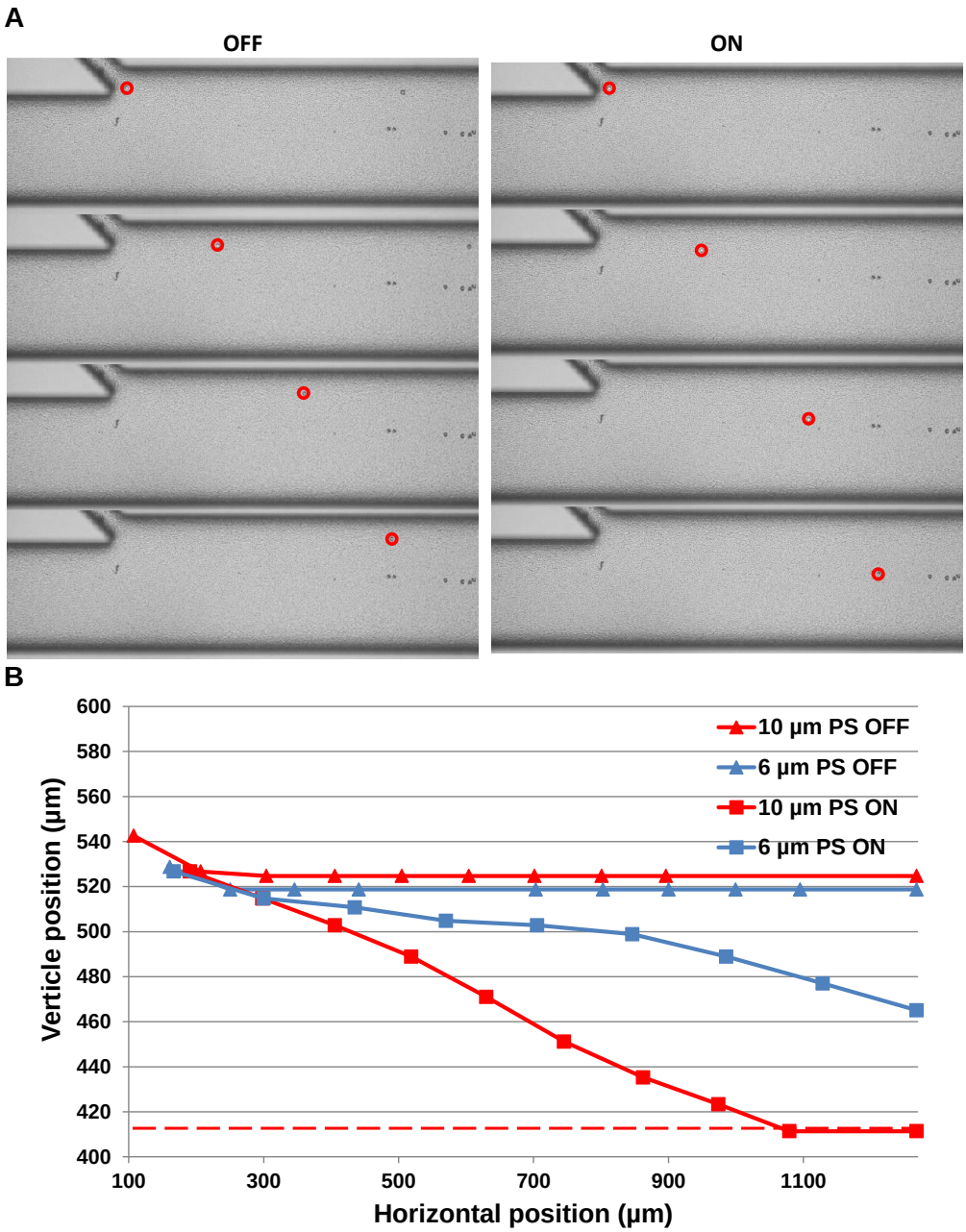

Fig. 3.11 Trajectories of beads in continuous flow system. (A) Time-lapse microscopic images showing movement of polystyrene beads with and without acoustic standing wave. (B) Analyzed trajectories of polystyrene beads of 6 and 10 μm diameters in continuous flow under acoustic standing wave.

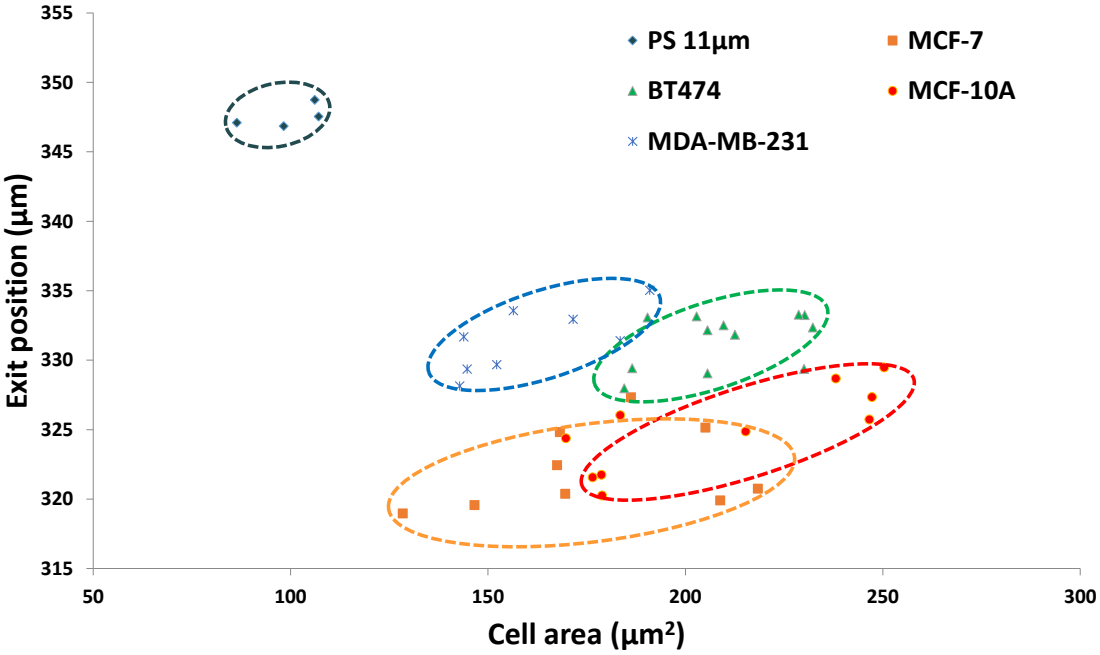

Fig. 3.12 Scatter plot of breast cancer cells and normal breast cell MCF-10A as well as polystyrene beads in continuous flow acoustic cell property measurement.

3.7. Discussions

In this study the acoustic radiation force was utilized to analyze the deformability of cells and particles and extract their mechanical properties by monitoring their motion in acoustic standing wave field with and without flow. The implementation of the multi-frequency technique in combination of acoustic levitation provided improved control of the locations of cells or particles using the trajectory tracking, which helped to reduce the variations in extracting the mechanical properties. Continuous flow scheme provides much higher throughput without compromising single cell resolution in differentiating cells with different metastatic potential.

CHAPTER IV

MICROFLUIDIC ACOUSTOFLUIDICS WITH INTEGRATED IMPEDANCE DETECTION

4.1. Introduction

In acoustofluidic trajectory analysis for cell mechanical property analysis, the throughput is very low in static flow case since each time the flow needs to be blocked to perform acoustic focusing and recording. Continuous flow trajectory tracking improves this issue since cells can be introduced and trajectories be recorded continuously. However both methods rely on the use of expensive high speed camera and large data processing capability. Also the trajectory analysis is not in real time in both methods, which poses difficulty for these methods to be used in applications that require real time analysis. To improve the throughput and facilitate real time detection and measurement, fluorescent labeling can be used, which requires added procedure and cost.

Impedance-based particle/cell detection has been widely used as a powerful and versatile non-invasive detection method, especially in impedance-based flow cytometry. This method solely relies on the dielectric property of particles/cells and provides real time information about the existence and size of particles/cells. Also by tuning the frequency and using multiple frequencies information on particle/cell internal composition such as membrane capacitance and cytoplasmic vesicle constitutes can be obtained through high content screening. Therefore, impedance-based cell detection can

be used as a high throughput and real time measurement approach in continuous flow acoustophoretic cell trajectory analysis.

It's required to extract two parameters in continuous flow cell detection for the cell phenotyping using acoustophoretic force, the cell size and cell position. Since the electrodes for impedance-based detection have fixed X position (along the flow direction), only the Y position is needed (perpendicular to flow direction) to be measured.

Cell size can be quantified using a pair of single-ended parallel electrodes to measure the change of amplitude and phase. Though differential measurement using two pairs of parallel electrodes can achieve improved sensitivity, this configuration requires two-channel measurement with increased complexity. Therefore in this study we adopted single-ended electrode configuration for cell size measurement.

To measure cell position, a straightforward approach is to use an array of parallel electrodes and record the cell passing through either of them. However this approach requires abundant electrodes and multi-channel impedance analyzer, making the fabrication and data acquisition and analysis difficult. Therefore a novel electrode design using a pair of tilted electrodes was developed and proposed in this study. Due to asymmetry of the electrodes in the lateral direction cells passing from different positions of the electrodes would trigger different level of detected signals and can be thus differentiated. This configuration offers simple and easy detection of particle/cell position (Y position) in the microchannel in a continuous flow device, and can easily achieve high throughput.

4.2. Principles of impedance-based size and position detection

The principles for impedance-based continuous flow particle/cell size and position detection are illustrated in Fig. 4.1. As shown in Fig. 4.1(A), a pair of tilted electrodes enables the detection and quantification of particles/cells Y position detection. Here cells 1, 2 and 3 indicate cells of the same size passing through the tilted electrodes at different Y positions, assuming the other dielectric properties are the same. The fundamental for single-ended impedance-based detection is that a certain voltage is applied to the electrodes, and the current that passes through the electrolyte medium and particles/cells is detected and converted to impedance value. Since the spacing of tilted electrodes change at different Y positions, the electric field and thus measured impedance would change according to its Y position for the same particle/cell. Therefore here cells 1, 2, and 3 would cause different amplitudes of detected impedance, and the transit time would also be different and can be used to differentiate the cells. However, even the same type of cells varies a lot in their sizes, thus from the detected impedance at tilted electrodes itself it is difficult to interpret the corresponding Y position, since a cell of different size can very well cause the change in amplitude and phase as well. Therefore calibration of the position detection signal according to their size is necessary.

Fig. 4.1(B) shows that a pair of parallel single-ended planar electrodes is utilized to detect the size of passing particles/cells. In the parallel configuration, the electric field is very uniform and therefore for the same cell the detected signal changes insignificantly. Thus the change of measured impedance (amplitude, phase) of the parallel electrodes can be regarded solely from the variation of cell size and dielectric

properties. Since for the same cell type the dielectric properties can be regarded as uniform, the detected signal of parallel electrodes can be directly correlated to cell size variation. As shown in Fig. 4.1(B), cells 1, 2, and 3 indicate cells of different size passaging through the parallel electrodes. The detected impedance (amplitude, phase) changes according to cell size (larger cell causes larger impedance change).

This method utilizes two pairs of electrodes and an impedance analyzer, and can eliminate the need for expensive high speed camera which can cost tens of thousand dollars, which facilitates high throughput and low cost detection of particle/cell size and position inside a microchannel, especially in applications such as monitoring particle/cell trajectory in acoustofluidic systems.

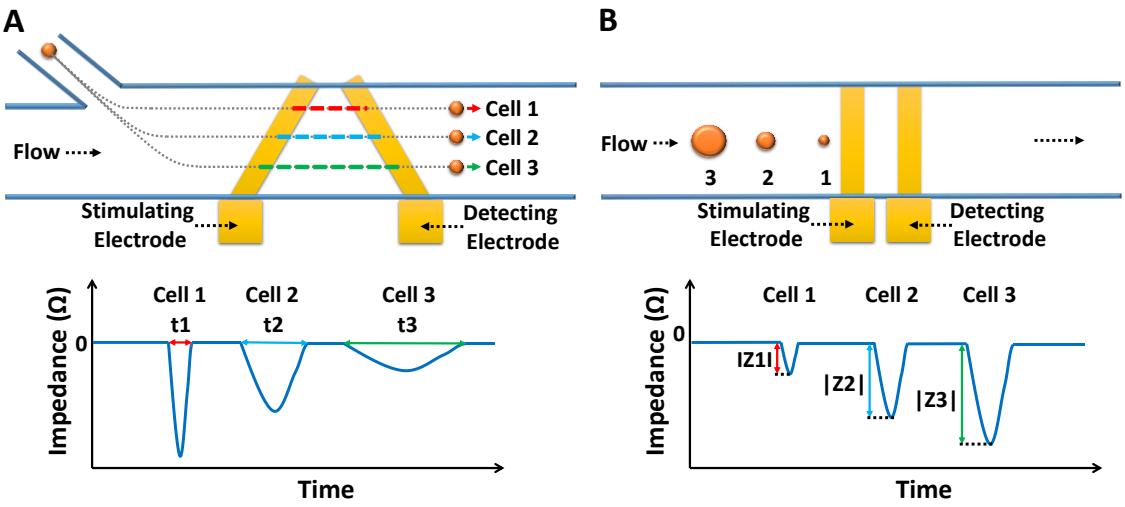

Fig. 4.1 Principles of impedance-based particle/cell position (A) and size (B) detection. (A) Impedance-based position detection using tilted electrodes. (B) Impedance-based size detection using parallel electrodes.

4.3. Design and fabrication

4.3.1. Design

The method for size and position detection was first characterized using a straight channel device and the electrode design was optimized. Narrow electrode design would help to improve signal to noise ratio for a given size of particle/cell to be detected. However, due to difficulty in fabrication, electrodes with less than 10 μm width were not used since most of them came out bad. Therefore in this study the electrode width was fixed to 15 μm. Also the electrodes were stretched wide after the detection region to reduce the impedance value of the detection electrodes themselves to get larger current output at a certain applied voltage. For parallel electrodes, the gap between electrodes was also fixed to 15 μm for the ease of fabrication. While for tilted electrodes, electrodes with different tilting angles were characterized and optimized. The three different designs for tilted electrodes are shown in Fig. 4.2. The gap d1 at the top was fixed to 10 μm, while the gap at the middle d2 changed from 40 μm to 60 μm to 100 μm from left to right.

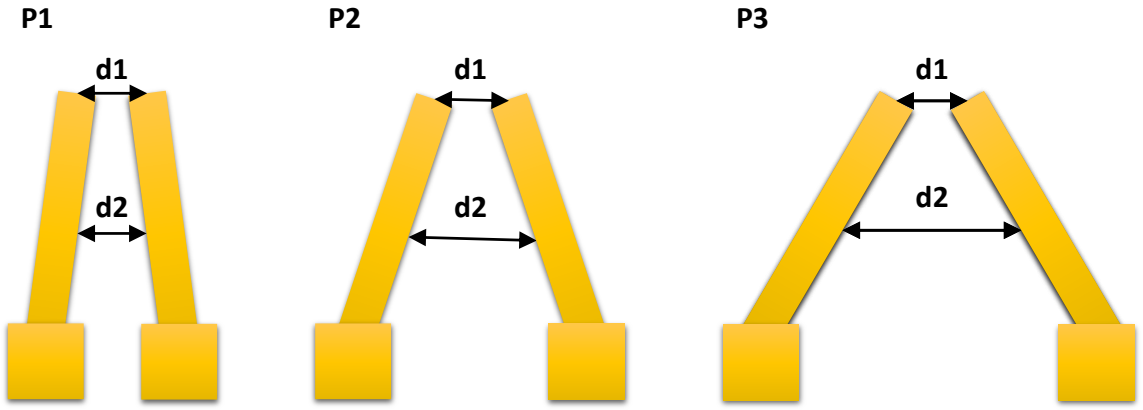

Fig. 4.2 Designs of position detection electrodes with different tilting angles. In all three designs, d1 = 10 μm, while d2 changes from 40 μm to 60 μm to 100 μm from left to right.

A straight microchannel (channel width = 187.5 μm) with three-inlet flow focusing microchip was used to conduit the flow and introduce particles/cells. The particles/cells are delivered through the middle narrow channel (channel width = 25 μm). The three-inlet design can deliver particles/cells to any position inside the microchannel by varying the flow rates of each inlet, providing a simple and versatile characterization model.

With optimized electrode design, impedance-based detection was integrated with continuous flow acoustofluidics system for analysis of cell mechanical properties such as density and compressibility. The proposed system is shown in Fig. 4.3. This method allows high throughput (target throughput 100-1000 cells/min) and low cost phenotyping and cancer cells.

4.3.2. Microchip fabrication

The electrodes for impedance-based detection were fabricated on glass slides. Chrome/Au (50 nm/200 nm) was deposited, and patterned with photoresist (MICROPOST® S1818, Shipley, MA). An isolation layer of 100 nm silicon dioxide was deposited by PECVD (PlasmaLab 80plus® PECVD, Oxford, UK) prior to use. For characterization, the three-inlet microchannel was fabricated in poly(dimethylsiloxane) (PDMS, Sylgard® 184, Dow Corning, MI) using the soft lithography technique. The master molds for the microfluidic devices were fabricated with a standard photolithography process using SU-8™ (MicroChem, MA). The microchannel was fabricated to a channel height of 24 μm. PDMS was then poured onto the master molds

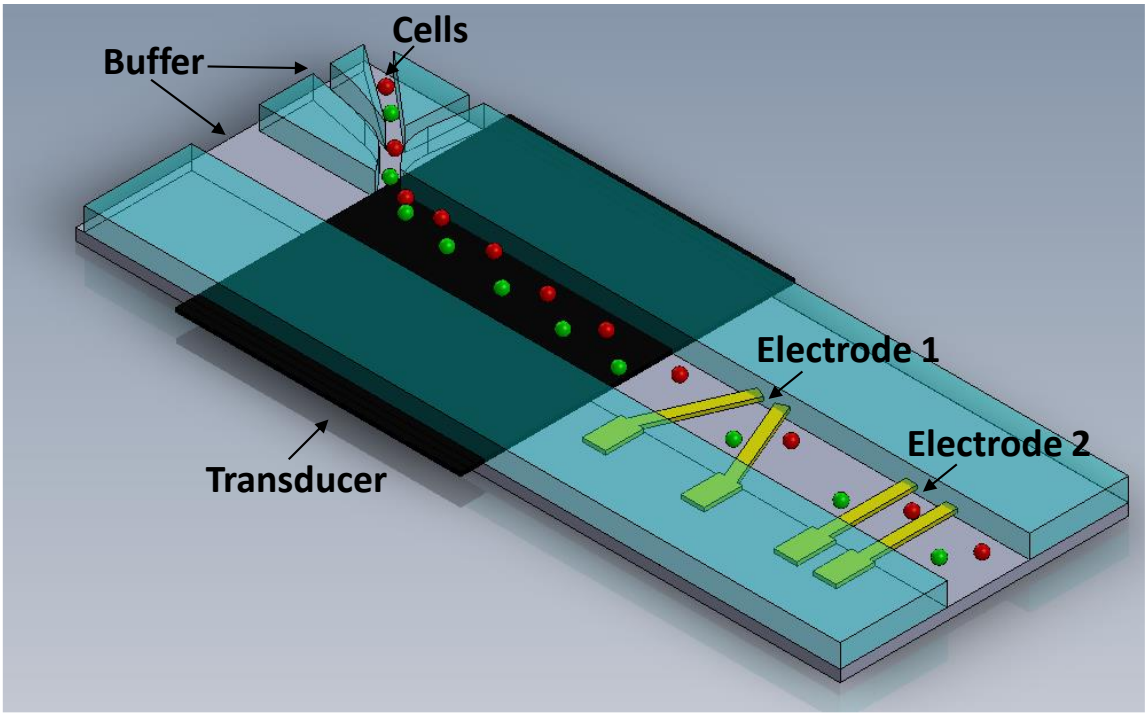

Fig. 4.3 Designs of acoustofluidic system with integrated impedance-based detection system for cell phenotyping.

and cured at 80 ℃ for 2 hours. The cured PDMS replicas were then released from the master molds and access holes were punched before bonding to the glass slide with patterned electrodes. Alignment of electrodes to the microchannel was performed using methanol under microscope.

For the acoustofluidic device, the microchannel was fabricated in silicon by using reactive-ion etching (Plasmalab 100® ICP RIE, Oxford, UK) to a depth of 30 μm using aluminum as etching mask, and an isolation layer of 100 nm silicon dioxide was deposited by PECVD before bonding to the glass slide patterned with electrodes. The fabricated microchannel had a width of 187.5 μm. Anodic bonding was performed at 420 ℃ and 900 V for 6 hr to completely bond the silicon and glass layers. The increase in required temperature, voltage and time is mainly due to the two isolation layer that are 100 nm thick each. Also, for characterization device soda lime glass slide was used to pattern electrodes for its low cost, while for acoustofluidic device borofloat glass was used for anodic bonding. Fluidic access holes were drilled in the glass slide using a bench drill press (DP101, Ryobi Ltd, SC), and connected via flat-bottom ferrules (P-200N, Upchurch Scientific, WA) to Tygon® tubing (Saint-Gobain Performance Plastics, OH). Piezoelectric transducers (PZ26, Ferroperm Piezoceramics A/S, Denmark) were attached to the bottom of the microchip at desired positions by using wax (Crystalbond™ 509, SPI Supplies/Structure Probe Inc., PA).

4.4. Impedance-based position detection

4.4.1. Experimental

The performance of impedance-based particle/cell detection was characterized using the simple straight channel device fabricated with PDMS. Polystyrene beads were used for their uniform size and property, and were injected through the middle channel. By varying the flow rates of the three inlets, the Y positions of beads in the microchannel changed between left, middle, and right, which correspond to the position electrodes at top (narrow end), middle, and bottom (wide end). The optimal frequency for impedance detection was found by scanning the frequency range for best signal-to-noise ratio.

4.4.2. Results

Using 11 μm diameter polystyrene beads, it can be seen that there was a significant change of detected impedance of position electrodes (Fig. 4.4 and Fig. 4.5).

It can be seen that, from top to bottom the impedance amplitude decreased, which is understandable since the electric field is stronger at the top, and the passage of a cell disturbs the field at a greater impact. On the other hand, the peak width (measured at the half height of each peak) gradually increased from top to bottom, which corresponds to the distance that the beads need to pass.

The design of the position detection electrodes was optimized by characterizing the performance of three different tilting angles as in Fig. 4.2. From Fig. 4.4 and Fig. 4.5 it can been that P3 shows more expanded signal range with comparable variation to P1 and P2. This is mainly due to the increased change of electrode angle, which gives better

discrimination of particle position in Y direction. Therefore P3 was used for other experiments that require position detection electrode.

4.5. Integrated acoustofluidic system with impedance detection

After characterizing the performance of impedance-based position and size detection, it was integrated with the acoustofluidic system for cancer cell phenotyping. However it was found that the impedance of silicon wafer was too small that an isolation layer was needed prior to anodic bonding. Therefore 100 nm thick silicon dioxide was deposited on both patterned silicon wafer and patterned borofloat glass. The assembled device is shown in Fig. 4.5. However the detected impedance signal was very noisy, but the acoustic focusing of polystyrene beads was successfully demonstrated.

4.6. Discussions

Impedance-based detection provides a simple non-invasive and non-labeling approach to characterize dielectric properties of particles/cells, and can be utilized in microfluidic systems for size and position detection. The developed system allows an easy and simple way in general applications to detect, locate, and verify the position of particles/cells, especially in flow cytometry applications. Integrated with acoustofluidic system, cell phenotyping can be achieved using compact system design at high throughput and low cost, allowing the implementation of the acoustofluidic system in practical scenarios such as clinics.

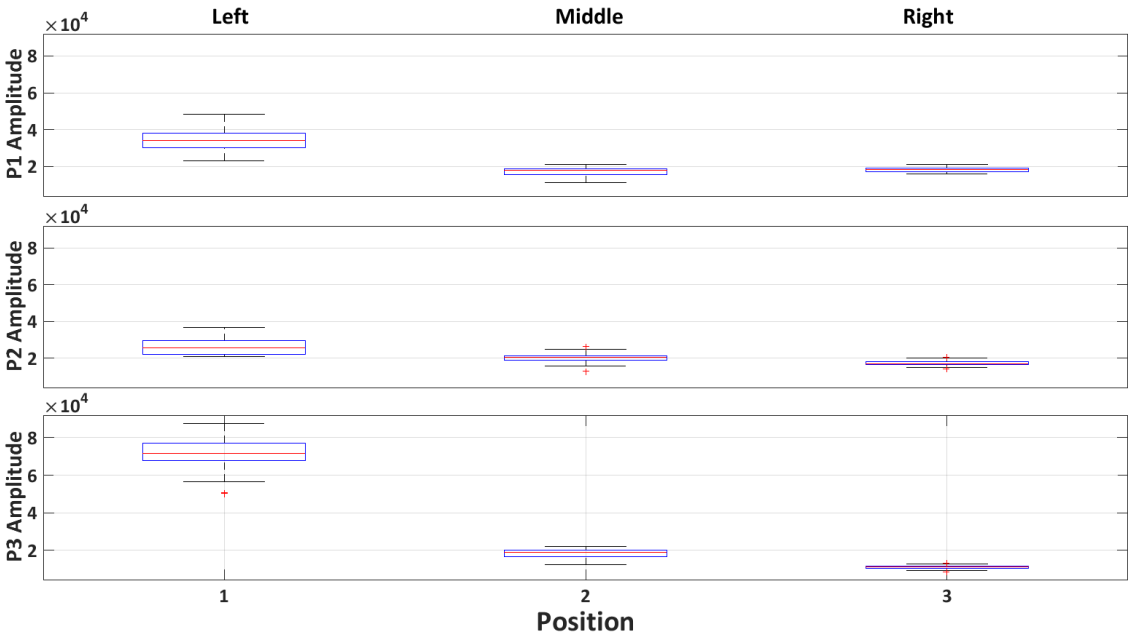

Fig. 4.4 Comparison of detected position signals (peak amplitude) from top (narrow end) to bottom (wide end) using polystyrene beads (diameter: 11 μm) with the three different designs.

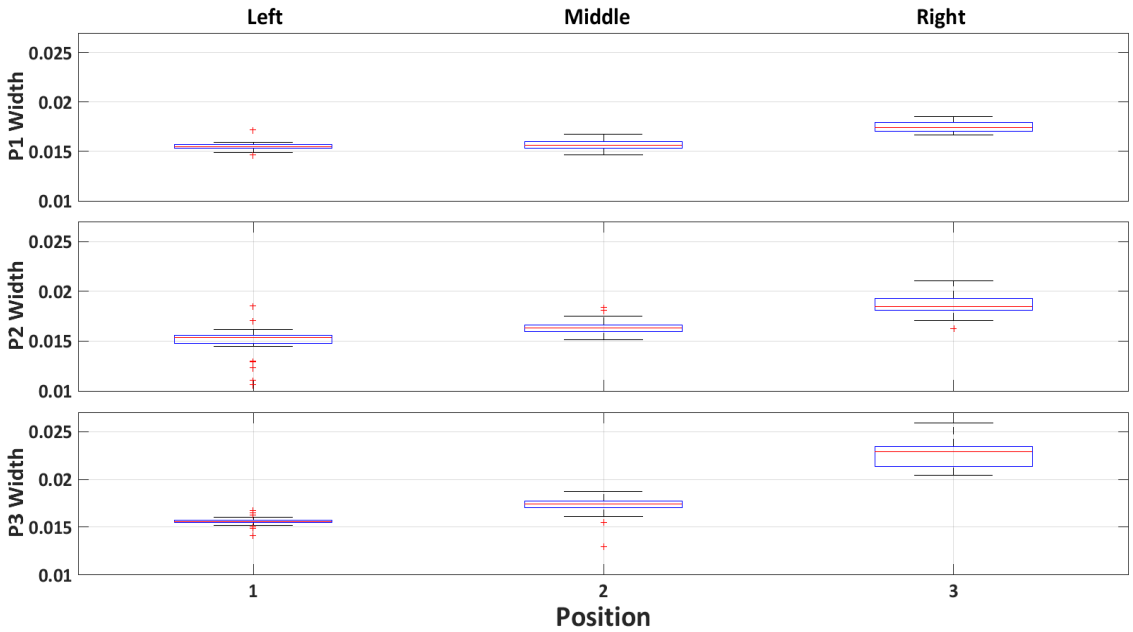

Fig. 4.5 Comparison of detected position signals (peak width) from top (narrow end) to bottom (wide end) using polystyrene beads (diameter: 11 μm) with the three different designs.

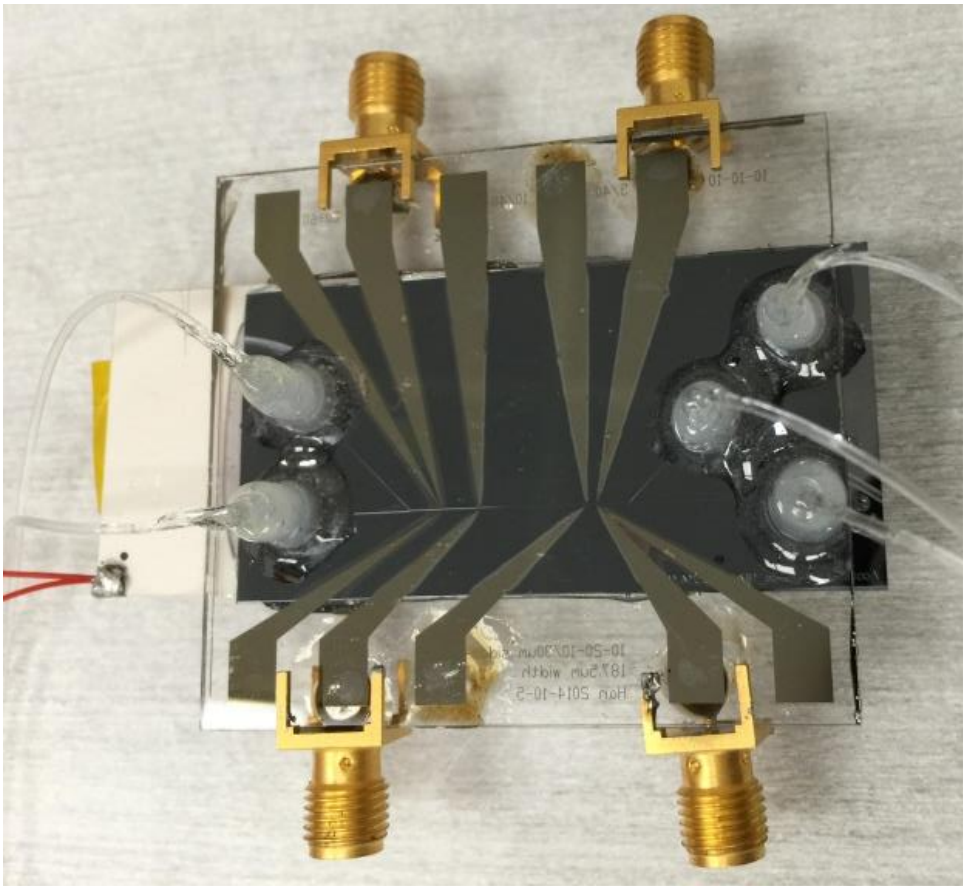

Fig. 4.6 Assembled acoustofluidic device integrated with impedance-based detection electrodes.

CHAPTER V

CONCLUSION AND FUTURE WORK

5.1. Conclusion

The integration of acoustics with microfluidics provides a powerful non-contact based particle and cell manipulation approach. Through this acoustofluidic technology a wide range of materials can be used as the target since the acoustic radiation force is regardless of electric and magnetic properties. Also since the field of operation is reduced to the order of micrometers, this offers a unique opportunity to study the mechanical properties of cells. The above presented work is part of the efforts in harnessing the power of acoustofluidics to be applied in a variety of applications, and the work in this field will continue to be proved promising with more applications come to the surface.

5.1.1. Oil droplet detection and separation

The developed continuous flow low concentration oil droplet detection and separation system was capable to detect oil droplet in aqueous solutions as low as 0.36 ppb, which was about three times higher than bench top oil detection system and about three thousand times higher than portable oil detectors currently available. The continuous flow oil droplet trapping scheme allows detecting ultra-low concentration of oil from a large sample volume. Also this system allows separation and collection of trapped oil

samples for further off-chip analyses. The developed system has the potential to be a low cost portable high sensitivity oil detector.

5.1.2. Cell biophysical property measurement

The developed acoustofluidic systems for cell mechanical property measurement have two configurations. The static flow system allows precise and robust control of cell position in 3-D space for trajectory monitoring to extract cell property, while the continuous flow system allows high throughput screening of cells with different mechanical properties. Both systems are promising platforms for clinical diagnosis of cancer progress and metastasis.

5.1.3. Integrated acoustofluidic system with impedance detection

Impedance detection of cells and particles has been widely used, and the developed system allows real-time detection of particle/cell size and position in Y-direction. Integrated with acoustofluidic system, this allows high throughput screening of cells with different mechanical properties, since their size and Y-direction deflection could be detected and quantified. This allows simple and low cost analysis of cell mechanical properties since no optical setup is required, replaced by two pairs of electrodes.

5.2. Future work

5.2.1. Cell biophysical property measurement

We have successfully developed a novel measurement approach of cell mechanical properties, and it requires a lot of screening studies on cancer cells with different metastatic potentials to reach a conclusion. In future cells with known (previously measured) mechanical properties such as MCF-7 and MCF-10A will be screened with this method, and compare the performance with other works.

Using the continuous flow scheme, the same cell lines will be screened to compare the trajectories and can potentially also extract the mechanical properties.

5.2.2. Acoustofluidics with integrated impedance detection

Impedance-based detection in microfluidic systems is a powerful and versatile tool and has broad applications. Integrated with acoustofluidic system, this platform allows simple and real time detection and characterization of particle/cell size and position. There're still technical hurdles in improving the performance and fully unleash the potential. We see the fully developed system a powerful and easy to use tool to quickly perform cell phenotyping based on their vibro-acoustic properties, which has great utility in clinical diagnostics and research.

REFERENCES

1. S. J. M. Todd Thorsen, Stephen R. Quake, *Science*, 2002.

2. D. I. Darwin R. Reyes, Pierre-Alain Auroux, Andreas Manz, *Anal. Chem.*, 2002.

3. P.-A. Auroux, D. Iossifidis, D. R. Reyes and A. Manz, *Analytical Chemistry*, 2002, **74**, 2637-2652.

4. S. H. a. R. Zengerle, *Lab Chip*, 2007.

5. T. Laurell, F. Petersson and A. Nilsson, *Chemical Society Reviews*, 2007, **36**, 492-506.

6. A. Lenshof, M. Evander, T. Laurell and J. Nilsson, *Lab on a Chip*, 2012, **12**, 684-695.

7. H. J. J., G. Martin, B. Ewald, N. Helmut and C. W. Terence, in *Proc. Forum Acusticum*, Sevilla, 2002.

8. J. D. N. Cheeke, *Fundamentals and Applications of Ultrasonic Waves*, Taylor & Francis, 2002.

9. S.-C. S. Lin, X. Mao and T. J. Huang, *Lab on a Chip*, 2012, **12**, 2766-2770.

10. X. Ding, P. Li, S.-C. S. Lin, Z. S. Stratton, N. Nama, F. Guo, D. Slotcavage, X. Mao, J. Shi, F. Costanzo and T. J. Huang, *Lab on a Chip*, 2013, **13**, 3626-3649.

11. J. Shi, S. Yazdi, S.-C. Steven Lin, X. Ding, I. K. Chiang, K. Sharp and T. J. Huang, *Lab on a Chip*, 2011, **11**, 2319-2324.

12. L. V. King, *Proceedings of the Royal Society of London. Series A - Mathematical and Physical Sciences*, 1934, **147**, 212-240.

13. K. Yosioka and Y. Kawasima, *Acustica*, 1955, **5**, 167-173.

14. L. P. Gorkov, *Sov. Phys. Dokl.*, 1962, **6**, 773.

15. W. L. Nyborg, *The Journal of the Acoustical Society of America*, 1967, **42**, 947-952.

16. G. Ter Haar and S. J. Wyard, *Ultrasound in medicine & biology*, 1978, **4**, 111-123.

17. C. Collinson and T. Roper, *Particle Mechanics*, Elsevier Science, 1995.

18. O. Doblhoff-Dier, T. Gaida, H. Katinger, W. Burger, M. Groschl and E. Benes, *Biotechnology Progress*, 1994, **10**, 428-432.

19. K. Yasuda, S. Umemura and K. Takeda, *Jpn J Appl Phys 1*, 1995, **34**, 2715-2720.

20. Z. I. Mandralis, D. L. Feke and R. J. Adler, *Fluid/Particle Separation Journal*, 1990, **3**, 115-121.

21. P. Glynne-Jones, R. J. Boltryk and M. Hill, *Lab on a Chip*, 2012, **12**, 1417-1426.

22. J. J. Hawkes and W. T. Coakley, *Sensors and Actuators B: Chemical*, 2001, **75**, 213-222.

23. N. R. Harris, M. Hill, S. Beeby, Y. Shen, N. M. White, J. J. Hawkes and W. T. Coakley, *Sensors and Actuators B: Chemical*, 2003, **95**, 425-434.

24. B. Hammarstrom, M. Evander, H. Barbeau, M. Bruzelius, J. Larsson, T. Laurell and J. Nilsson, *Lab Chip*, 2010, **10**, 2251-2257.

25. D. A. Johnson and D. L. Feke, *Separations Technology*, 1995, **5**, 251-258.

26. S. Gupta, D. L. Feke and I. Manas-Zloczower, *Chemical Engineering Science*, 1995, **50**, 3275-3284.

27. C. Ratier and M. Hoyos, *Analytical Chemistry*, 2010, **82**, 1318-1325.

28. Z. I. Mandralis and D. L. Feke, *AIChE Journal*, 1993, **39**, 197-206.

29. C. Siversson, F. Petersson, A. Nilsson and T. Laurell, in *Micro Total Analysis Systems*, The Royal Society of Chemistry Malmö, Sverige, 2004, pp. 330 - 332.

30. N. Harris, R. Boltryk, P. Glynne-Jones and M. Hill, *Physics Procedia*, 2010, **3**, 277-281.

31. J. J. Hawkes, M. J. Long, W. T. Coakley and M. B. McDonnell, *Biosensors and Bioelectronics*, 2004, **19**, 1021-1028.

32. R. J. Townsend, M. Hill, N. R. Harris and M. B. McDonnell, *Ultrasonics*, 2008, **48**, 515-520.

33. S. Kapishnikov, V. Kantsler and V. Steinberg, *J Stat Mech-Theory E*, 2006, **2006**, P01012.

34. S. Radel, M. Brandstetter and B. Lendl, *Ultrasonics*, 2010, **50**, 240-246.

35. T. Kanazaki, S. Hirawa, M. Harada and T. Okada, *Analytical Chemistry*, 2010, **82**, 4472-4478.

36. D. Bazou, G. P. Dowthwaite, I. M. Khan, C. W. Archer, J. R. Ralphs and W. Terence Coakley, *Molecular Membrane Biology*, 2006, **23**, 195-205.

37. G. O. Edwards, D. Bazou, L. A. Kuznetsova and W. T. Coakley, *Cell Communication and Adhesion*, 2007, **14**, 9-20.

38. V. G. Zarnitsyn and M. R. Prausnitz, *Ultrasound in medicine & biology*, 2004, **30**, 527-538.

39. J. M. Escoffre, K. Kaddur, M. P. Rols and A. Bouakaz, *Ultrasound in medicine & biology*, 2010, **36**, 1746-1755.

40. D. Carugo, D. N. Ankrett, P. Glynne-Jones, L. Capretto, R. J. Boltryk, X. Zhang, P. A. Townsend and M. Hill, *Biomicrofluidics*, 2011, **5**, 44108.

41. S. Rodamporn, N. R. Harris, S. P. Beeby, R. J. Boltryk and T. Sanchez-Eisner, *Biomedical Engineering, IEEE Transactions on*, 2011, **58**, 927-934.

42. A. Lenshof, A. Ahmad-Tajudin, K. Järås, A.-M. Swärd-Nilsson, L. Åberg, G. Marko-Varga, J. Malm, H. Lilja and T. Laurell, *Analytical Chemistry*, 2009, **81**, 6030-6037.

43. F. Petersson, L. Åberg, A.-M. Swärd-Nilsson and T. Laurell, *Analytical Chemistry*, 2007, **79**, 5117-5123.

44. P. Thévoz, J. D. Adams, H. Shea, H. Bruus and H. T. Soh, *Analytical Chemistry*, 2010, **82**, 3094-3098.

45. P. Augustsson, C. Magnusson, C. Grenvall, H. Lilja and T. Laurell, in *Micro Total Analysis Systems*, Groningen, Netherlands, 2010, pp. 1592–1594.

46. J. D. Adams and H. T. Soh, *Applied Physics Letters*, 2010, **97**, 064103.

47. Y. Liu and K.-M. Lim, *Lab on a Chip*, 2011, **11**, 3167-3173.

48. M. Groschl, *Acustica*, 1998, **84**, 432-447.

49. J. Wu, *The Journal of the Acoustical Society of America*, 1991, **89**, 2140-2143.

50. H. M. Hertz, *Journal of Applied Physics*, 1995, **78**, 4845-4849.

51. M. Evander, L. Johansson, T. Lilliehorn, J. Piskur, M. Lindvall, S. Johansson, M. Almqvist, T. Laurell and J. Nilsson, *Anal Chem*, 2007, **79**, 2984-2991.

52. M. Evander and J. Nilsson, *Lab on a Chip*, 2012, **12**, 4667-4676.

53. O. Manneberg, B. Vanherberghen, B. Onfelt and M. Wiklund, *Lab on a Chip*, 2009, **9**, 833-837.

54. J. Svennebring, O. Manneberg, P. Skafte-Pedersen, H. Bruus and M. Wiklund, *Biotechnology and Bioengineering*, 2009, **103**, 323-328.

55. H. Wang, Z. Liu, S. Kim, C. Koo, Y. Cho, D.-Y. Jang, Y.-J. Kim and A. Han, *Lab on a Chip*, 2014, **14**, 947-956.

56. O. Manneberg, S. Melker Hagsäter, J. Svennebring, H. M. Hertz, J. P. Kutter, H. Bruus and M. Wiklund, *Ultrasonics*, 2009, **49**, 112-119.

57. P. Augustsson, R. Barnkob, C. Grenvall, T. Deierborg, P. Brundin, H. Bruus and T. Laurell, in *Proceedings of the 14. International Conference on Miniaturized Systems for Chemistry and Life Sciences*, 2010, pp. 1337-1339.

58. R. Barnkob, P. Augustsson, C. Magnusson, H. Lilja, T. Laurell and H. Bruus, in *Proceedings of the 15th International Conference on Miniaturized Systems for Chemistry and Life Sciences*, 2011, pp. 127-129.

59. D. Hartono, Y. Liu, P. L. Tan, X. Y. S. Then, L.-Y. L. Yung and K.-M. Lim, *Lab on a Chip*, 2011, **11**, 4072-4080.

60. H. Wang, Z. Liu, D. M. Shin, Z. Chen, Y. Cho, D.-Y. Jang, Y.-J. Kim and A. Han, *Proceedings of Meetings on Acoustics*, 2013, **19**, 045019-045019.

61. T. Frommelt, M. Kostur, M. Wenzel-Schäfer, P. Talkner, P. Hänggi and A. Wixforth, *Physical Review Letters*, 2008, **100**, 034502.

62. A. Wixforth, *Superlattices and Microstructures*, 2003, **33**, 389-396.

63. P. R. Rogers, J. R. Friend and L. Y. Yeo, *Lab on a Chip*, 2010, **10**, 2979-2985.

64. T. Franke, A. R. Abate, D. A. Weitz and A. Wixforth, *Lab on a Chip*, 2009, **9**, 2625-2627.

65. T. Franke, S. Braunmuller, L. Schmid, A. Wixforth and D. A. Weitz, *Lab on a Chip*, 2010, **10**, 789-794.

66. S. Li, X. Ding, F. Guo, Y. Chen, M. I. Lapsley, S.-C. S. Lin, L. Wang, J. P. McCoy, C. E. Cameron and T. J. Huang, *Analytical Chemistry*, 2013, **85**, 5468-5474.

67. J. Shi, H. Huang, Z. Stratton, Y. Huang and T. J. Huang, *Lab on a Chip*, 2009, **9**, 3354-3359.

68. J. Nam, H. Lim, C. Kim, J. Yoon Kang and S. Shin, *Biomicrofluidics*, 2012, **6**, 24120-2412010.

69. X. Ding, S.-C. S. Lin, B. Kiraly, H. Yue, S. Li, I.-K. Chiang, J. Shi, S. J. Benkovic and T. J. Huang, *Proceedings of the National Academy of Sciences*, 2012, **109**, 11105-11109.

70. C. H. Peterson, S. D. Rice, J. W. Short, D. Esler, J. L. Bodkin, B. E. Ballachey and D. B. Irons, *Science*, 2003, **302**, 2082-2086.

71. D. A. Gill, J. S. Picou and L. A. Ritchie, *American Behavioral Scientist*, 2012, **56**, 3-23.

72. R. R. Lessard and G. DeMarco, *Spill Science & Technology Bulletin*, 2000, **6**, 59-68.

73. P. Nounou, *Ambio*, 1980, **9**, 297-302.

74. R. K. Nelson, Kile, B.M., Plata, D.L., Sylva, D.P., Xu, L., Reddy, C.M., Gaines, R.B., Frysinger, G.S., and Reichenbach, S.E., *Environmental Forensics*, 2006, **7**, 33-44.

75. G. D. Marty, D. E. Hinton, J. W. Short, R. A. Heintz, S. D. Rice, D. M. Dambach, N. H. Willits and J. J. Stegeman, *Canadian Journal of Zoology*, 1997, **75**, 989-1007.

76. R. A. Heintz, S. D. Rice, A. C. Wertheimer, R. F. Bradshaw, F. P. Thrower, J. E. Joyce and J. W. Short, *Marine Ecology Progress Series*, 2000, **208**, 205-216.

77. M. F. Fingas and C. E. Brown, *Spill Science & Technology Bulletin*, 1997, **4**, 199-208.

78. M. Jha, J. Levy and Y. Gao, *Sensors*, 2008, **8**, 236-255.

79. P. D. Keizer and D. C. Gordon Jr, *Journal of the Fisheries Research Board of Canada*, 1973, **30**, 1039-1046.

80. R. Camilli, C. M. Reddy, D. R. Yoerger, B. A. S. Van Mooy, M. V. Jakuba, J. C. Kinsey, C. P. McIntyre, S. P. Sylva and J. V. Maloney, *Science*, 2010, **330**, 201-204.

81. A.-R. Diercks, R. C. Highsmith, V. L. Asper, D. Joung, Z. Zhou, L. Guo, A. M. Shiller, S. B. Joye, A. P. Teske, N. Guinasso, T. L. Wade and S. E. Lohrenz, *Geophysical Research Letters*, 2010, **37**, L20602.

82. W. G. Mendoza, D. D. Riemer and R. G. Zika, *Environmental Science: Processes & Impacts*, 2013, **15**, 1017-1030.

83. P. Lambert, *Journal of Hazardous Materials*, 2003, **102**, 39-55.

84. K. Trudel, Belore, R., VanHaverbeke, M., Mullin, J., in *Proceedings of the Thirty-second Arctic and Marine Oillspill Program (AMOP) Technical Seminar*, Environment Canada, Ottawa, Canada, 2009, pp. 397–410.

85. M. Kim, U. H. Yim, S. H. Hong, J.-H. Jung, H.-W. Choi, J. An, J. Won and W. J. Shim, *Marine Pollution Bulletin*, 2010, **60**, 383-389.

86. A. M. Castro, J. Delgado and G. Orellana, *Journal of Materials Chemistry*, 2005, **15**, 2952-2958.

87. M. Wiklund, P. Spégel, S. Nilsson and H. M. Hertz, *Ultrasonics*, 2003, **41**, 329-333.

88. A. Nilsson, F. Petersson, H. Jonsson and T. Laurell, *Lab Chip*, 2004, **4**, 131-135.

89. T. Lilliehorn, U. Simu, M. Nilsson, M. Almqvist, T. Stepinski, T. Laurell, J. Nilsson and S. Johansson, *Ultrasonics*, 2005, **43**, 293-303.

90. F. Petersson, A. Nilsson, C. Holm, H. Jonsson and T. Laurell, *Lab on a Chip*, 2005, **5**, 20-22.

91. O. Doblhoffdier, T. Gaida, H. Katinger, W. Burger, M. Groschl and E. Benes, *Biotechnology Progress*, 1994, **10**, 428-432.

92. K. Yasuda, S. S. Haupt, S. Umemura, T. Yagi, M. Nishida and Y. Shibata, *J. Acoust. Soc. Am.*, 1997, **102**, 642-645.

93. O. Manneberg, J. Svennebring, H. M. Hertz and M. Wiklund, *Journal of Micromechanics and Microengineering*, 2008, **18**, 095025.

94. Z. Wang and M. Fingas, *Journal of Chromatography A*, 1997, **774**, 51-78.

95. S. E. Cross, Y. S. Jin, J. Tondre, R. Wong, J. Rao and J. K. Gimzewski, *Nanotechnology*, 2008, **19**, 384003.

96. M. Mak, C. A. Reinhart-King and D. Erickson, *Lab on a Chip*, 2013, **13**, 340-348.

97. S. Kang, S. Elf, K. Lythgoe, T. Hitosugi, J. Taunton, W. Zhou, L. Xiong, D. Wang, S. Muller, S. Fan, S. Y. Sun, A. I. Marcus, T. L. Gu, R. D. Polakiewicz, Z. G. Chen, F. R. Khuri, D. M. Shin and J. Chen, *J Clin Invest*, 2010, **120**, 1165-1177.

98. C. T. Lim, E. H. Zhou, A. Li, S. R. K. Vedula and H. X. Fu, *Materials Science and Engineering: C*, 2006, **26**, 1278-1288.

99. G. Y. H. Lee and C. T. Lim, *Trends in Biotechnology*, 2007, **25**, 111-118.

100. S. Suresh, *Acta Biomaterialia*, 2007, **3**, 413-438.

101. M. Lekka, P. Laidler, D. Gil, J. Lekki, Z. Stachura and A. Z. Hrynkiewicz, *Eur Biophys J*, 1999, **28**, 312-316.

102. Q. S. Li, G. Y. H. Lee, C. N. Ong and C. T. Lim, *Biochemical and Biophysical Research Communications*, 2008, **374**, 609-613.

103. S. Leporatti, D. Vergara, A. Zacheo, V. Vergaro, G. Maruccio, R. Cingolani and R. Rinaldi, *Nanotechnology.*, 2009, **20**, 055103.

104. R. M. Hochmuth, *Journal of Biomechanics*, 2000, **33**, 15-22.

105. F. J. Byfield, H. Aranda-Espinoza, V. G. Romanenko, G. H. Rothblat and I. Levitan, *Biophys J.*, 2004, **87**, 3336-3343. Epub 2004 Sep 3333.

106. E. H. Zhou, C. T. Lim, K. S. W. Tan, S. T. Quek, A. Lee and B. Liau, in *Proceedings of the 2nd World Congress for Chinese Biomedical Engineers*, Beijing, China, 2004.

107. W. Kim and A. Han, in *The 14th International Conference on Miniaturized Systems for Chemistry and Life Sciences*, Groningen, The Netherlands, 2010, 253-255.

108. A. Ashkin and J. M. Dziedzic, *Physical Review Letters*, 1985, **54**, 1245-1248.

109. A. Ashkin, J. M. Dziedzic and T. Yamane, *Nature*, 1987, **330**, 769-771.

110. T. W. Remmerbach, F. Wottawah, J. Dietrich, B. Lincoln, C. Wittekind and J. Guck, *Cancer Research*, 2009, **69**, 1728-1732.

111. J. Guck, S. Schinkinger, B. Lincoln, F. Wottawah, S. Ebert, M. Romeyke, D. Lenz, H. M. Erickson, R. Ananthakrishnan, D. Mitchell, J. Kas, S. Ulvick and C. Bilby, *Biophys J*, 2005, **88**, 3689-3698.

112. F. J. Alenghat, B. Fabry, K. Y. Tsai, W. H. Goldmann and D. E. Ingber, *Biochemical and Biophysical Research Communications*, 2000, **277**, 93-99.

113. V. r. M. Laurent, S. Hénon, E. Planus, M. Balland, D. Isabey, F. o. Gallet and R. Fodil, *Journal of Biomechanical Engineering*, 2002, **124**, 408-421.

114. A. Adamo, A. Sharei, L. Adamo, B. Lee, S. Mao and K. F. Jensen, *Analytical Chemistry*, 2012, **84**, 6438-6443.

115. C. H. D. Tsai, S. Sakuma, F. Arai and M. Kaneko, *Biomedical Engineering, IEEE Transactions on*, 2014, **61**, 1187-1195.

116. H. W. Hou, A. A. S. Bhagat, A. G. Lin Chong, P. Mao, K. S. Wei Tan, J. Han and C. T. Lim, *Lab on a Chip*, 2010, **10**, 2605-2613.

117. S. C. Hur, N. K. Henderson-MacLennan, E. R. B. McCabe and D. Di Carlo, *Lab on a Chip*, 2011, **11**, 912-920.

118. H. T. K. Tse, D. R. Gossett, Y. S. Moon, M. Masaeli, M. Sohsman, Y. Ying, K. Mislick, R. P. Adams, J. Rao and D. Di Carlo, *Science Translational Medicine*, 2013, **5**, 212ra163.

119. A. Lenshof, C. Magnusson and T. Laurell, *Lab on a Chip*, 2012, **12**, 1210-1223.

120. D. D. Reynolds, *Engineering Principles of Acoustics: Noise and Vibration Control*, Allyn and Bacon, 1981.

121. John Happel and H. Brenner, *Low Reynolds number hydrodynamics*, Martinus Nijhoff Publisher, 1983.

122. P. Ganatos, S. Weinbaum and R. Pfeffer, *Journal of Fluid Mechanics*, 2006, **99**, 739.

123. L. Lobry and N. Ostrowsky, *Physical Review B*, 1996, **53**, 12050-12056.

APPENDIX A

MASK DESIGN

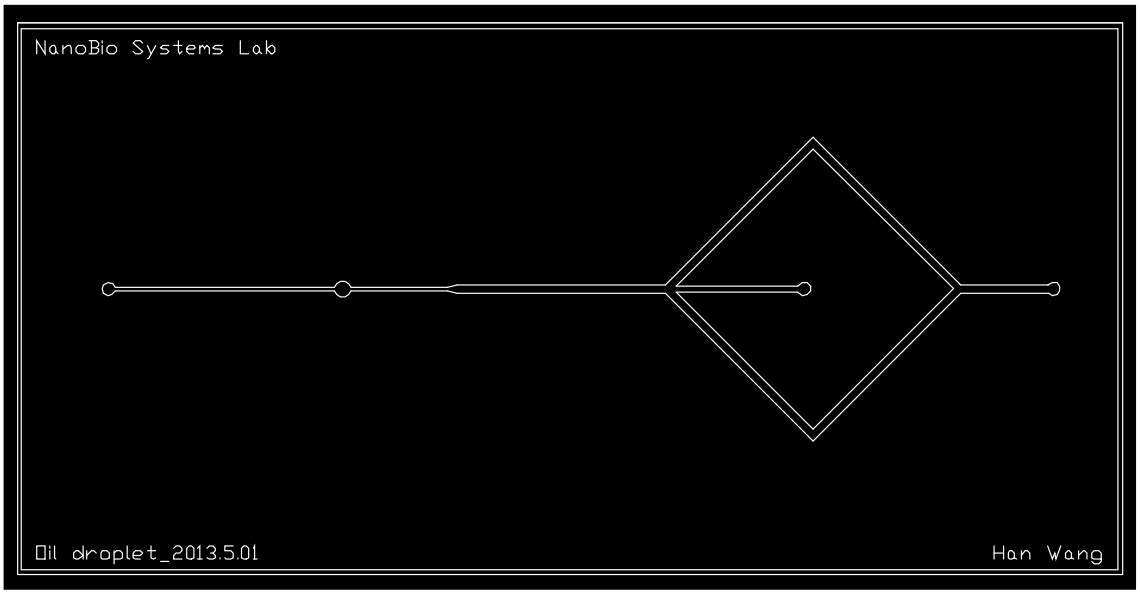

Fig. A.1 Oil droplet detection and trapping device.

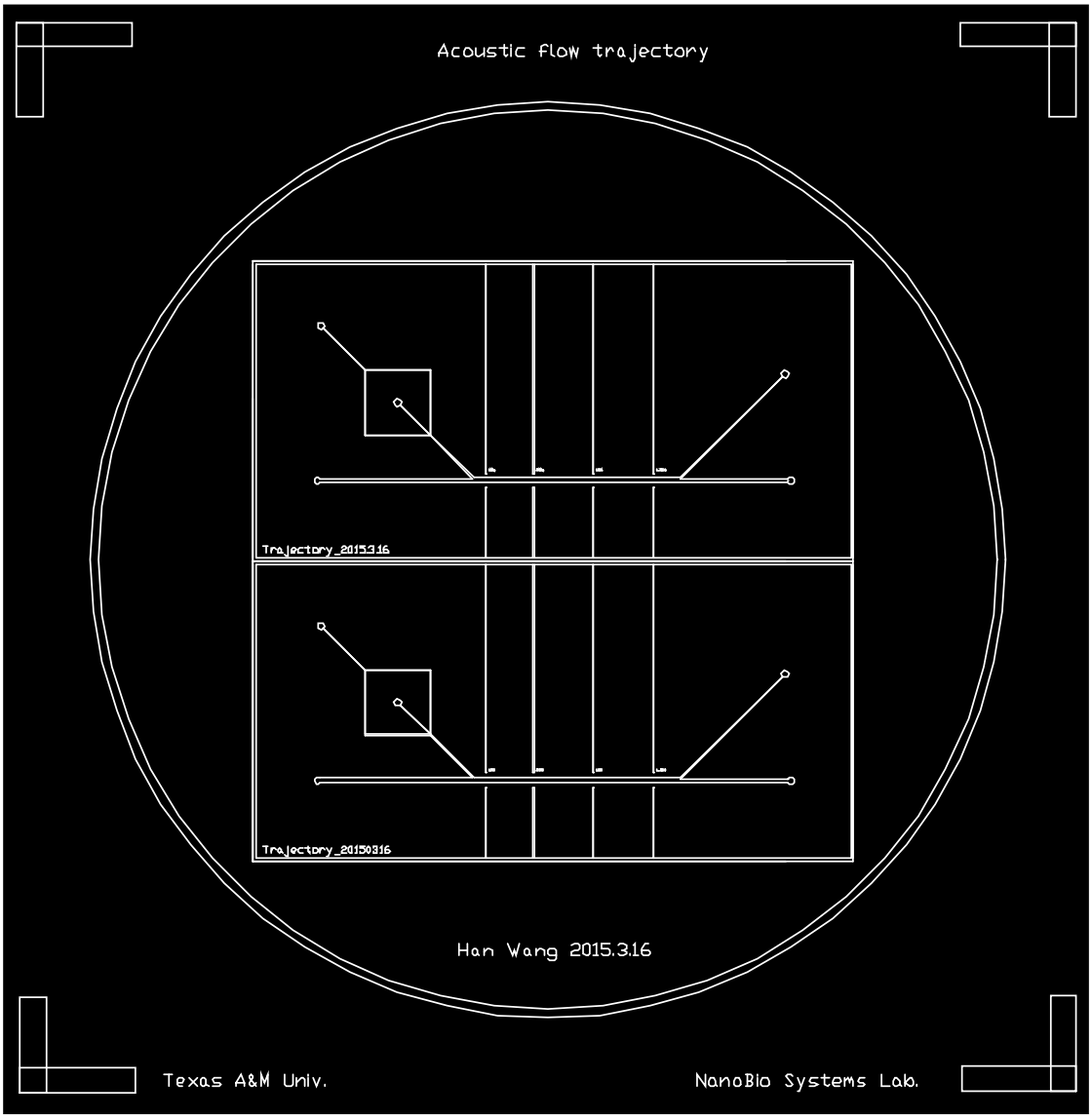

Fig. A.2 Acoustophoretic continuous flow cell biophysical property measurement device.

Fig. A.3 Acoustophoretic static flow cell biophysical property measurement device.

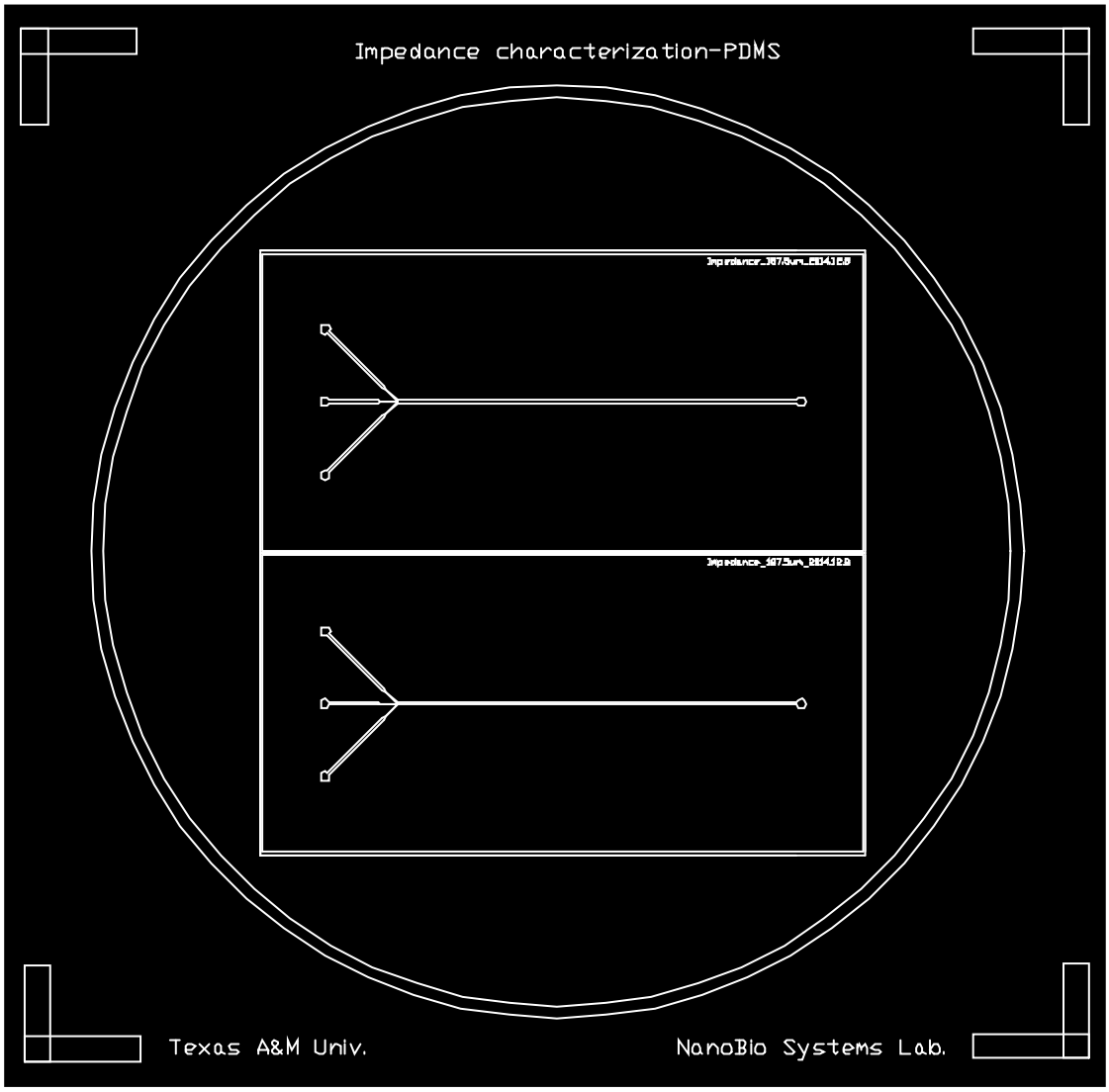

Fig. A.4 Impedance based particle size and position characterization device.

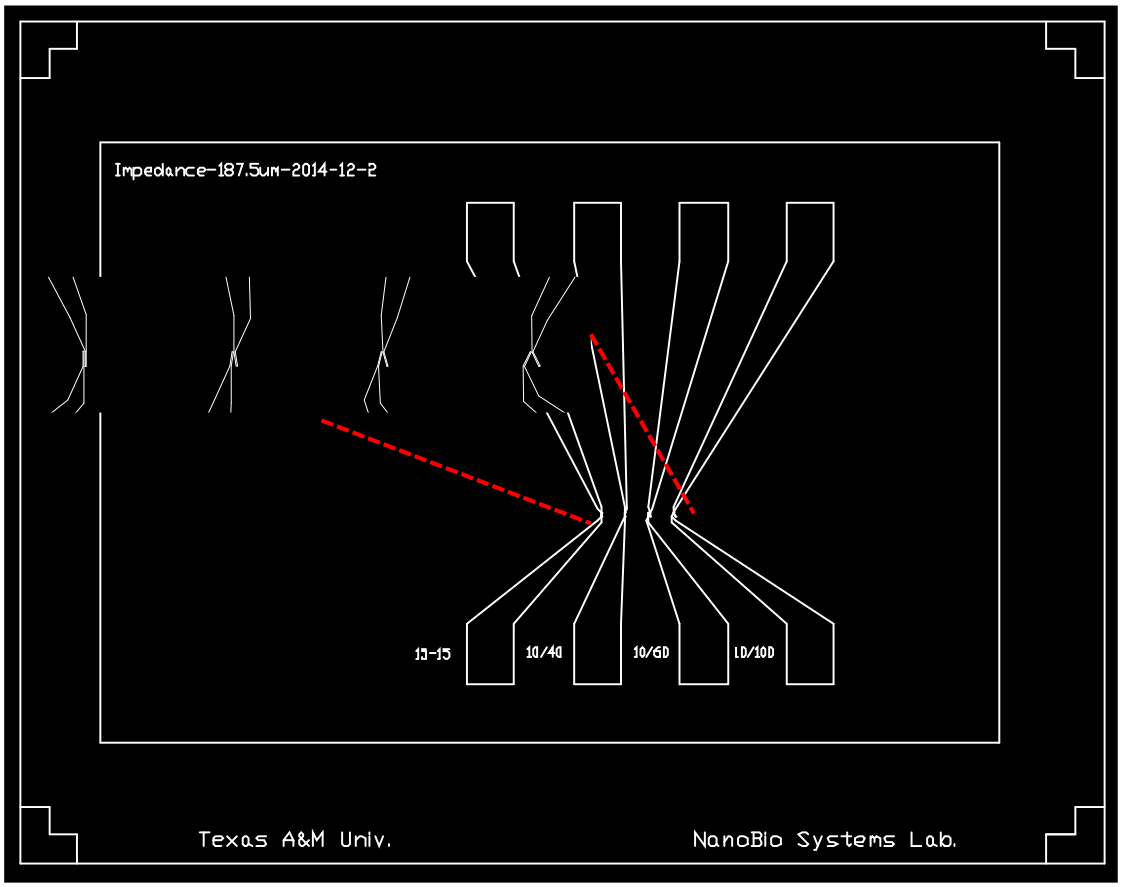

Fig. A.5 Electrodes for impedance based particle size and position characterization device. Insert: enlarged electrodes with different angles for position detection.

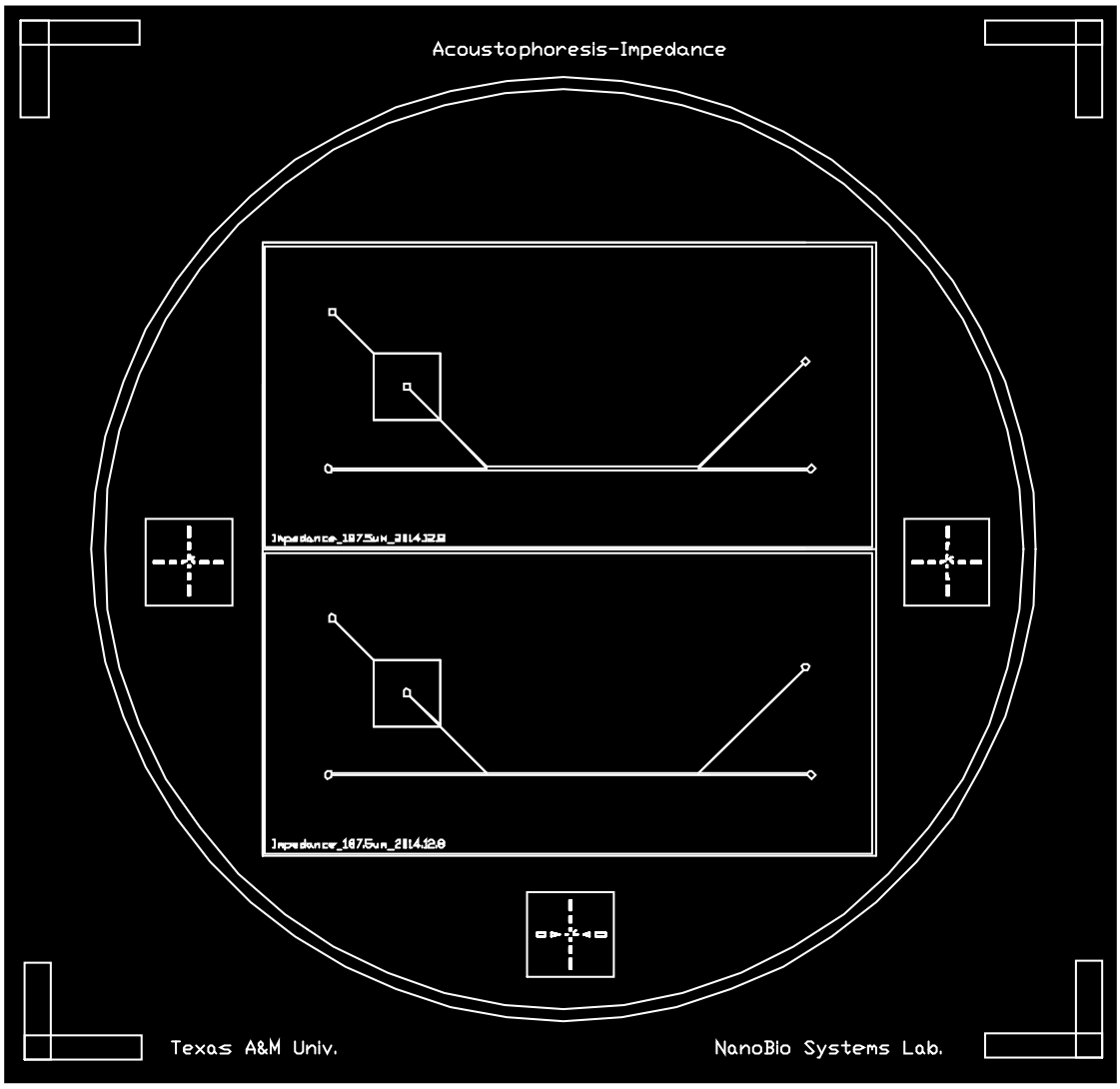

Fig. A.6 Acoustofluidic device integrated with impedance based particle size and position detection.

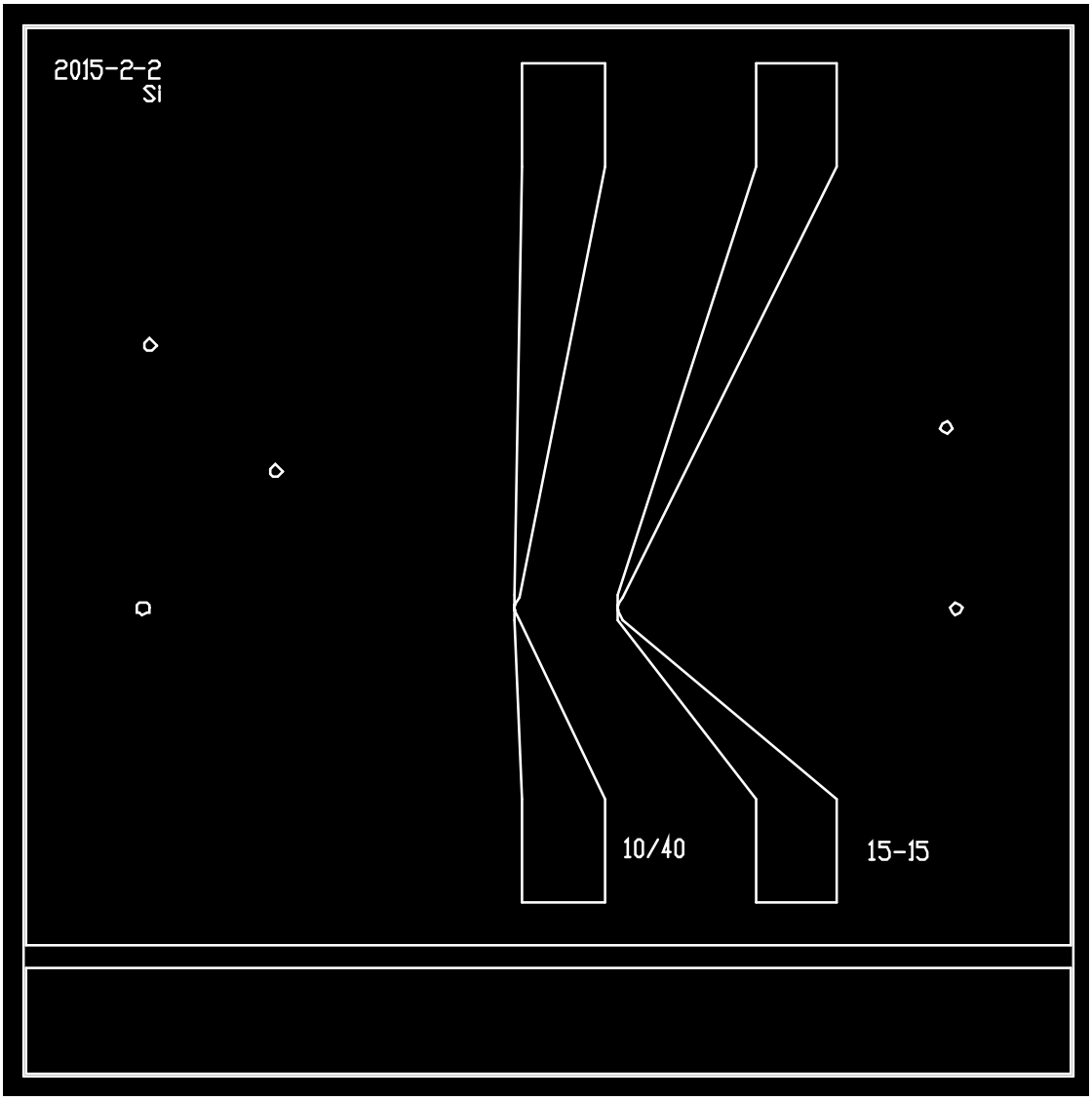

Fig. A.7 Electrodes for acoustofluidic device integrated with impedance based particle size and position detection.

APPENDIX B

SILICON WAFER FABRICATION PROCEDURE

B.1. Aluminum Etching Mark Patterning

1. Clean the 3 inch silicon wafer with piranha at 3:1 ratio for 30 min

2. Deposit Al layer using a PVD evaporator to a thickness of 5000 Å

3. Clean the wafer with acetone, IPA, and DI water and dry with N_2 gas

4. Dehydrate baking at 200 ℃ for 10 minutes

5. Spin coat Microposit S1818 photoresist (Rohm and Haas Electronic Material LLC, Marlborough, MA) on the silicon wafer at 4000 rpm for 30 seconds with an acceleration time of 5 seconds

6. Soft baking at 110 ℃ for 10 minutes, cool down

7. Expose UV using a mask aligner (MJB3, SUSS MicroTec Inc., Waterbury Center, VT) at 12 mW/cm^2 (wavelength: 320 nm) for 10 second with a photomask having alignment marks

8. Develop the pattern using MF-319 developer (Rohm and Haas Electronic Material LLC, Marlborough, MA) for 20-40 seconds

9. Rinse in DI water and dry with N_2 gas

10. Hard baking at 120 ℃ for 10 min

10. Etch uncovered Aluminum with Aluminum etchant for about 20 min

11. Rinse the wafer with acetone, IPA, and DI water in sequence, and dry with N_2 gas

B.2. RIE Etching

1. Cryogenic etching of silicon wafer with Oxford PlasmaLab 100 RIE machine using aluminum (500 nm thick) as etching mask

2. Run chamber cleaning recipe for 15 min prior to each etching

3. Use the optimized cryogenic etching recipe as shown in Table B.1

4. The average etching rate is about 3 μm/min

5. Remove the aluminum etching mask

Table B.1 Optimized RIE conditions for cryogenic Si etching.

SF_6/O_2 (sccm)	70/4	Temperature (℃)	-100
APC (mTorr)	10	Forward power (W)	10
ICP (W)	900	Etch rate (μm/min)	3.202
Etch mask	Al (500 nm)		

B.3. Anodic Bonding

1. Mark access holes on borofloat coverglass, attach coverglass to glass slide backing with wax

2. Drill access holes in coverglass, add a drop of water while drilling, also use black rubber as vibration absorber below the glass slide

3. Remove wax on coverglass by sonication in acetone solution for 5 min, and quickly rinse with acetone after taking out

4. Clean the etched silicon wafer and coverglass with piranha solution at 3:1 ratio for 30 min

5. Align silicon wafer with coverglass and add a small drop of water or methanol for attachment, put the two in the direction that the coverglass is facing down in contact with cathode (ground) plate, while the anode wire was brought into contact with silicon wafer, use ceramic to cover the wafers

6. Anodic bonding was done at 400 ℃ with 700 V for 40 min

7. In the case of bonding silicon wafer and glass electrodes, since there's silicon dioxide layer only clean with acetone or quickly dip in piranha for 2 min, and bond at 420 ℃ with 900 V overnight (~ 12 hr)

B.4. Electrode Pattern on Glass Slide

1. Deposit 50 nm of chrome and 200 nm of gold on the glass slide (borofloat glass for anodic bonding, soda lime glass for bonding with PDMS)

2. Rinse the glass slide with acetone, IPA, and DI water in sequence, and dry with N_2 gas

3. Dehydrate baking at 200 ℃ for 10 minutes

4. Spin coat Microposit S1818 photoresist (Rohm and Haas Electronic Material LLC, Marlborough, MA) on the silicon wafer at 4000 rpm for 30 seconds with an acceleration time of 5 seconds

5. Soft baking at 110 ℃ for 10 minutes, cool down

6. Expose UV using a mask aligner (MJB3, SUSS MicroTec Inc., Waterbury Center, VT) at 12 mW/cm^2 (wavelength: 320 nm) for 10 second with a photomask having alignment marks

7. Develop the pattern using MF-319 developer (Rohm and Haas Electronic Material LLC, Marlborough, MA) for 20-40 seconds

8. Post exposure baking at 120 ℃ for 10 minutes, cool down

9. Etch gold and chrome layer

10. Remove photoresist etching mask

11. Rinse with DI water, and dry with N_2 gas

B.4. PDMS Master Fabrication

1. Rinse a bare 3 inch silicon wafer with acetone, IPA, and DI water in sequence, and dry with N_2 gas

2. Dehydrate baking at 200 ℃ for 10 minutes

3. Spin coat 24 μm thick photoresist (SU-8™ 2015, Microchem, Inc., Newton, MA) on the pre- pattered silicon wafer at 2000 rpm for 40 seconds

4. Soft baking at 65 ℃ for 15 minutes, followed by 95 ℃ baking for 30 minutes, cool down

5. Expose UV using a mask aligner (MA6, SUSS MicroTec Inc., Waterbury Center, VT) at 220 mJ/cm^2 with the PDMS channel photomask

6. Post exposure baking at 65 ℃ for 10 minutes, followed by 95 ℃ baking for 30 minutes, cool down

7. Develop the patterns using SU-8 developer (Microchem, Inc., Newton, MA) for about 3 minutes

8. Rinse with IPA and DI water, and dry with N_2 gas

B.5. PDMS Soft Lithography

1. Place the fabricated silicon master mold wafers inside the desiccator together with a weight boat containing 6 ~ 7 drops of tridecafluoro-1,1,2,2-tetrahydrooctyl (trichlorosilane, United Chemical Technologies, Inc., Bristol, PA)

2. Vacuum the desiccator for 10 min to allow trichlorosilane vaporize and evenly sprayed over the wafers

3. Mix PDMS (Sylgard® 184, Dow Corning, Inc., Midland, MI) prepolymer with curing agent at 10 : 1 ratio, and degas in a desiccator for 10 minutes

4. Pour the degassed PDMS prepolymer mixture onto trichlorosilane coated master wafers for about 20 g per 3 inch wafer, and degas again in the desiccator for 10 min

5. Cure in an 85 ℃ oven for 2 hr

B.6. PDMS Device Bonding

1. Peel off and trim the cured PDMS channel block

2. Punch holes in the PDMS block with a gauge 19 needle

3. Clean both PDMS device and glass with patterned electrode using acetone, IPA, and DI water, blow dry with N_2 gun

4. Apply oxygen plasma treatment (100 mTorr, 100W, 45 sec) for both fluidic layer membrane and pneumatic layer block, visually align under a stereo microscope with methanol

5. Bake on a 80 ℃ hotplate for 8 hr

APPENDIX C

CELL CULTURE PROTOCOL

C.1. Materials and Reagents

[HCT116-MKI67-1000 GFP, MCF-7] (RPMI 1640)

1 L: RPMI 1640 (Invitrogen, Catalog number: 11875-085) with 10% Fetal Bovine Serum (Invitrogen, Catalog number: 16000-044), 20 mM HEPES (Invitrogen, Catalog number: 15630-080), 2-4 mM additional L-Glutamine and 100 units/ml of Penicillin/Streptomycin (equivalent to 10ml Penicillin-Streptomycin-Glutamine (100X), liquid, Invitrogen, Catalog number: 10378-016) (all given numbers are the final concentration)

[H4IIE] (ALPHA-MEM)

500 ml: 5 g MEM/ALPHA (Thermo Scientific Hyclone, Catalog number: SH30007.03), added into 425 ml ultrapure water from Milli-Q water purification system (Millipore), 1.755 g D-glucose (Fisher Scientific, Catalog number: BP350-1), 1.1 g Sodium Bicarbonate for 5% CO2 (VWR, Catalog number: 12001-650), 50 ml Fetal Bovine Serum (Invitrogen, Catalog number: 16000-044), 10 ml Pen-Strep (Fisher Scientific, Catalog number: SV30010), adjust pH to 7.3 with HCl/NaOH, filter with Steritop filters (Millipore, Catalog number: SCGPT05RE)

[MCF-10A, BT474, MDA-MB-231, HeLa] (DMEM)

1 L: DMEM power 10 g (SAFC, Catalog number: 56436C) with 10% Fetal Bovine Serum (Invitrogen, Catalog number: 16000-044), 1% Penicillin/Streptomycin (equivalent to 10ml Penicillin-Streptomycin-Glutamine (100X), liquid, Invitrogen, Catalog number: 10378-016), 0.75 g Sodium Bicarbonate (Sigma-Aldrich, Catagory number: S5761), adjust pH to 7.3 with

HCl/NaOH, filter with Steritop filters (Millipore, Catalog number: SCGPT05RE) (all given numbers are the final concentration)

[37B, M4e, 686LN, Tu686] (DMEM/F-12)
1 L: DMEM/F-12 (CellGro, Catalog number: 10-090-CV) with 10% Fetal Bovine Serum (Invitrogen, Catalog number: 16000-044)

0.05% Trypsin-EDTA (1x), phenol red (Invitrogen, Catalog number: 25300-054)
PBS (Invitrogen, Catalog number: 10010-023)
70% Ethanol in water

C.2. Equipments

Clean 37 ℃ water bath
Personal protective equipment (sterile gloves, laboratory coat, safety goggle)
Biosafety Cabinet Class II
37 ℃ and 5% CO_2 Incubator
Aspirator, centrifuge, pipette

C.3. Procedure

1. Here HCT116-MKI67-1000 GFP cell line is used as an example, for other cells the general procedures are the same while the medium need to be changed accordingly.
2. Warm PRMI 1640 medium and trypsin-EDTA in the 37 ℃ water bath for about 15 min, and turn on the centrifuge machine ahead if cooling function is included. Label the centrifuge tube and new culture flask as below:

HCT116-MKI67-1000 GFP
09/09/2011
HAN

3. For a T25 culture flask, remove old medium with aspirator (cap the glass tip with disposable 10 µl pipet tips for each use)
4. Pipet 5 ml PBS (for T75 flask and petri dish, use 10 ml) gently into the T25 flask, gently shake for 30 s
5. Remove PBS with aspirator, and add in 1 ml trypsin-EDTA (for T75 and petri dish use 2 ml). Keep the culture flask in the incubator for about 5 min
6. Observe the cell detaching under the microscope, after this process finishes wash the cell suspension with 4 ml of medium (for T25 and petri dish 8 ml is needed to reach 10 ml of final volume) and transfer the solution into 15 ml centrifuge tube
7. Centrifuge at 800-1000 rpm for 4:30 min to 5min (higher rpm and longer centrifuge would increase cell aggregation). For centrifuges without cooling function, the centrifuge holders need to be kept in the 4℃ refrigerator. For centrifuges with cooling function, the centrifuge needs to be pre-cooled. This is to reduce cell adhesion to sidewall and enhance cell pellet separation from basal medium
8. Remove the supernatant with the aspirator. Add 5 ml RPMI1640 medium to the new T25 culture flask and resuspend the cell pellets to 2 ml in fresh medium. Split the cell suspension at 1:6–1:8 ratio to the new culture flask
9. Keep the cells in a 37℃ and 5% CO_2 incubator